


12-1-2017

# Surface and Interface Characterization of Solution-Processed Metal Oxides and PEDOT:PSS Using Photoelectron Spectroscopy

Lynette M. Kogler

*University of Nevada, Las Vegas*, [lmkogler@outlook.com](mailto:lmkogler@outlook.com)

Follow this and additional works at: <https://digitalscholarship.unlv.edu/thesesdissertations>

 Part of the [Engineering Science and Materials Commons](#), [Materials Science and Engineering Commons](#), and the [Physical Chemistry Commons](#)

---

## Repository Citation

Kogler, Lynette M., "Surface and Interface Characterization of Solution-Processed Metal Oxides and PEDOT:PSS Using Photoelectron Spectroscopy" (2017). *UNLV Theses, Dissertations, Professional Papers, and Capstones*. 3143.  
<https://digitalscholarship.unlv.edu/thesesdissertations/3143>

This Dissertation is brought to you for free and open access by Digital Scholarship@UNLV. It has been accepted for inclusion in UNLV Theses, Dissertations, Professional Papers, and Capstones by an authorized administrator of Digital Scholarship@UNLV. For more information, please contact [digitalscholarship@unlv.edu](mailto:digitalscholarship@unlv.edu).

SURFACE AND INTERFACE CHARACTERIZATION OF SOLUTION-PROCESSED  
METAL OXIDES AND PEDOT:PSS USING PHOTOELECTRON SPECTROSCOPY

By

Lynette M. Kogler

Bachelor of Science – Astronomy & Physics

Texas Christian University

1995

A dissertation submitted in partial fulfillment of  
the requirements for the

Doctor of Philosophy – Chemistry

Department of Chemistry and Biochemistry

College of Sciences

The Graduate College

University of Nevada, Las Vegas

December 2017

Copyright by Lynette M. Kogler, 2017

All Rights Reserved



## **Dissertation Approval**

The Graduate College  
The University of Nevada, Las Vegas

December 7, 2017

This dissertation prepared by

Lynette M. Kogler

entitled

Surface and Interface Characterization of Solution-Processed Metal Oxides and  
PEDOT:PSS Using Photoelectron Spectroscopy

is approved in partial fulfillment of the requirements for the degree of

Doctor of Philosophy - Chemistry  
Department of Chemistry and Biochemistry

Clemens Heske, Dr. rer. nat.  
*Examination Committee Chair*

Kathryn Hausbeck Korgan, Ph.D.  
*Graduate College Interim Dean*

Dong-Chan Lee, Ph.D.  
*Examination Committee Member*

Kathleen Robins, Ph.D.  
*Examination Committee Member*

Daniel Gerrity, Ph.D.  
*Graduate College Faculty Representative*

## ABSTRACT

### SURFACE AND INTERFACE CHARACTERIZATION OF SOLUTION-PROCESSED METAL OXIDES AND PEDOT:PSS USING PHOTOELECTRON SPECTROSCOPY

by

Lynette M. Kogler

Dr. Clemens Heske, Advisory Committee Chair

Professor of Chemistry

University of Nevada, Las Vegas

Solution-processed materials are appealing for use in printable electronics as a means to lower production costs, but precise control of the process is crucial for achieving the desired properties in the final materials and their interfaces. Electronic interface properties depend on both the involved materials and their fabrication processes, impacting the development and commercialization of these materials. Analyzing the chemical and electronic structure of these materials, particularly at the surfaces and interfaces, is important not only for insuring that the materials have the desired properties, but also for understanding the effects of the fabrication process and how to modify properties via processing for specific applications. To gain such insights into the chemical and electronic properties at the surface, photoelectron spectroscopy and inverse photoemission spectroscopy have proven to be powerful techniques.

In the first part of this research, indium-based transparent conductive oxides (TCOs) were prepared by spin-coating precursor solutions of metal-acetylacetonate coordination complexes onto glass substrates. The precursor films were converted into TCO films by annealing in

ambient air or in dry nitrogen. These were characterized with X-ray Photoelectron Spectroscopy (XPS), Ultraviolet Photoelectron Spectroscopy (UPS), and Inverse Photoemission Spectroscopy (IPES). The observed surface chemistries and electronic structures are reported, and the effects of ambient environment, low-energy (50 eV) ion treatments, and heating in ultra-high vacuum (UHV) will be discussed.

The second part of this dissertation explores the surfaces of, and the interface between, two materials widely used in printable organic electronics: indium tin oxide (ITO) and poly(3,4-ethylenedioxythiophene) polystyrene sulfonate (PEDOT:PSS). Spin coating was used to fabricate thin films of both ITO and PEDOT:PSS, which were then characterized using XPS, UPS, and IPES. Inhomogeneities in the PEDOT:PSS films involving differing ratios of PEDOT to PSS were observed using XPS, and the work function at different points on individual samples was measured. The impact of these findings on the surface electronic properties and the implications for printable electronic devices will be discussed.

## ACKNOWLEDGEMENTS

There are many people who have aided me on this amazing journey, and I could easily turn these acknowledgements into another dissertation in recognizing all of them. Hence, I must limit myself to those who I need to thank specifically:

Dr. Clemens Heske, for giving me the opportunity to work with some incredible instrumentation, to learn spectroscopic methods I had never heard of before, and to use these to characterize some fascinating materials. I am grateful to Dr. Heske for his support on my scientific adventure, for his encouragement to dive deep into increasing my knowledge and understanding, and for challenging me to think outside the “black box.”

Dr. Marc Häming, first for introducing me to solution-processed metal oxides, and then for helpful advice and information, almost entirely via e-mail and regular Skype meetings – with a nine-hour time zone difference – for over three years. I am extremely grateful to Dr. Häming for introducing me to coding for fityk; it has saved me a lot of time!

Members of the extended Heske research group, past and present: Drs. Monika Blum, Lothar Weinhardt, Timo Hofmann, Samantha Rosenberg, Kim Horsley, Douglas Duncan, Michelle Mezher, Dirk Hauschild, Erki Kärber, and Manuela Wallesch, and members James Carter, Kyle Aleshire, Chase Aldridge, Ryan Bugni, Sarah Alexander, Evan Misak, James Maslow, Mary Blankenship, and Amandee Hua. Thank you for training on and insight into instrumental methods and data analysis, advice, feedback, a patient ear during rants of frustration, and miscellaneous adventures outside the laboratory. I am grateful for all of those things, and I hope I have been able to give back in return. Not to be forgotten, thanks also go to

honorary group member, SEB Technical Director Eric Knight, for helping us improve our capabilities and keeping things running.

My committee members, Drs. Clemens Heske, Dong-Chan Lee, Kathy Robins, and Daniel Gerrity, for their patience, feedback, and goodwill throughout the process: the examinations, the meetings, the presentations, the paperwork, and all the emails.

The Department of Chemistry & Biochemistry Faculty and Staff, with special thanks to past and present administrative staff, Mark Miyamoto, Debbie Masters, Bianca Rideout, and Marsha McDuff.

The College of Sciences, the Graduate College, and in particular, the Graduate Student & Professional Association for providing conference travel funding in Spring 2017. In particular, thanks to Graduate Affairs Coordinator Keala “Ala” Kiko and former GPSA Manager Rebecca Bolton, for keeping me headed in the right direction with policies and paperwork.

Family, but especially my mother, Charlene Kogler, who made my time in grad school a lot easier than it could have been in many different ways, although my favorite was always a fun dinner at Steiner’s. Mom, I will always be glad and proud to serve as your tech support!

Friends in Vegas and elsewhere: my local hiking group, whom I have greatly missed this last year of busyness with conferences, dissertation, etc., and my distant, “e-mail” friends (many of whom who have surely wondered if I was even still alive due to lack of contact). I am particularly grateful for the friendship and support of Dr. Daria Boeninger and Bridgette Quinn, whose previous experiences in grad school provided much validation and understanding.

Thank you, all.



## DEDICATION

There are many people to whom I could dedicate this work, all deserving in one way or another. However, there is one person who deserves very special mention of the role she played in my life's pursuit of science. So I dedicate this work to Mrs. Trammell Henson.

As my mathematics teacher at (then) C.V.T Gilbert Sixth Grade Center, she made a subject that I had struggled with until then both comprehensible and fun. I am still not entirely sure how she did it, but she somehow made math, the language of science, intelligible to me. Although I already had a deep love of science, Mrs. Henson gave me the gift of being able to understand and speak its language. Because of her, I was able to use the tools of algebra, geometry, trigonometry, and my favorite, calculus, to fully pursue the science that I loved.

One person can truly make a difference in others' lives, and Mrs. Henson did so for me. It is with deep respect and immense gratitude that I dedicate this to her.

## PREFACE

Because this research lies at the intersection of chemistry, physics, material science, and engineering, its prospective audience could be quite varied. I have endeavored to make many different concepts accessible for a diverse scientific audience. Substantial material has also been included in the Appendices, in the hope that a written record of the tools I have used may assist other researchers in their own work.

# TABLE OF CONTENTS

Abstract .....	iii
Acknowledgements.....	v
Dedication.....	vii
Preface.....	viii
Table of Contents.....	ix
List of Tables .....	xii
List of Figures.....	xiii
Chapter 1 – INTRODUCTION.....	1
Section 1.1 – Motivation: More Efficient Use of More “Clean” Energy .....	1
Section 1.2 – Organic Electronics.....	2
Section 1.3 – Printable Electronics and Solution-Processed Materials .....	4
Section 1.4 – Transparent Conductive Oxides.....	5
Section 1.5 – Research.....	6
Section 1.6 – Dissertation Overview .....	8
Chapter 2 – EXPERIMENTAL TECHNIQUES .....	10
Section 2.1 – A few basic principles of spectroscopy .....	10
Section 2.2 – Ultra-High Vacuum .....	12
Section 2.3 – Photoelectron Spectroscopy.....	13
Section 2.4 – Inverse Photoemission Spectroscopy (IPES).....	23
Section 2.5 – Extrapolation of VBM, CBM, and Band Gap .....	25
Chapter 3 – SOLUTION-PROCESSED METAL OXIDES .....	27
Section 3.1 – Background.....	27

Section 3.2 – Precursor Solution.....	30
Section 3.3 – The Thin Film Coating Process .....	31
Section 3.4 – Samples.....	32
Section 3.6 – Indium Oxide Samples Made in Air and N <sub>2</sub> .....	34
Section 3.7 – Indium Zinc Oxide (IZO) .....	42
Section 3.8 – Indium Tin Oxide (ITO) .....	45
Section 3.9 – Conclusions.....	49
Chapter 4 – PEDOT:PSS THIN FILMS.....	52
Section 4.1 – Introduction.....	52
Section 4.2 – Experimental: Solution Development.....	54
Section 4.3 – Thin Film Process .....	56
Section 4.4 – Multiple Layers.....	57
Section 4.6 – Results: PEDOT:PSS Inhomogeneities and Beam Damage.....	58
Section 4.7 – Results: PEDOT:PSS on ITO .....	69
Section 4.7 – Conclusions.....	74
Chapter 5 – SUMMARY AND FUTURE WORK.....	76
Appendix A – LIST OF ABBREVIATIONS AND SYMBOLS .....	80
Appendix B – SPECTROSCOPY EQUIPMENT.....	82
Appendix C – CHEMICAL INFORMATION .....	83
Appendix D – INPUT CODE FOR PEAK FITTING .....	84
Appendix E – SPIN COATERS .....	87
Section E.1 – Single-Speed Spin Coater.....	87
Section E.2 – Variable-Speed Spin Coater .....	87

BIBLIOGRAPHY.....	92
CURRICULUM VITAE.....	99

## LIST OF TABLES

Table 2-1. Excitation sources, their energies, and their uses. <sup>[29]</sup> .....	14
Table 3-1. Indium 3d <sub>5/2</sub> and M <sub>4</sub> N <sub>4,5</sub> N <sub>4,5</sub> peak positions and $\alpha'$ for samples In-ox (air), before and after ion treatment (IT), and In-ox(N <sub>2</sub> ). .....	39
Table 4-1. Resistance in multilayer PEDOT:PSS samples. ....	57
Table 4-2. In 3d <sub>5/2</sub> and In M <sub>4</sub> N <sub>4,5</sub> N <sub>4,5</sub> peak positions, and modified Auger parameter for indium, as detected in PP thin films. ....	72
Table E-1. Measurements of rpm for each position of 8-position selector switch after final assembly of spin coater.....	89

## LIST OF FIGURES

<p>Figure 2-1. Attenuation depth as a function of electron energy, determined experimentally. Attenuation depth <math>\lambda</math> is related to atom size, hence <math>\lambda</math> is expressed in terms of monolayers of atoms of a particular element. The approximate monolayer depth of analysis for XPS, UPS, and IPES is indicated. Graph adapted from [26].....</p>	12
<p>Figure 2-2. Diagram of concurrent XPS and AES processes..</p>	16
<p>Figure 2-3. XPS survey spectrum of indium oxide.....</p>	17
<p>Figure 2-4. Wagner plot of several different indium species. Reproduced from a Wagner plot for indium from the NIST XPS Database [30].....</p>	20
<p>Figure 2-5. Diagram of UPS process and the concept of work function (WF, or <math>\Phi</math>). .....</p>	21
<p>Figure 2-6. Diagram of the IPES process. ....</p>	23
<p>Figure 2-7. Diagram of the combination of UPS and IPES data, the extrapolation of the valence band maximum and the conduction band minimum, and the derivation of the electronic surface band gap. ....</p>	25
<p>Figure 3-1. Diagram of electronic structure and band gaps for different materials: (a) metal, (b) n-type semiconductor, (c) p-type semiconductor, (d) insulator. The energy difference between the Conduction Band Minimum and the Valence Band Maximum is the band gap (<math>E_g</math>). .....</p>	27
<p>Figure 3-2. Vanadyl acetylacetonate molecular structure, showing vanadium-oxygen acac bonds and a double bond to a single oxygen atom to balance V<sup>4+</sup> oxidation state. (Ben Mills, Wikimedia Commons, Vanadyl-acetylacetonate-from-xtal-3D-balls.png, based on [34].) .....</p>	30

Figure 3-3. Three XPS surveys of two solution-processed indium oxides samples: a sample made in air before and after 50 eV Ar <sup>+</sup> ion treatment, and a sample made in N <sub>2</sub> . Taken with a monochromated Al Kα x-ray source.....	34
Figure 3-4. C 1s spectra after peak fitting. Positions of fitted peaks are given with most likely corresponding species (from [30]). The residual, i.e., the difference between data and fit, is shown below each spectrum on a magnified scale. ....	36
Figure 3-5. C 1s and O 1s spectra of an In-ox sample made in air and then ion treated, and an In-ox sample made in N <sub>2</sub> .....	36
Figure 3-6. Peak fitting of O 1s spectrum of In-ox (N <sub>2</sub> ). The approximate ranges of different oxygen species are indicated by arrows, based on data from the NIST XPS Database [30].....	37
Figure 3-7. O 1s spectra after peak fitting, for the In-ox sample made in air, before and after ion treatment.....	38
Figure 3-8. Wagner plot of In-ox samples made in N <sub>2</sub> and in air, before and after ion treatment. Indium oxide is the major contributor to the In 3d <sub>5/2</sub> and In M <sub>4</sub> N <sub>4,5</sub> N <sub>4,5</sub> Auger peak positions. ....	40
Figure 3-9. Band gap extrapolations of In-ox (air), before and after IT, and In-ox (N <sub>2</sub> ).....	41
Figure 3-10. XPS Survey spectra of IZO annealed at 250 and 450 °C. A larger carbon signal is observed in the survey of the 250 °C sample. ....	43
Figure 3-11. (a) XPS O 1s spectra of In-ox, Zn-ox, and IZO, before heating in UHV. (b) Change in the O 1s lineshape of IZO after UHV heating.....	44
Figure 3-12. XPS survey spectra of solution-processed ITO and commercially produced ITO.....	45



Figure 3-13. Work function (WF) determination of CITO and ITO, before and after ion treatment. Data is shown after subtraction of the applied bias voltage. ....	46
Figure 3-14. Extrapolated VBM and CBM from UPES and IPES data for SITO and CITO samples. ....	48
Figure 4-1. Molecular structures of PEDOT (top) and PSS (bottom). From [36]. ....	52
Figure 4-2. Change in PEDOT chain conformation due to surfactant ion replacement of PSS, as proposed by Fan et al. Modified from [60]. ....	55
Figure 4-3. XPS survey spectrum of a PEDOT:PSS thin film on glass. ....	58
Figure 4-4. Example of the S 2p region in XPS, indicating how different chemical species can be differentiated. Reference XPS data on PEDOT:PSS from [49] were used for initial verification of species. Reference values (in black) are taken from [30]. ....	59
Figure 4-5. Photograph of the PP-SITO sample. The approximate locations of three measurement spots are marked. The sample was cut along the edge closest to Spot 3. ....	60
Figure 4-6. XPS measurements of the S 2p region for PP-SITO and PP-CITO, showing the differing intensities of PEDOT (ca. 164 eV) and PSS (ca. 168 eV) with respect to measurement location on the samples. ....	61
Figure 4-7. Multiple XPS measurements of the S 2p region on PP-SITO. With each measurement, the PSS peak intensity decreases and the PEDOT peak intensity increases at each measurement spot. ....	62

Figure 4-8. Peak fitting of XPS S 2p spectra for PEDOT:PSS. (a) Fitting a S 2p doublet for each polymer gives a poor fit. (b) A better fit is possible when the ionic species are also considered [46,47,85], requiring a total of four S 2p doublets in the fit. ....	63
Figure 4-9. Ratios of peak area sums for PEDOT and PSS at different sample spots for PEDOT:PSS on SITO and CITO substrates.....	64
Figure 4-10. Secondary electron cutoff (SEC) measurements of PP-CITO-2 at different sample spots (after correction for the bias voltage).....	66
Figure 4-11. UV beam damage of PP film changes the intensity of PSS and PEDOT peaks in “before and after” XPS measurements .....	68
Figure 4-12. Survey spectra of PEDOT:PSS samples on SITO and CITO samples, with a SITO survey for reference purposes.....	69
Figure 4-13. XPS measurement of In 3d peaks, detected at the surface of PEDOT:PSS on CITO.....	70
Figure 4-14. C 1s and O 1s spectra of the PP2-CITO and PP3-SITO8g samples shown in the survey spectra of Figure 4-12. ....	71
Figure 4-15. Wagner plot for indium from Fig. 2-4, with data added for PP-SITO and PP-CITO samples.....	73
Figure E-1. Single-speed spin coater. Copper wire substrate holders visible on top.....	87
Figure E-2. Variable speed spin coater. Copper mesh holders for 15x15mm <sup>2</sup> and 25x25mm <sup>2</sup> substrates visible on top. Profile sections and electronics are visible through the PVC enclosure. On/off switch is on the left, and rotary 8-position rpm selector switch is on the right.....	90

Figure E-3. Photograph of circuit board at the back of the spin coater and diagram of the resistors connected to the switch positions..... 91

## Chapter 1 – INTRODUCTION

### Section 1.1 – Motivation: More Efficient Use of More “Clean” Energy

Advancements in electronics have changed the world – and the world of electronics has made enormous advancements – in the past few decades. New materials, new processes, and new structures have made incredible technologies possible that, just a few decades ago, lay in the realm of science fiction. One needs to look no farther than today’s smart phones and tablet PCs to see the realization of late 20<sup>th</sup>-century futurisms. Even now, ongoing research at the intersection of chemistry, physics, and materials science is leading to new technologies and products – and more efficient, low-cost approaches – that are changing the world globally.

Recent years have seen a large increase in the development of “clean” and renewable energy sources, specifically wind and solar, across the world.<sup>[1,2]</sup> Political factors, such as government commitments and investment, have played a part in the increase, but lowering the cost of the manufacturing components and making technology more efficient has helped make solar and wind power more economically favorable as well.<sup>[3]</sup> For developing countries, low-cost renewable energy sources can be put in places that previously had little to no access to electricity, skip over the dependency on fossil fuels as they develop large-scale energy grids, reduce the negative health impacts of air pollution, and create new jobs.<sup>[4]</sup> In 2016, the reduced cost of renewable energy enabled developing countries to invest more in renewables than developed countries, and China has been and continues to be a global leader in renewable energy investment and manufacturing.<sup>[5,6]</sup> One of the most important benefits of using more clean energy sources is reducing emissions of greenhouse gases that are causing climate change. With faster-than-expected development of renewable energy globally,<sup>[1]</sup> the outlook for slowing down climate change is optimistic.

In tandem with generating energy from clean, renewable sources, reducing the amount of energy consumed is an important focus. Two effective ways to do this in power-hungry nations like the United States are to introduce energy-saving products to replace those already in use and to design new products with inherently lower power consumption. Technological development has been key to not only the invention of energy-efficient devices like light-emitting diodes (LEDs), but also making those products cost-effective to produce, distribute, and be used by consumers.

## Section 1.2 – Organic Electronics

Organic materials hold promise in replacing costly, non-renewable materials in electronic devices. Organic photovoltaics (OPVs, or organic solar cells) and organic light-emitting diodes (OLEDs) are two examples of developing technologies that can help address the goals of clean energy production and efficient energy consumption, respectively. Designing organic molecules with light absorbing or emitting properties has been done for years for different-colored dyes and fluorescent materials. Through decades of research, conductive polymers and self-assembling small molecules have been and continue to be designed to make materials that absorb light (for OPVs), emit light (for OLEDs), or enhance charge carrier transport in devices as interfacial layers between different materials.

Once made exclusively of inorganic semiconductors, LEDs are now also being made from organic materials (OLEDs) and have been incorporated into displays with great success. Production costs have lowered sufficiently, such that OLED displays are being used in affordable products like smart phones and watches, tablets, and televisions. OLED lighting has begun to

emerge onto the consumer market, with the advantage over conventional LEDs in creating flexible panels of diffuse light closer to sunlight in color rendering, without emitting UV light.<sup>[7]</sup> Diffuse light being characteristic of OLED panels, additional lighting components that diffuse light (necessary for conventional LEDs) or serve as heat sinks are not needed. Currently, OLED lighting panels are much more expensive than available lighting products. In the past, the same was true of LEDs compared to traditional incandescent bulbs and compact fluorescent lights,<sup>[8]</sup> but production costs did come down and now LED lighting is the first choice for energy-efficient lighting. With further refinement of manufacturing processes, cost can be lowered for OLEDs. In the future, we should see more affordable OLED lighting on the consumer market. While their form and light emission is not useful for light bulbs, OLEDs can serve a complementary role to LEDs in the energy-efficient lighting market.

The advantages of OPVs include roll-to-roll printing on flexible substrates and being composed of readily abundant, renewable elements. Compared to photovoltaics made from inorganic materials, however, OPVs have faced several challenges at becoming commercially viable. The most important of these challenges are increasing the efficiency of conversion of light to usable electricity (power conversion efficiency), organic material degradation due to water, oxygen, and/or light (usually via air exposure), and device lifetime. Efficiencies have improved, with a power conversion efficiency greater than 13% recently reported.<sup>[9]</sup> Careful selection of device materials and designing the order of device layers and additional components has improved device stability and lifetimes.<sup>[10]</sup> OPVs do have a limited presence on the commercial market<sup>[11]</sup> compared to inorganic PVs. With additional improvements to OPV devices and finding the markets where OPVs are a better choice than today's low-cost inorganic PVs, we could see more use of OPVs in the future.

## Section 1.3 – Printable Electronics and Solution-Processed Materials

One area of research that contributes to lowering electronic device manufacturing costs is in developing materials that can be rapidly printed using existing printing technology. Printable electronic materials are also of interest in improving existing technology and develop new applications, such as thin, flexible batteries.<sup>[12]</sup>

Processes such as lithography and screen printing have been and remain mainstay production processes in the creation of electronic circuitry.<sup>[13]</sup> However, new materials are making manufacturing processes like inkjet printing a reality for commercially produced goods.<sup>[12]</sup> While other processes can be expensive and pose safety and waste concerns, using materials that can be deposited onto a surface like ink onto paper can reduce material waste and cost, and produce the thin, light-weight devices that are increasingly demanded by consumer electronic applications.<sup>[12,13]</sup> Another benefit of this more efficient use of materials is the easy customization of products by digital printing methods, leading to reduced production costs.<sup>[2]</sup>

Creating an electrically conductive material from a printable “ink” has three requirements. First, the desired material must be capable of being suspended in or derived from a liquid solution with properties suitable for the printing method used. Second, it must be possible to fabricate the solid state material from the solution. Third, the solid material must have the desired properties for the application for which it is intended. Variables like solubility, viscosity, and solvent and additive residues influence how well each of these requirements are met.

The types of solution-processed electronic materials are vast, and both organic and inorganic materials can be made from a solution. Nanoparticles and other nanostructures,

typically of inorganic metal compounds in a solvent dispersion, show promise for printable electronics.<sup>[12,13]</sup> Formation of materials with specific crystal structure from chemical solution can be employed for creating perovskite and kesterite solar cells.<sup>[14]</sup> Organic solvents and molecules may be employed as carriers of metallic elements and compounds for the formation of inorganic structures.<sup>[15]</sup> Many of the organic materials used to make OPVs and OLEDs have already been developed to be dissolved or suspended in liquids.

The advantages of printing electronic components are offset by the need for precise control of the process to convert the material from solution to solid state. Control of the fabrication process parameters is crucial for achieving the desired properties in the final material; this is true for many manufacturing processes. In particular, electronic interface properties for solution-processed materials depend on both the material and the fabrication process, which in turn greatly impacts the development, optimization, and manufacture of electronic devices.

## Section 1.4 – Transparent Conductive Oxides

Transparent conductive oxides (TCOs) are an essential part of modern electronics; they are found in OLEDs, OPVs, sensors, displays, and many other devices.<sup>[16]</sup> Indium tin oxide (ITO), also called tin-doped indium oxide, is the most-used TCO in the electronics market,<sup>[16]</sup> and most of the world's indium production goes toward TCO thin films in displays and touch screens.<sup>[17]</sup> ITO coatings are produced by magnetron sputtering, evaporative methods, and other physical vapor deposition (PVD) techniques that typically require vacuum or controlled atmosphere processing.<sup>[16]</sup> Solution-processing of ITO from an organic precursor solution was investigated over two decades ago, but the effectiveness of PVD techniques at producing the



desired thin film properties seems to have eclipsed solution processing as a favorable method at that time.<sup>[18,19]</sup> A thin coating of ITO typically serves as a transparent electrode, allowing light to pass into (PV) or out of (OLED) a device.

A roll-to-roll printing of reasonably efficient organic solar cells could help lower costs for OPVs and allow for greater use of solar energy. Ironically, one of the barriers to this is a simple, preferably solution-based process to make ITO.<sup>[20]</sup> Roll-to-roll printing of OPVs is currently done on polymers coated with a thin film of ITO produced by sputter deposition. Sputter deposition is done in a vacuum by bombarding an ITO ingot target with ions of an inert gas, usually argon.<sup>[21]</sup> Commercial sputtering equipment costs from tens to hundreds of thousands of dollars, not including costs of operation, maintenance, and consumables such as gas and sputter targets. Mass production of sputtered ITO on glass and polymer has made these ITO-coated materials reasonably inexpensive, but a further reduction in the cost of production could make a significant difference in making OLEDs, OPVs, and other ITO-containing devices more cost-effective when produced on a commercial scale.

## Section 1.5 – Research

The purpose of the first part of this dissertation was to take a new look at making indium-based TCOs, including ITO, from a precursor solution. Unlike expensive, vacuum-dependent sputter processes, these films were made at room temperature under either ambient air or dry nitrogen. The samples were made from metal ion-acetylacetonate (acac) coordination complexes. These compounds are readily available for purchase, and metal oxide thin films for transistors have already been successfully made from metal-acac complexes dissolved in solvent.<sup>[22]</sup> In this

study, the surface chemistry and electronic structure of TCO thin films was investigated using photoelectron spectroscopy, and the resulting characteristics of solution-processed ITO thin films were compared to those of commercially-produced ITO to assess the suitability of the solution-processed ITO as an electrode for use in organic electronic devices.

In the second part of this dissertation, the conductive polymer PEDOT:PSS was applied to samples of commercial ITO and solution processed ITO and characterized with the same photoelectron spectroscopy methods as before. PEDOT:PSS has been used in organic electronics as a hole transport layer between ITO and the active organic material. Therefore studying the characteristics at the interface between PEDOT:PSS and the two different ITO samples should shed additional light on the suitability of solution-processed ITO for use in organic electronics.

Chemical and electronic structure differences between the commercial and solution-processed ITO thin films were initially expected. One of the advantages of the vacuum-based sputter deposition process is that a high purity of the final ITO film can be expected. In contrast, residues from the decomposition of the organic solvent and ligand are to be expected in the solution process ITO, but the composition of those residues, if present in detectable amounts, and how they affect the thin film properties can not easily be predicted. Indeed, the solution-process does result in some differences in the surface chemistry and electronic properties, but these differences are not as large as might have been expected, and this initial study indicates that a solution-processed ITO could be viable as a substitute to sputter-deposited ITO in organic electronics.

## Section 1.6 – Dissertation Overview

The objective of this work was to investigate the surface chemistry and electronic properties of solution-processed materials and gain further insight into how fabrication process affects those properties at the material surface. The methods employed involved primarily x-ray and ultraviolet photoelectron spectroscopies, as well as inverse photoemission spectroscopy. These powerful techniques have already proven highly useful in characterizing the chemical composition and electronic structure of PV materials.<sup>[23]</sup> The next chapter describes these spectroscopies and illuminates important concepts in their use.

Chapter 3 describes the first phase of this research, the exploration of indium-based TCO thin films using a solution process. Using metal-acetylacetonate coordination complexes dissolved in solution, thin films of indium oxide (In-ox), indium zinc oxide (IZO), and indium tin oxide (ITO) were made via spin coating and annealing. These films were characterized using X-ray Photoelectron Spectroscopy (XPS), Ultraviolet Photoelectron Spectroscopy (UPS), and Inverse Photoemission Spectroscopy (IPES). To compare select process conditions, films were made under ambient air and in a glove box containing dry nitrogen, as well as at different annealing temperatures. Changes in film properties after heating in ultra-high vacuum (UHV) and after soft (50 eV) ion treatments were also studied, as these represent two possible post-fabrication modifications to the films and their surfaces that may be used to change surface properties.

Chapter 4 discusses the thin film application of PEDOT:PSS and measurements with XPS, UPS, and IPES. As an aqueous dispersion of two polymers, PEDOT:PSS brings its own unique challenges in thin films formation, and the conductive PEDOT, combined with the non-conductive PSS, also presents an interesting set of properties for photoelectron spectroscopy

measurements. The surface properties of PEDOT:PSS on commercial and solution-processed ITO are compared.

The overall findings are summarized in Chapter 5, and the implications for printable electronic devices are discussed. Ideas for future work are also presented.

## Chapter 2 – EXPERIMENTAL TECHNIQUES

### Section 2.1 – A few basic principles of spectroscopy

#### Section 2.1.1 – Fermi’s Golden Rule

Spectroscopy is the science of analyzing materials via the interaction of electromagnetic radiation (EM) with matter. The heart of spectroscopy is best described by Fermi’s Golden Rule, written here in a general form<sup>[24]</sup> for discussion purposes:

$$I \propto |\langle \psi_f | \hat{O} | \psi_i \rangle|^2 \delta(h\nu - |E_f - E_i|) \quad (1)$$

In this form, maximum or peak intensity ( $I$ ) is proportional to a matrix element of a specific transition that contains a transition operator ( $\hat{O}$ ), an initial state ( $|\psi_i \rangle$ ), and a final state ( $\langle \psi_f |$ ).

The Kronecker delta in the equation ensures conservation of energy:  $\delta(0) = 1$  and  $\delta(\neq 0) = 0$ .

For XPS and UPS, the conservation of energy takes the form of

$$0 = h\nu - |E_k + E_b + \Phi| \quad (2)$$

where  $\Phi$  represents the work function of the sample (in a model in which the kinetic energy of the emitted electron is referenced to the vacuum level). When referenced to the Fermi energy, (2)

can be rewritten as

$$h\nu = E_k + E_b, \quad (3)$$

which describes the conservation of the excitation energy from x-ray or UV photons as the sum of the electron’s kinetic energy ( $E_k$ ) and the energy of the state to which it was bound ( $E_b$ ).

Because of the quantization of energy at the atomic/molecular scale, specific and characteristic values for  $E_b$  for the different energy states in atoms and molecules are observed. It should be noted that there is an inherent assumption in Equations 2 and 3 that the electron undergoes no inelastic scattering as it travels from the emitting atom to the sample surface and on to the electron analyzer.

The above involves the absorption of photons by the material. However, when any EM radiation encounters matter, one of the following basic processes may occur: transmission through the material, absorption by the material, or reflection/scattering. The numerous types of energy transfer that can occur between EM radiation and matter can be very complex, and they give rise to specialized types of spectroscopies. For purposes of this discussion, EM radiation will be limited to the range of x-rays and UV light. At this point, we will briefly discuss the path these electrons must travel before we return to discussion of the spectral signals they produce.

#### Section 2.1.1 – Inelastic Mean Free Path

The mean free path (MFP) is defined as “the average distance travelled by a particle, atom, etc., between collisions” with other particles.<sup>[25]</sup> Intuitively, the length of the mean free path increases as distance between adjacent particles increases. The MFP is applicable to many different systems, and its specific derivation varies accordingly. Generically, the mean free path ( $l$ ) is the inverse of the number of particles ( $n$ ) multiplied by the effective cross sectional area of collision ( $\sigma$ ) and can be written as:

$$l = (\sigma n)^{-1}. \quad (4)$$

In practical terms, the mean free path greatly affects the instrument design and operation, sample preparation, and the depth of the material that is analyzed. For PES techniques, the “collisions” or scattering interactions that occur between free electrons and the atoms and molecules in the material are illustrated in the *inelastic* mean free path (IMFP) of the emitted electrons. As an electron interacts with other particles in its path, it can eventually lose enough energy where it cannot escape the material surface and is recaptured into an unoccupied state in the material. Essentially, this results in a limited sample depth that can be analyzed using XPS

and UPS that is dependent on the kinetic energy ( $E_k$ ) of the electron<sup>[26]</sup>, which in turn is dependent on the excitation energy of the photon source (or, in case of IPES, the energy imparted to electrons by the electron gun). Figure 2-1 shows the impact of this on the different techniques of XPS, UPS, and IPES.

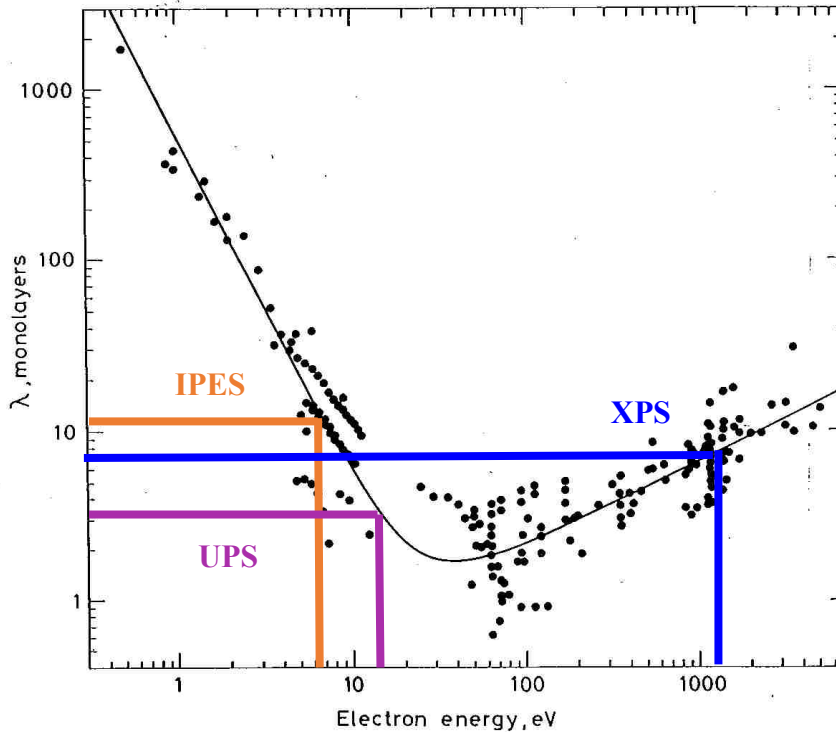


Figure 2-1. Attenuation depth as a function of electron energy, determined experimentally. Attenuation depth  $\lambda$  is related to atom size, hence  $\lambda$  is expressed in terms of monolayers of atoms of a particular element. The approximate monolayer depth of analysis for XPS, UPS, and IPES is indicated. Graph adapted from [26].

## Section 2.2 – Ultra-High Vacuum

Because free electrons are in either the final (PES) or initial (IPES) states for these methods, the IMFP for electrons is critical for the ability to collect data. An electron may have to

travel more than a meter through the vacuum chamber, the analyzer, and on to a detector; to achieve an IMFP of this length or more at room temperature requires pressures lower than  $10^{-4}$  mbar at minimum.<sup>[27,28]</sup> Realistically, pressures must be significantly lower than this – and the IMFP in vacuum much longer – for sufficient numbers of electrons to reach a multiplying detector to generate an adequate signal. Pressures in the ultra-high vacuum (UHV) range of  $10^{-10}$  mbar are necessary for good PES data.<sup>[28]</sup> The data to be discussed in later chapters was collected in this range.

### Section 2.3 – Photoelectron Spectroscopy

Photoelectron spectroscopy (PES) is based on the photoelectric effect: a photon of sufficiently high energy is absorbed by a material, resulting in the release of an electron from a bound state. Whereas the electrons only need move to the conduction band to generate a current to verify the photoelectric effect, extra energy must be supplied to impart enough kinetic energy to the released electrons for them to reach an electron analyzer. Typically, this is done using a light source of sufficiently high fixed photon energy to both release the bound electrons and eject them from the material. The electron analyzer then sorts those electrons by their kinetic energy to create a spectrum.

With the known value of the excitation energy of the photon and the measured EK values, equation (3) becomes

$$E_b = h\nu - E_k, \quad (5)$$

and binding energies can be calculated. Due to the quantization of energy states, these peaks occur at specific energies for specific elements. Moreover, due to bonds, defects, and other aspects of the material chemical environment, slightly more or less energy may actually be



needed to eject electrons from a given state; this will result in peak shifts that reflect the actual electronic states as affected by chemical composition and bonds, as well as final state effects (such as screening and shake-up/shake-off processes).

Two of the most common PES methods use either x-rays or ultraviolet rays of a fixed energy as the photon source. From Equation 3, it is clear that a specific, known excitation energy is needed for PES measurements. Outside of tunable synchrotron light sources, sources that provide a fixed excitation energy are routinely employed. Commonly used excitation energies and their applications are listed in Table 1.

Source Element	Excitation	Energy (eV)	Use
Helium	$I_{\alpha}$	21.22	UPS
	$I_{\beta}$	23.09	UPS
	$II_{\alpha}$	40.82	UPS
	$II_{\beta}$	48.38	UPS
Magnesium	$K_{\alpha}$	1253.6	XPS
Aluminum	$K_{\alpha}$	1486.6	XPS

Table 2-1. Excitation sources, their energies, and their uses.<sup>[29]</sup>

The type of information that can be derived from PES data is directly related to the energy of the excitation source; only electron states of energies lower than the excitation source may be probed. Ultraviolet sources are typically limited to the valence band and outermost orbitals of most elements. The higher energy of x-ray sources can excite electrons in core level states, but again, only to the limit of the excitation energy of the source. This is why the high energies and tunability of synchrotron x-ray sources are particularly desirable and even necessary

for some PES applications. Because of the photon-electron interactions and energy values involved, it is most convenient to discuss PES data in units of electron volts (eV). A table relating photon energies in electron volts to wavelength and other common spectroscopy units can be found in Appendix B.

Where multiple excitations are possible for an element, instrument design and operation may be used to reduce or eliminate unwanted excitations that would increase the broadening of spectral lines. A monochromator is highly effective but can also be very expensive and challenging to correctly align, particularly for x-rays. In the case of using a helium plasma as a light source, the pressure of the gas fed into the plasma chamber may be adjusted to encourage the second excitation (40.82 eV) and reduce the first (21.22 eV). Due to the very low intensities of the  $I_{\beta}$  and  $II_{\beta}$  emissions, using these as excitation sources requires a monochromator; however, the separation between spectra lines is wide enough that a single grating can be used. Ultimately, a thorough knowledge of the instrumentation used and how the data was collected is essential for correctly processing and interpreting PES data.

An important consideration for PES measurements is the conductivity of the sample. Because PES removes electrons from the sample, a non-conductive sample will become positively charged at the surface, and this in turn will affect the kinetic energies and peak positions of PES spectra. Samples that are conductive must be grounded, so as to have a source of electrons to draw upon to replace the electrons lost in the PES process. Conductive samples that are poorly grounded will also charge.

Another consideration is beam damage. The photon excitation and/or the loss of electrons can break bonds, damage materials, and change the chemical composition of the surface. Beam

damage must be kept in mind when making measurements and processing and interpreting PES data.

### Section 2.3.1 – X-Ray Photoelectron Spectroscopy (XPS)

The energy of x-rays allows probing of the energy levels of atoms in a material up to the limits of the excitation energy. This includes core levels and the valence band. The basic process is illustrated in Figure 2-2 in blue: an x-ray photon is absorbed, part of the energy goes into freeing the electron from its bound state, and the remaining energy becomes the kinetic energy imparted to the free electron. As mentioned earlier, the core levels are characteristic of different elements. Electrons in outer core levels involved in or affected by bonds or ionization states experience slightly different binding energies in those states than if they were in single atoms or neutral species. As a result, the XPS spectra will show shifts in peak energy.

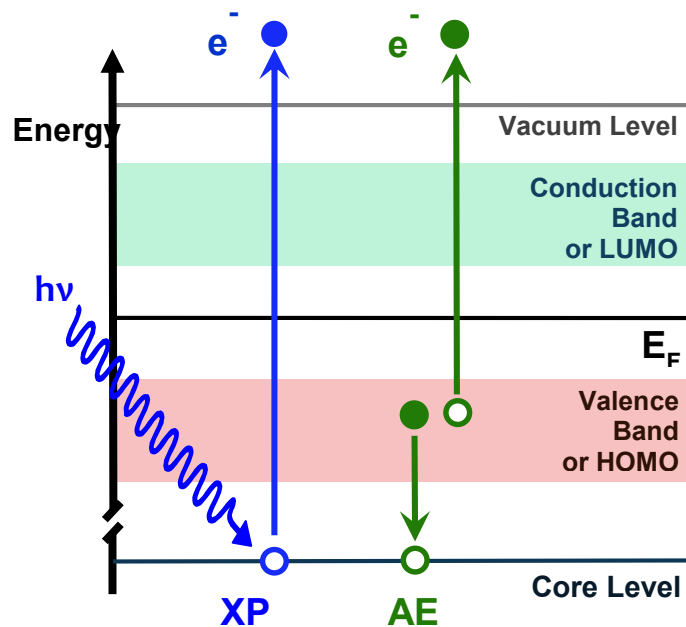


Figure 2-2. Diagram of concurrent XPS and AES processes..

The Auger process shown in Fig. 2-2 occurs in XPS measurements due to the core level electron vacancies (holes) left by x-ray excitation. In the Auger process, an electron in a higher energy level relaxes to the core hole. In doing so, it releases the amount of energy characteristic of that transition. In a simplified picture, that energy is transferred to an adjacent electron, giving it the kinetic energy to be removed its bound state and be detected by the analyzer. Again, because the quantized energy levels and transitions are characteristic of elements and their compounds, Auger peaks that occur in an XPS spectrum are characteristic of a particular element and its chemical environment. Note that in the Auger process, there is no dependence on the energy of the excitation source, and values of Auger peak positions are correctly expressed in terms of kinetic energy.

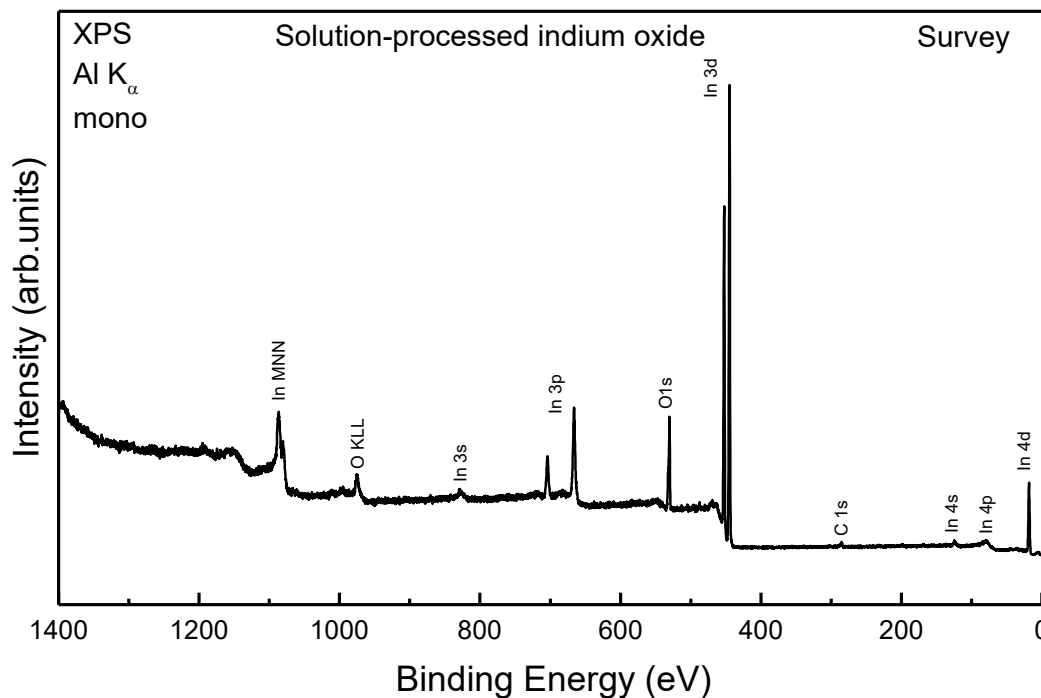


Figure 2-3. XPS survey spectrum of indium oxide.

For XPS, spectral peaks and detailed regions are usually labelled according to element and either by core level orbital or by Auger transition levels, e.g., “In 3d<sub>5/2</sub>” and “In MNN”. A survey spectrum for solution-processed indium oxide is given in Figure 2-3 as an example. This survey was taken with a monochromated aluminum-anode x-ray source and scanned over the range of 86.58 to 1496.58 eV kinetic energy. After calibrating the spectrum from the analyzer in kinetic energy, binding energy is calculated by using Equation 5 and a known  $h\nu$  value of 1486.58 eV for the aluminum K<sub>α</sub> excitation of the source. The survey is then plotted in descending binding energy. The intensity comes from the counts of electrons detected at a specific kinetic energy, hence it is considered to be in arbitrary units. Thus, in one elegant spectrum, a qualitative chemical composition may be deduced.

#### Section 2.3.1.1 – XPS Data

XPS data is a rich information source of chemical composition at a material surface. The elements that are present, their relative ratios, and their chemical bonds can all be extracted from good XPS data. However, processing XPS data is not at all trivial, and like all analytical techniques, there are limits to the detection and resolution of chemical species. Although XPS data is used for quantification, the approximations involved may not yield data to the accuracy level desired, even when done carefully and conscientiously. Determining ratios of one chemical species to another is more reliable when looking for changes between samples.

The most basic information gleaned from an XPS spectrum includes the presence of specific core level peaks of the elemental constituents. Because peaks of different elements can overlap, the characteristic Auger peaks for an element are used for confirmation of the presence of an element, keeping in mind that trace amounts of elements, if they show their most intense

core level peak at all, may not necessarily show an Auger peak above the secondary electron background. Once the elements in a spectrum are identified, the next step is usually to account for the source of each element. XPS is highly surface sensitive, and even adsorption of ambient-air hydrocarbons frequently leads to the presence of a C 1s peak in an XPS survey spectrum. Sample processing and air exposure can affect the surface chemistry, and byproducts of these procedures can remain on the sample surface, causing unexpected elements to show up in an XPS spectrum.

The next level of XPS data processing involves a precise determination of the positions of the core level and Auger peaks. This is best done from high resolution measurements of the detailed regions of interest. The nature and degree of the shifts can indicate sample charging (which ideally should not occur), interface band bending, and variations in chemical environment. With regard to chemical environment, a sum of the measured binding energy of the core level peaks and the kinetic energy of the Auger peaks gives the so-called “modified Auger parameter ( $\alpha'$ )”.<sup>[28]</sup> When these are plotted in a Wagner plot, a more complete picture of the chemical environment can be seen. An example is given in Figure 2-4, which is a Wagner plot generated from the NIST XPS Database<sup>[30]</sup> for selected indium species. Note that the peak positions and the modified Auger parameter are different for metallic indium, indium chloride, indium oxide, etc.

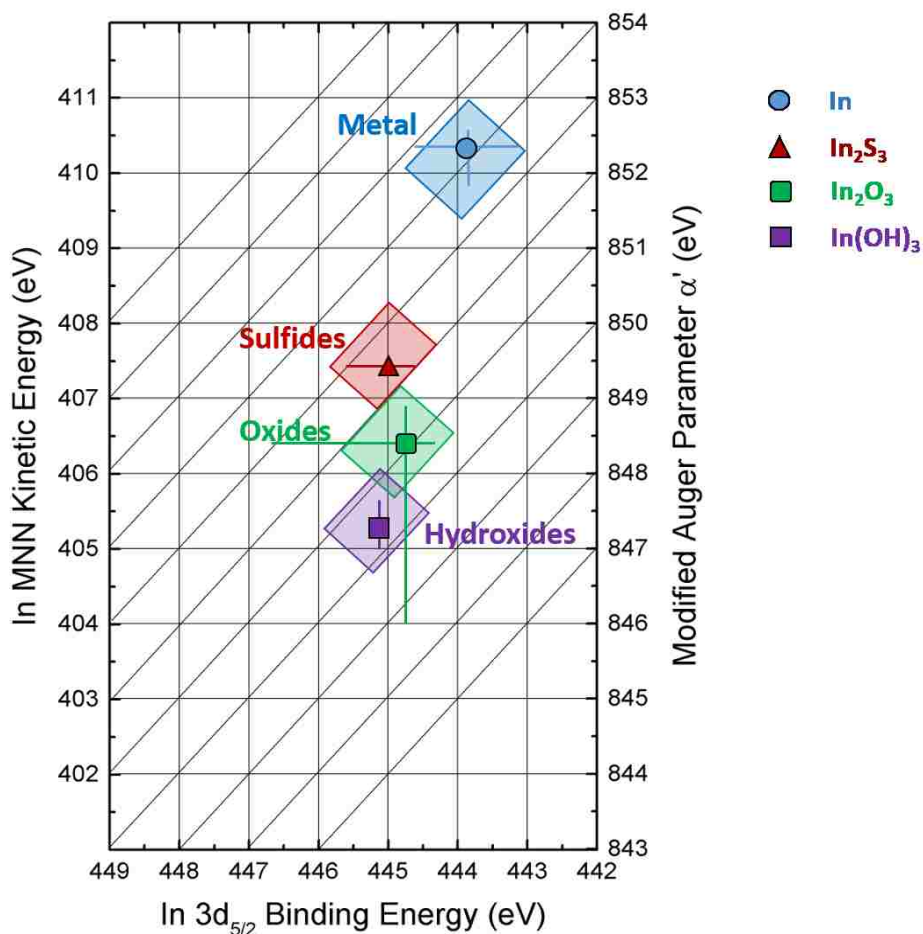


Figure 2-4. Wagner plot of several different indium species. Reproduced from a Wagner plot for indium from the NIST XPS Database [30].

In some cases, multiple compounds involving a single element can result in a broad and possibly oddly-shaped XPS core level peak. It may be necessary to use a peak fitting program to describe the spectra with the best approximations of multiple overlapping peaks and then identify the individual species contributing to the peak. Peak fitting is also used to calculate peak areas, which can then be used to approximate elemental ratios in a sample. Additional discussion of the parameters involved in peak fitting and an example of the code that can be used to define those parameters for use in the fity software is given in Appendix D.

### Section 2.3.2 – Ultraviolet Photoelectron Spectroscopy (UPS)

Less energetic UV photons are employed for UPS, and one or more of the excitations of a helium plasma are frequently used as a source. The process is similar to that of XPS, except that the lower excitation energy only allows excitation of electrons from the valence band or the highest occupied molecular orbitals (HOMOs), as depicted in Figure 2-5. As seen earlier in Figure 2-1, UPS is sensitive to the uppermost monolayers of a sample, which it makes it very sensitive to adsorbates and contaminants on a surface.

Also shown in Figure 2-5 is the concept of work function (WF or  $\Phi$ ). The work function is the minimum amount of energy required to remove an electron from a material (strictly speaking: to rest at a location outside of the surface, close enough to not be influenced by the

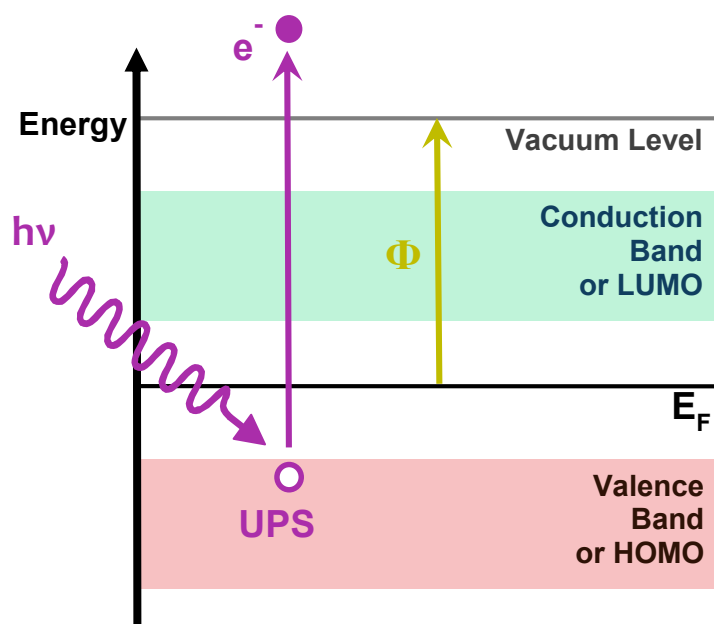


Figure 2-5. Diagram of UPS process and the concept of work function (WF, or  $\Phi$ ).

edges of that particular surface facet, but far enough to neglect any direct interactions with the surface). As such, it is strictly a surface property. It is very sensitive to surface contaminants and is useful for showing changes to surface due to surface treatments. When an interface is formed,



the work function of the substrate surface impacts the resulting band alignment at the interface, and hence modifying a surface to change its work function is an important area of research for electronic device development and interface optimization.

In practical UPS measurements, a known bias voltage is applied to the sample to give the electrons additional kinetic energy. This allows the measurement of electrons near the vacuum level, reduces interferences with, e.g., magnetic fields inside the vacuum chamber, and shifts UPS spectrum accordingly. Instead of being directly connected to ground, the sample is connected to ground via the bias voltage, which can be measured with a parallel multimeter. Measuring the position of a prominent metal peak (such as Au 4f<sub>7/2</sub>) with XPS with the bias attached and unattached gives a good quantification of the bias as experienced by the electrons going to the analyzer.

#### Section 2.3.2.1 – UPS Data

As with XPS, a UPS survey spectrum is useful for determining the kinetic energy ranges for detailed measurements of the secondary electron cutoff (SEC) at low kinetic energies and the valence band region at higher kinetic energies.

The SEC gives the lowest kinetic energy at which electrons can be removed from the sample surface; the SEC can thus be used to determine the work function. A linear fit of the slope of the SEC can be used to extrapolate a value for the work function of the surface. Figure 3-10 in Chapter 3 shows this with UPS data on metal oxides.

To determine the position of the valence band maximum (VBM) of a sample, the UPS spectrum is plotted with respect to the Fermi level ( $E_F$ ), which can be derived, e.g., from the

Fermi edge of a clean gold foil, measured with UPS using the same settings as the sample measurement.

## Section 2.4 – Inverse Photoemission Spectroscopy (IPES)

In Inverse Photoemission Spectroscopy, or IPES, incident electrons of known kinetic energy from a low-energy electron gun are focused on to the sample surface. The sample is grounded through a set-up that simultaneously measures the sample current (for normalization). At certain energies, electrons can relax to lower energy levels in the conduction band of the material and release the energy difference in the form of a photon. In particular, the conduction band minimum (for semiconductors) or Fermi energy (for metals) can be determined at the lowest impinging electron energy that provides photons compatible with the specific photon detection system.

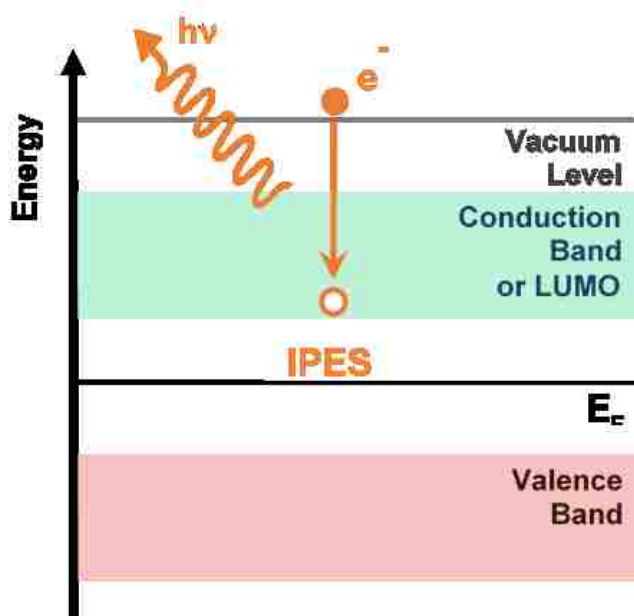


Figure 2-6. Diagram of the IPES process.

The data collected for IPES has two components: the number of photon counts at each step in the scan of electron energy, and the magnitude of the sample current at the same energy steps.

Setting up and operating the experimental equipment required for IPES is challenging, and hence few IPES systems are in regular operation worldwide. As with PES techniques, IPES must be done in an UHV chamber. Corresponding to energies between 2 and 20 eV, the photons emitted are in the UV range, and the detector must be chosen accordingly. Due to the very small number of photons emitted from a material during an IPES measurement, IPES requires photon counting. As electron source, a low-energy electron gun capable of high currents at low energies and low thermal spread is desirable. For the photon detector, different designs exist - the two types of detectors used in this work are an argon-iodine detector and a photomultiplier tube, as discussed in the following.

#### Section 2.4.1 – Ar-I<sub>2</sub> Detector

The argon-iodine (Ar-I<sub>2</sub>) detector is based on a Geiger-Muller tube<sup>[31]</sup> design, with a strontium fluoride window at the front, inside the vacuum chamber. Inside the detector, a mixture of iodine and argon at a pressure below atmosphere (approximately 300 mbar) fills the space between a positively charged needle-shaped anode and the grounded cylindrical detector wall. The voltage between the electrodes is usually at about 600 eV, but may be more or less depending on the Ar-I<sub>2</sub> mix, to achieve maximum counts without causing arcing in the detector. The detector has a photon band pass centered around 9.5 eV, and measurements are usually made in the range of 4-15 eV in electron energy.

### Section 2.4.3 – IPES Data Processing

To process IPES data, the photon counts are normalized by dividing by the sample current to account for the electron emission variation of the electron gun as a function of electron energy. Once normalized, the IPES data calibration of the energy axis follows a similar procedure to UPS calibration: IPES data of a clean gold foil is collected and normalized, then fitted with a Fermi function to find the Fermi energy, and this value is used to calibrate the energy scale of IPES measurements to  $E_F = 0$  eV. The conduction band minimum (CBM) of a semiconductor sample is then derived in similarly to the derivation of the VBM in UPS, as will be described in the following section.

### Section 2.5 – Extrapolation of VBM, CBM, and Band Gap

If both UPS and IPES data for the valence and conduction bands are available for a sample, they are frequently plotted together to form a visual picture of the experimentally measured band gap. A linear extrapolation of the data to the intercept of the x-axis provides a

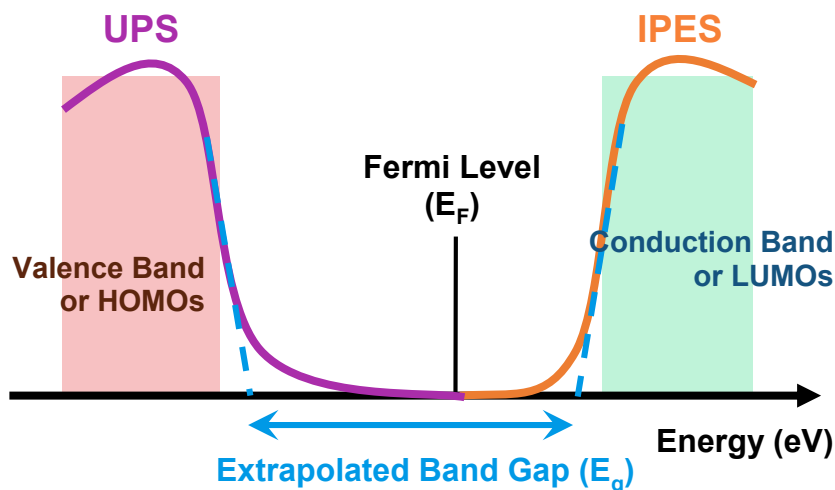


Figure 2-7. Diagram of the combination of UPS and IPES data, the extrapolation of the valence band maximum and the conduction band minimum, and the derivation of the electronic surface band gap.

numerical approximation of the maximum energy of the onset of the valence band and the minimum energy of the onset of the conduction band, i.e., of the VBM and CBM.<sup>[32]</sup> Combining the two allows a determination of the (experimentally derived) electronic band gap at the surface of the sample.

## Chapter 3 – SOLUTION-PROCESSED METAL OXIDES

### Section 3.1 – Background

Since ancient times, chemistry has been employed by metal workers, alchemists, scientists, and engineers with the goal of producing useful metals, metal coatings, alloys, and other compounds. Metal oxides have historically played roles as both a nuisance, as in the tarnish of decorative silver, and as a desirable product, such as aluminum oxide for its multiple uses as an abrasive, filler, and surface protectant (anodizing). From the standpoint of electronic circuitry, metal oxides may be useful or detrimental.

The adjacent occupied and unoccupied energy states that are available to electrons in a metal allow for conduction. There is no energetic separation between the occupied and unoccupied energy levels. The oxidation of a metal changes the distribution of energy levels available to electrons, resulting in an energetic separation between occupied valence band states and unoccupied conduction band states. This energetic separation, the band gap ( $E_g$ ), gives rise

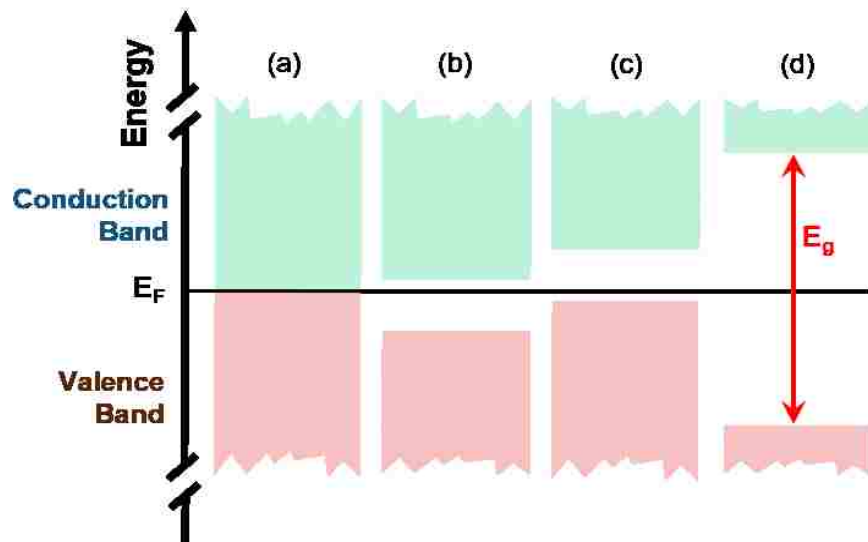


Figure 3-1. Diagram of electronic structure and band gaps for different materials: (a) metal, (b) n-type semiconductor, (c) p-type semiconductor, (d) insulator. The energy difference between the Conduction Band Minimum and the Valence Band Maximum is the band gap ( $E_g$ ).

to the properties of semiconductors and insulators, depending on the size of the bandgap (see Figure 3-1).

Materials with smaller bandgaps, e.g., semiconductors, can be quite conductive. Larger bandgaps result in increasingly insulating behavior. However, a material's bandgap also influences its optical properties. The size of the bandgap and the relative positions of the conduction band minimum (CBM) and valence band maximum (VBM) determine optical absorption and transmission characteristics. (For purposes of this discussion, "optical" includes not only the visible portion of the electromagnetic spectrum, but the near ultraviolet and infrared regions as well.) For example, a transparent insulator like sapphire (corundum-structured  $\text{Al}_2\text{O}_3$ ) has a very large band gap, while there is no band gap and no transparency for metals. Thus, a transparent conductive oxide (TCO) seems to be an implausible contradiction.

It should be noted that coatings of metals and metal oxides produced in thin films on the order of several hundred nanometers can have some degree of transparency. Transparency is not equivalent to 100% transmission, and light-matter interactions of elastic scattering (reflection) and inelastic scattering of unabsorbed photons still take place. Compared to a thin metal film of the same thickness, greater optical transparency is possible with a metal oxide. While the conductivity of a metal oxide may be less than a metal, the greater optical transparency of TCOs makes them extremely useful in devices like PVs and OLEDs.

TCOs can also be amorphous or crystalline, depending on their preparation method. Conductive amorphous films are desirable, because their conductivity does not depend on crystallinity. This allows them to be put on flexible substrates that would otherwise damage crystal structures and change their electronic properties. The solution process used here is

performed at temperatures lower than those needed to heat and crystallize the metal oxides being studied, and the result is an amorphous TCO thin film.

### Section 3.1.1 – Overview of ITO

Indium tin oxide (ITO), also known as tin-doped indium oxide, is a TCO frequently used as an electrode in many common electronic devices, for example, in OLED displays in smartphones. The bulk of the oxide is indium oxide, which is a TCO. By adding tin, usually in amounts between 3-10%, the conductivity is enhanced. ITO is a wide band gap, n-type semiconductor.<sup>[33]</sup> The wide optical band gap allows excellent transmission of light through the thin metal oxide layer. Applied to transparent substrates made of glass or polymer sheets, this combination of transparency and conductivity have made it a mainstay in the production of organic solar cells and LED displays.

ITO is typically applied to glass or polymers using physical vapor deposition techniques (PVD), and variations of vacuum sputtering are common. These techniques typically require expensive equipment, and sputtering is an indiscriminant process that leaves target material on more surfaces of the sputtering chamber than just the substrate. To achieve patterned circuitry, acid etching-lithography is used to remove selected areas of the sputtered ITO. ITO is insoluble in water or organic solvents.

ITO made from a metal-organic coordination complex, specifically acetylacetonate ligands in solution, was previously investigated in 1997.<sup>[18,19]</sup> Synthesizing the acetylacetonate solution, dip-coating the substrates, and annealing at 500 °C was used to produce crystalline films with good transparency and resistivity results; however, the resistivity was not as good as that of sputtered films at that time.<sup>[19]</sup> In the literature since 1997, there is very little to indicate that metal oxide formation from acetylacetonate or other organic ligand solutions ever became a



popular area of research. Advances in low-cost printing methods have now renewed interest in solution-processed metal oxides of all kinds, not just ITO. As a well-studied and readily available material, ITO is a good model for taking a new look at solution-processing of metal oxides.

## Section 3.2 – Precursor Solution

In this dissertation, metal ion-acetylacetonate (acac) coordination complexes were used as the source of transition metals for the metal oxide precursor solution:  $M(C_5H_7O_2)_y$  or  $M(acac)_y$ . The enolate anion of acetylacetonone (formal name: pentane-2,4-dione) is a strong nucleophile. Interactions occur between the  $\pi$ -orbitals of the acac molecule and the d-orbitals of the transition metal that favor a distribution of charge through the enolate anion and the formation of metal-oxygen bonds.<sup>[34,35]</sup> For most transition metals, two or three acac anions are involved in the coordination complex, depending on the oxidation state of the metal ion,<sup>[36]</sup> and due to steric effects, higher metal ion oxidation states often involve another anion species to achieve a neutral charge. As an example of the three-dimensional arrangement of metal and acac ions with another species, Figure 3-2 depicts the molecular structure of vanadyl acetylacetonate,

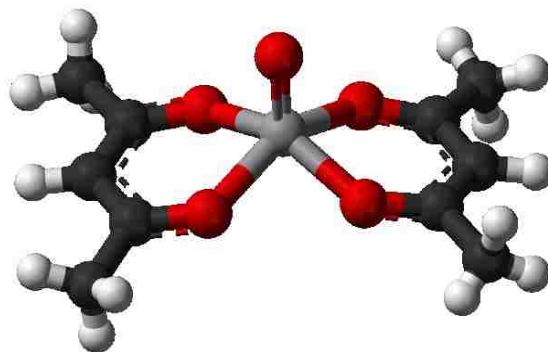


Figure 3-2. Vanadyl acetylacetonate molecular structure, showing vanadium-oxygen acac bonds and a double bond to a single oxygen atom to balance  $V^{4+}$  oxidation state. (Ben Mills, Wikimedia Commons, Vanadyl-acetylacetonate-from-xtal-3D-balls.png, based on [34].)

also known as vanadium(IV)-oxy acetylacetonate. Charge is distributed across the vanadium-oxygen acac bonds, but each acac anion has only a single negative charge. To balance the  $V^{4+}$  oxidation state, a single oxygen atom forms a double bond with the vanadium ion.<sup>[37]</sup>

The metal-acac coordination complexes used in this research were:

- Indium(III) acetylacetonate,  $In(acac)_3$
- Tin(IV) bis(acetylacetonate) dichloride,  $SnCl_2(acac)_2$
- Zinc acetylacetonate hydrate,  $Zn(acac)_2$

All acetylacetonate complexes were procured from Sigma-Aldrich.<sup>[36]</sup> Acac complexes were dissolved in 2-methoxyethanol, with no more than 3% acac compound to solvent by weight. This low concentration is partly due to the limits of solubility of some acac complexes, notably  $In(acac)_3$  in 2-methoxyethanol. However, it also keeps the overall amount of acac in the solution low, making the solution less viscous, and when spread in a thin coating, readily enables decomposition of the acac and solvent into gaseous products later in the coating process.

After the weighed amounts of metal-acac powder and 2-methoxyethanol were combined, the solutions were placed in an ultrasonic bath for 30-60 minutes. The solutions were then filtered through a 0.45  $\mu m$  PTFE filter to remove any particulates that might remain.

### Section 3.3 – The Thin Film Coating Process

Once made, the precursor solution was applied to different substrates using spin coating. The majority of substrates used were of AF-45 alkali-free glass in pieces of 15 x 15  $mm^2$  or 25 x 25  $mm^2$ . Cut pieces of gold-coated silicon wafer were used when a substrate without oxygen was

desired. The two spin coaters used for this research were made in-house for these specific sample sizes (see Appendix F). Substrates were cleaned by sonication, first for 15 minutes in acetone, then 15 minutes in isopropanol. The substrates were rinsed with additional isopropanol, spun on the spin coater to remove the excess solvent, and then placed on the hotplate to remove any solvent residues. The spinning speed and heating temperature in this preparation step were done using the same settings as the sample batch being made, typically 3200 or 3800 rpm and 450 °C.

A precursor solution was applied to the substrate before starting the spin coater. Up to 150  $\mu\text{L}$  of solution was applied to entirely cover the substrate surface, depending on the size of the substrate and the degree of wetting. The first thin film layer typically required more solution than the following layers, as the first-formed thin film usually improved surface wetting for subsequent layers, as observed qualitatively during the coating process. Once the solution was applied, the spin coater was started immediately. The coated substrate was spun for 30 seconds. Afterward, the substrate was placed on a pre-heated hotplate. This served to decompose and evaporate the organic portion of the solution, as well as anneal the remaining metal oxide. Unless otherwise specified, this annealing was conducted at 450 °C for four or five minutes. The substrate was then removed from the hotplate and allowed to cool briefly before repeating the process to form additional layers.

### Section 3.4 – Samples

The two main sets of samples for study of solution-processed metal oxides were IZO and ITO, but thin films of indium oxide (In-ox), zinc oxide (Zn-ox), and tin oxide (Sn-ox) were made concurrently for reference purposes. An IZO precursor solution was made at a ratio of 3:2

indium to zinc, and ITO precursor was formulated for a 19:1 ratio of indium to tin. Abbreviations “M-ox” will be used throughout the discussion, so as not to imply a specific stoichiometry.

Indeed, the true stoichiometry of many metal oxides varies.

IZO, In-ox, and Zn-ox sample sets were made with the following variations and measured with XPS:

- Annealing in air at 250 °C and 450 °C
- Heating in UHV to 200 °C

ITO, In-ox, and Sn-ox sample sets were made with the following variations and measured with XPS, UPS, and IPES:

- In air and in N<sub>2</sub>
- Low-energy ion treatment with Ar<sup>+</sup> ions at an energy of 50 eV in UHV

Samples of commercially-produced ITO were measured with the ITO series. With measurements of In-ox tying these two sample groups together, many of the results will be discussed with regard to solution-processed In-ox as a model for this specific process of making TCO thin films.

Samples made in N<sub>2</sub> in the thin film glove box were placed in Fluoroware™ containers and then vacuumed sealed in plastic and transferred to an N<sub>2</sub>-filled sample preparation glovebox for introduction to the UHV system for spectroscopic measurements. This procedure prevents adsorbates of water and hydrocarbon compounds in the air from coming into contact with the sample surface, and is important for distinguishing surface contamination from the air from the surface compounds that are a product of the solution process. Samples made in air were either introduced to the UHV system through the same sample prep glovebox or through an air-UHV load lock on the Scienta system. This was done immediately after making the thin films.

## Section 3.6 – Indium Oxide Samples Made in Air and N<sub>2</sub>

### Section 3.6.1 – XPS: Surveys

XPS survey spectra were taken to obtain a surface chemical profile of the samples. Figure 3-3 shows the survey spectra for an indium sample made in air, before and after ion treatment,

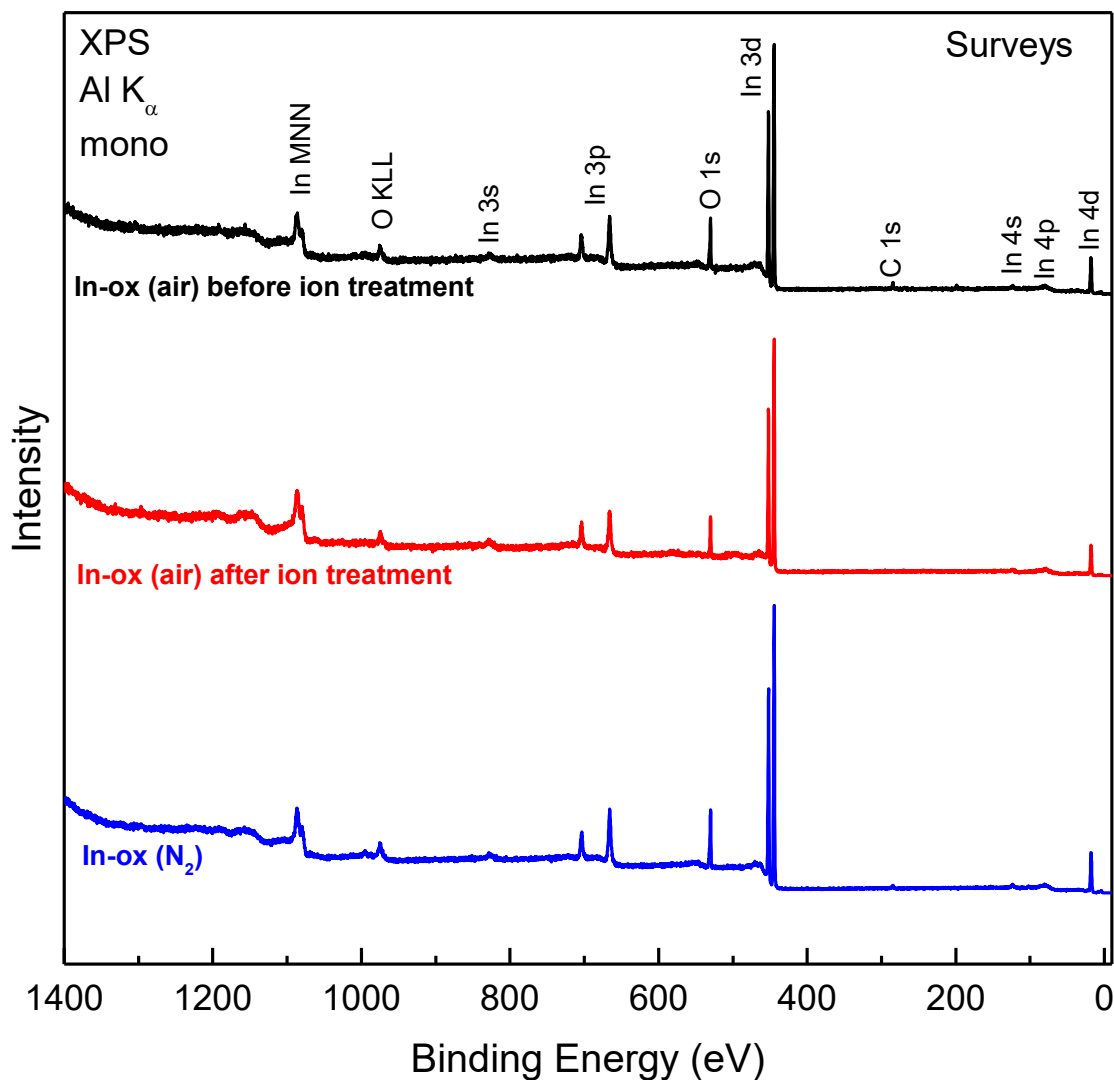


Figure 3-3. Three XPS surveys of two solution-processed indium oxides samples: a sample made in air before and after 50 eV Ar<sup>+</sup> ion treatment, and a sample made in N<sub>2</sub>. Taken with a monochromated Al K<sub>α</sub> x-ray source.

and a sample made in dry nitrogen. The core level and Auger peaks expected of indium oxide are present. For the untreated air sample and the sample made in nitrogen, the small C 1s peak indicates carbon-containing species on the surface. Ambient air exposure is a source of surface carbon contamination readily seen in XPS survey spectra. To get a better idea of the differences between these samples, XPS spectra were taken of limited regions with more data points around the peaks identified in the survey spectra. These detailed spectra will be discussed in the following sections.

### Section 3.6.2 – XPS: Carbon and Oxygen

The detailed spectra of the C 1s region show the presence of at least two carbon species for both samples, i.e., made in air and in nitrogen (Figure 3-4). Carbon is expected on the surface of a sample exposed to air. In the case of the sample made in nitrogen, the presence of carbon could be attributed to either a residue inherent in the solution coating and annealing process or from surface exposure of organic solvent vapors within the glovebox. After a 30-minute, 50 eV ion treatment, the carbon species are removed, as shown for the In-ox sample made in air. Because the presence or absence of oxygen species is also sensitive to air exposure and ion treatment, detailed spectra for the oxygen O 1s peaks are also shown in Figure 3-4.

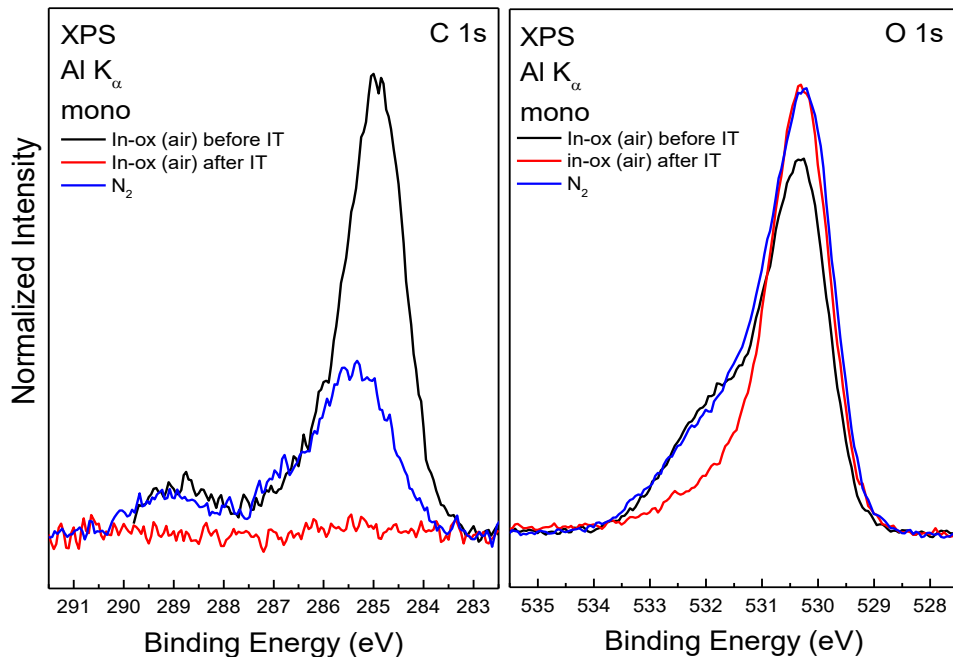


Figure 3-5. C 1s and O 1s spectra of an In-ox sample made in air and then ion treated, and an In-ox sample made in N<sub>2</sub>.

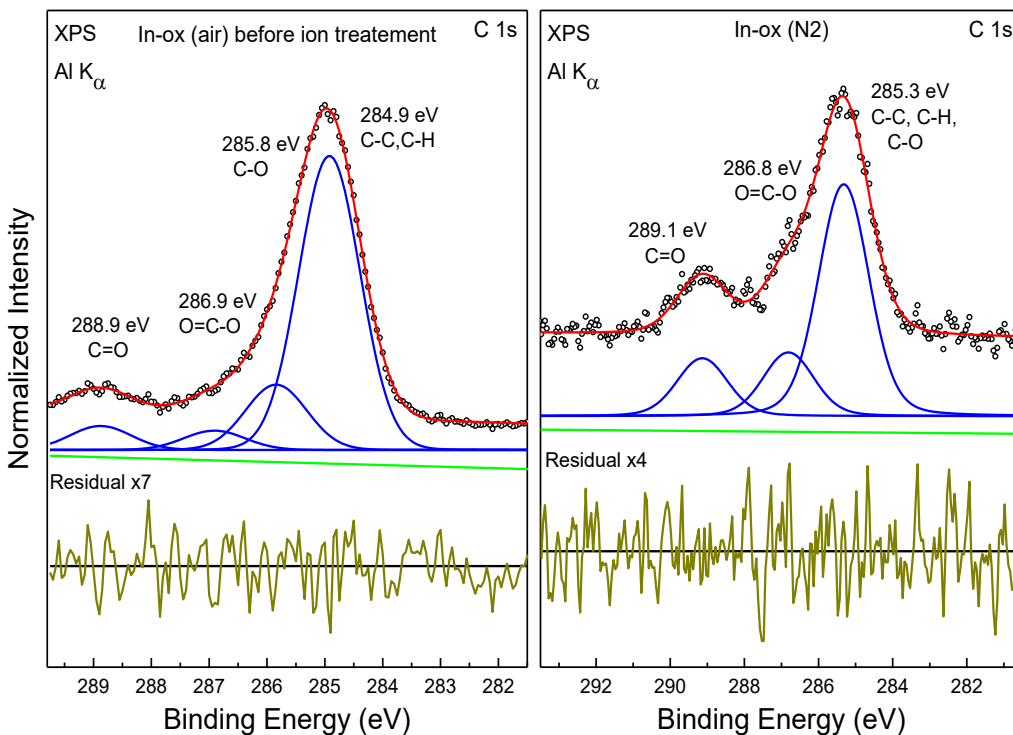


Figure 3-4. C 1s spectra after peak fitting. Positions of fitted peaks are given with most likely corresponding species (from [30]). The residual, i.e., the difference between data and fit, is shown below each spectrum on a magnified scale.

Peak fitting was done using the program fityk, version 0.9.4.<sup>[38,39]</sup> The carbon spectra (Figure 3-5) show several possible carbon bonds that contribute to the XPS C 1s peak. It appears from the difference in intensity and peak position of the largest peak that the sample made in air gained some additional carbon species due to air exposure compared to the sample made in nitrogen. For both samples, residual carbon-oxygen species at approximately 287 and 289 eV are likely due to precursor solution residue.

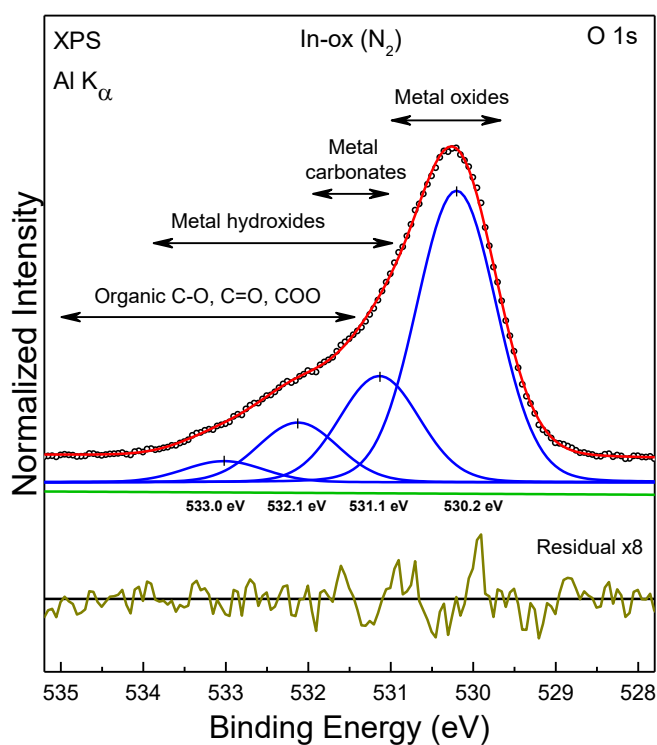


Figure 3-6. Peak fitting of O 1s spectrum of In-ox (N<sub>2</sub>). The approximate ranges of different oxygen species are indicated by arrows, based on data from the NIST XPS Database [30].

Peak fitting was done on the O 1s peaks as well. Figure 3-6 shows the fit of four peaks to the O 1s spectra of the indium oxide sample made in nitrogen. Furthermore, the figure shows the ranges of certain oxygen species, taken from reference data.<sup>[30]</sup> As seen with the carbon peak fits, some carbon is bound to oxygen, and therefore at least one and likely more than one carbon-



oxygen species contributes to the shape of the O 1s spectra. The most intense contribution falls in the range of metal oxides, and the carbon-oxygen species indicated in the C 1s spectra imply that one or more of the oxygen species near 532 eV and 533 eV represent the same carbon-oxygen compounds, likely as a residue from the organic precursor solution.

Peak fitting of the sample made in air, before and after ion treatment, seems to indicate that after removal of organic residues, some contribution from metal hydroxides may remain at about 531.3 eV. The removal of carbon-oxygen species by ion treatment indicates that these are surface residues. After ion treatment, the largest two contributions lie within 0.1 eV of the peaks for the sample made in nitrogen. This suggests that adsorbates from air are also contributing to the O 1s spectra for the sample made in air. The carbon-oxygen species present on the sample made in N<sub>2</sub> gives additional weight to the hypothesis that the residues are a by-product of the solution process.

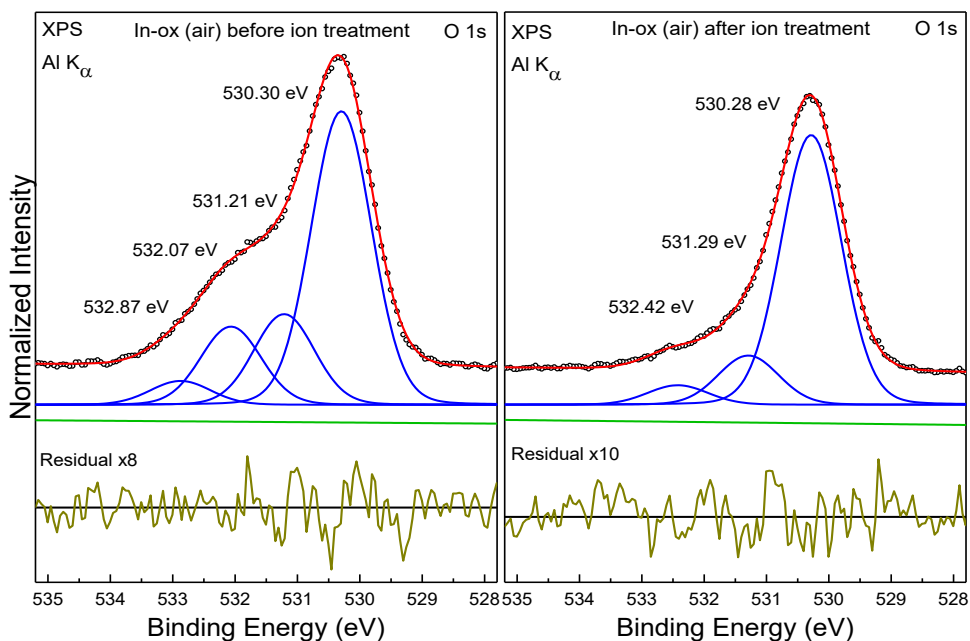


Figure 3-7. O 1s spectra after peak fitting, for the In-ox sample made in air, before and after ion treatment.

### Section 3.6.3 – Indium species

To evaluate the indium compounds formed in the solution process, the positions of the prominent In  $3d_{5/2}$  and In  $M_4N_{4,5}N_{4,5}$  peaks were measured, and the modified Auger parameter  $\alpha'$  was calculated. These measurements are presented in Table 3-1. The error associated with this data:  $\pm 0.05$  eV for the XPS and Auger data, and  $\pm 0.07$  eV for  $\alpha'$ . Interestingly, the values of  $\alpha'$  between the sample made in air versus the sample made in  $N_2$  are quite similar. After the air sample is ion-treated, the In MNN and  $\alpha'$  values change towards larger values. Plotting the data in Table 3-1 in a Wagner plot for indium (Figure 3-8), the indium at the surface of the ion-treated sample shows a stronger oxide character than the same sample before ion treatment and the sample made in nitrogen.

Sample	In $3d_{5/2}$ (eV)	In $M_4N_{4,5}N_{4,5}$ (eV)	$\alpha'$ (eV)
In-ox (air) before IT	444.9	406.1	851.0
In-ox (air) after IT	444.8	406.7	851.5
In-ox ( $N_2$ )	444.7	406.4	851.1

Table 3-1. Indium  $3d_{5/2}$  and  $M_4N_{4,5}N_{4,5}$  peak positions and  $\alpha'$  for samples In-ox (air), before and after ion treatment (IT), and In-ox( $N_2$ ).

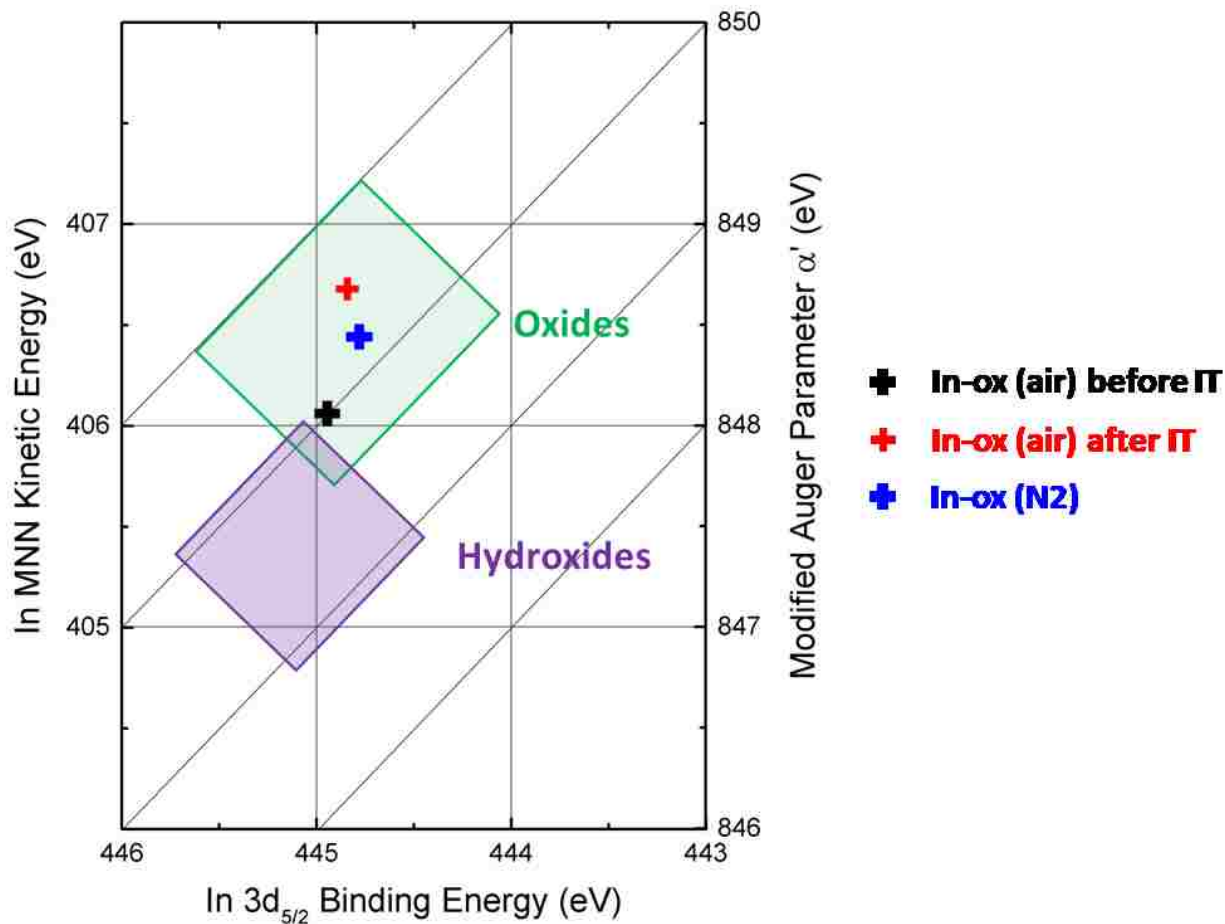


Figure 3-8. Wagner plot of In-ox samples made in N<sub>2</sub> and in air, before and after ion treatment. Indium oxide is the major contributor to the In  $3d_{5/2}$  and In  $M_4N_{4.5}N_{4.5}$  Auger peak positions.

#### Section 3.6.4 – Ion treatment and changes in work function and band edge position

Work function values were calculated using the SEC from UPS measurements, as described in Chapter 2. For In-ox (air), the work function before IT was 5.35 eV. This was lowered to 5.01 eV after ion treatment. The untreated In-ox (N<sub>2</sub>) sample had the lowest work function at 4.80 eV. These work function measurements have an error of  $\pm 0.03$  eV and are consistent with reported values of the work function of indium oxide, In<sub>2</sub>O<sub>3</sub>, prepared or treated with thermal methods.<sup>[40,41]</sup> The process by which indium oxide is made has an effect on its work

function, and post-processing surface treatments can be used to raise or low the work function as well.<sup>[42-46]</sup>

UPS and IPES data were used to extrapolate the VBM and CBM and their spectral “tails,” respectively. The results are shown in Figure 3-9. Error for these extrapolations is  $\pm 0.05$  eV for the VBM and  $\pm 0.1$  eV for the CBM. It is hypothesized that the larger (absolute) values of

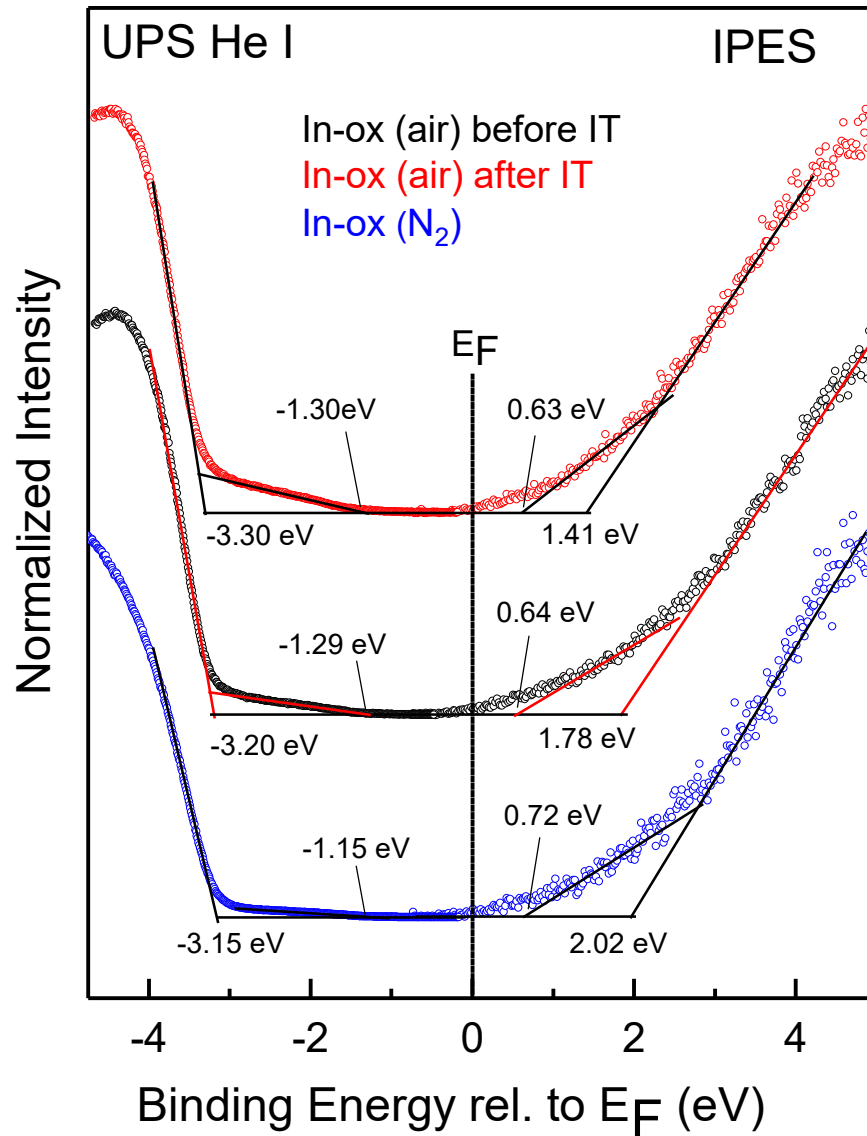


Figure 3-9. Band gap extrapolations of In-ox (air), before and after IT, and In-ox (N<sub>2</sub>).

VBM and CBM are responsible for the optical band gap and the transparency of the TCO, and that defect states create the tails within the optical gap that give rise to conductivity. This effect has been seen in UPS and IPES measurements of the TCO zinc magnesium oxide by Duncan et al.<sup>[47]</sup> Overall, the onsets and tails are quite similar for all three samples. In particular, all IPES spectra show a tail that extends all the way to the Fermi energy, suggesting a very strong n-type character of the TCO surface. Furthermore, the best approximation of the CBM from the dominant tail for all three samples is, within the error bars, essentially the same. The biggest variation is found for the dominant edge in IPES, which is highest (in energy) for the air sample, and also shifts towards lower energies after ion treatment.

### Section 3.7 – Indium Zinc Oxide (IZO)

Temperature effects were investigated with thin films of In-ox, Zn-ox, and IZO. Thin films made by annealing at 250 and 450 °C were measured with XPS. Made directly on a glass substrate, the films annealed at 250 °C were not conductive enough to prevent charging during XPS measurements. In contrast, films made on conductive IZO and annealed at 450 °C did not show charging effects during XPS measurements. As seen in the XPS survey spectra (Figure 3-10), more carbon was present in/on the samples annealed at 250 °C. This seems to correlate with mass spectroscopy measurements of the pyrolysis products of ITO thin films made from an acac precursor by Gallagher et al.<sup>[19]</sup>. In that study, most pyrolysis products were released at less than 100 °C, but another release of pyrolysis products occurred above 250 °C.

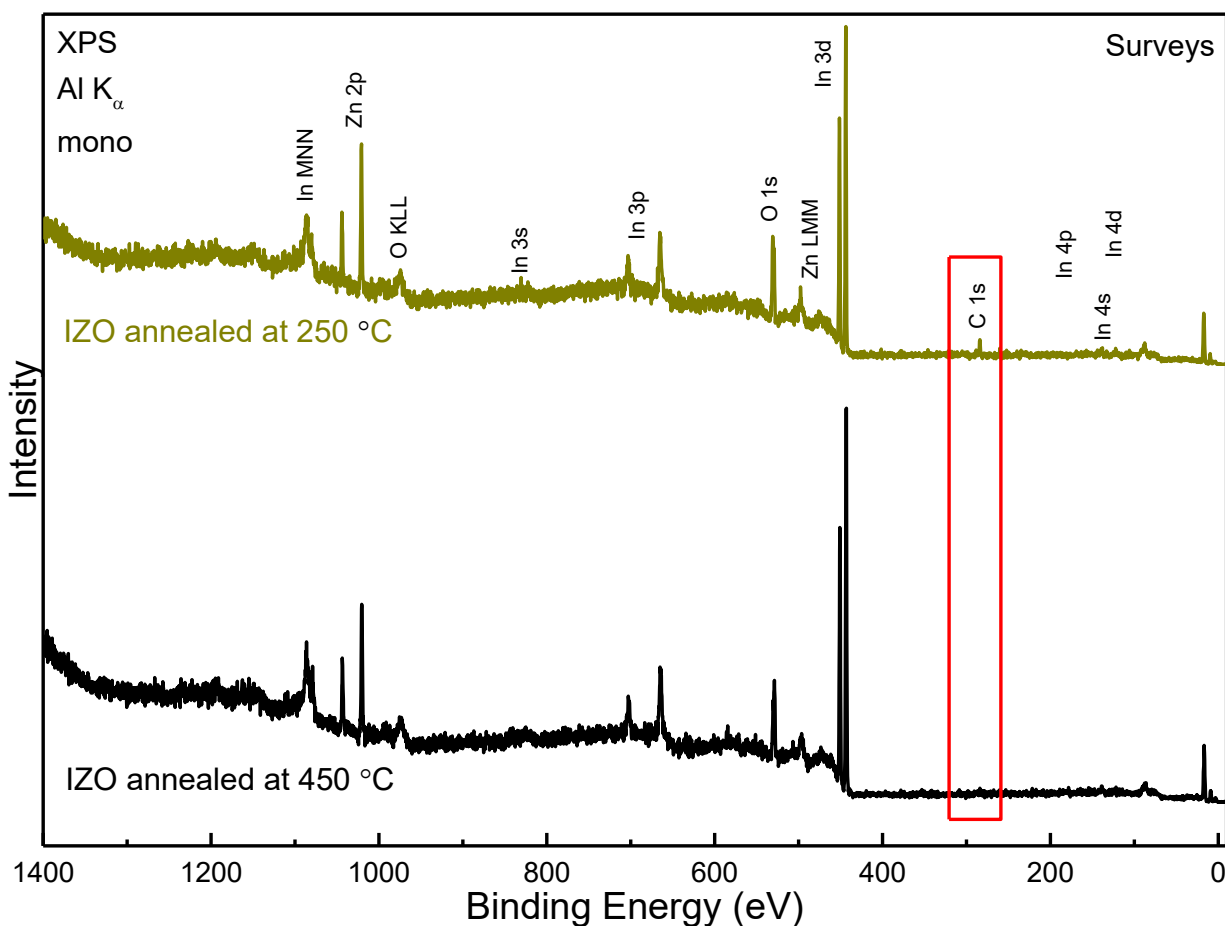


Figure 3-10. XPS Survey spectra of IZO annealed at 250 and 450 °C. A larger carbon signal is observed in the survey of the 250 °C sample.

Annealing the thin films at 450 °C provides sufficient thermal energy to cause this second desorption of precursor material. The thin films in this study were spin coated and annealed (or “pyrolyzed”) while the single layer of solution was still wet. Then, additional layers were applied in the same way, with four layers making a suitably conductive thin film for measurements. There may be a temperature below 450 °C that can be used to make conductive thin films with this process, but 250 °C is not adequate.

Ultimately, all of the solution-processed TCOs in this research showed the presence of metal hydroxides as well as metal oxides in the O 1s spectra; the IZO series was no exception (see Figure 3-11a). Interestingly, the position of these species is shifted towards higher binding energy for Zn-samples. The In-ox O 1s species lie at lower binding energy, and at a ratio of 3:2 of indium to zinc, IZO lies between the two and slightly closer to In-ox. The shape of the O 1s spectra in Figure 3-11a is similar to the indium oxide O 1s spectra discussed earlier. Here, the O 1s spectrum of IZO would represent a combination of oxides and hydroxides of both Zn and In, along with organic residues, consistent with the solution process.

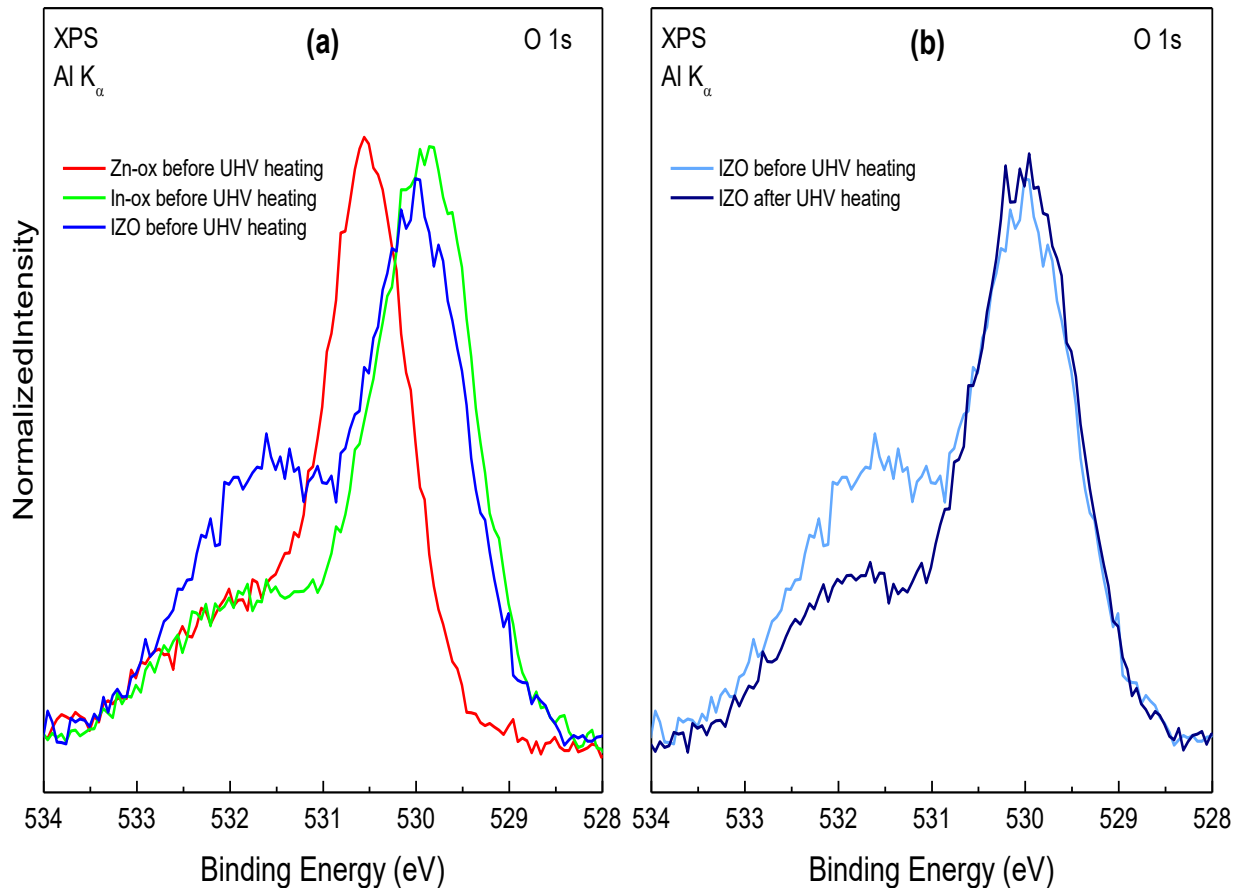


Figure 3-11. (a) XPS O 1s spectra of In-ox, Zn-ox, and IZO, before heating in UHV. (b) Change in the O 1s lineshape of IZO after UHV heating.

Instead of ion treatment, the IZO series of samples were heated in UHV to 200 °C and then measured again with XPS after returning to room temperature. Heating in UHV reduces the shoulder at higher binding energy that corresponds to the organic residues and metal oxides. The difference in the O 1s peak for IZO before and after heating is shown in Figure 3-11b. Compared to the ion treatment of In-ox, UHV heating leaves more organic residue and/or metal hydroxide on the surface.

### Section 3.8 – Indium Tin Oxide (ITO)

ITO thin films on glass and plastic substrates are readily available, so comparing solution-processed ITO (SITO) to a commercially-produced ITO on glass was a logical step to include in this study of solution-processed TCOs. ITO coated glass slides (Sigma-Aldrich product number 576352, 70-100  $\Omega$ /sq.) would be used for this purpose, as well as a substrate for

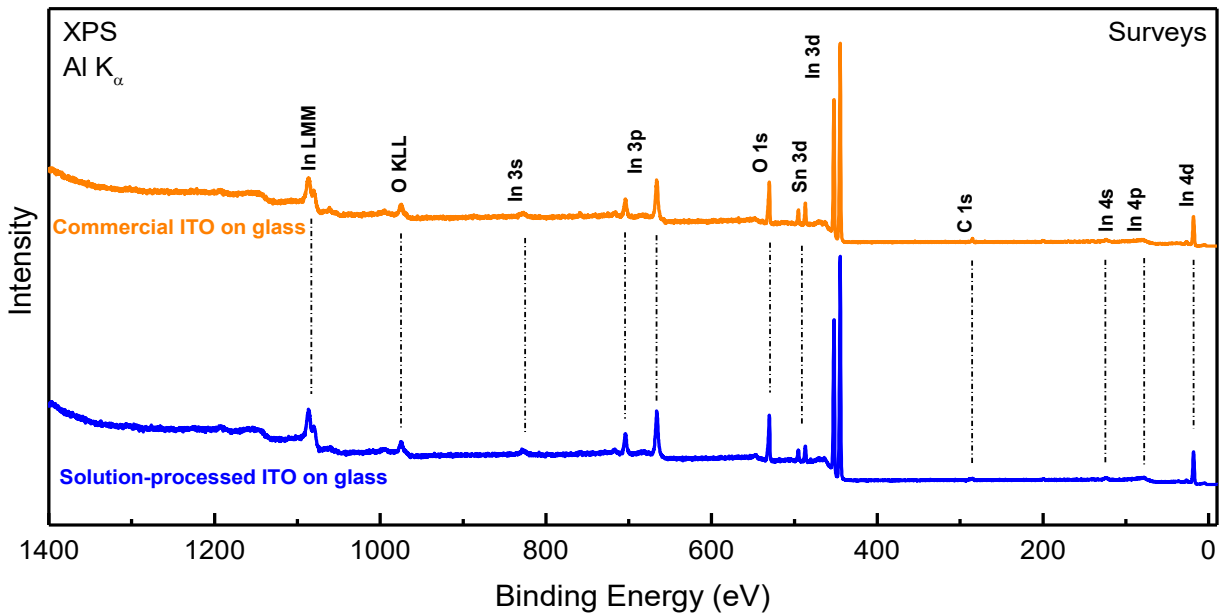


Figure 3-12. XPS survey spectra of solution-processed ITO and commercially produced ITO.



PEDOT:PSS thin films later. The precursor solution was made with 5% Sn to 95% In to mimic the ratio in commercial ITO.

The XPS survey spectra are very similar, although, due to the unknown period of air exposure, the surface of the commercial ITO (CITO) showed a larger signal of the carbon C 1s peak as compared to the SITO sample that was introduced into UHV immediately after it was made (Figure 3-12). In detail spectra, the metal hydroxide shoulder on the O 1s peak was also observed for the uncleaned CITO sample, and, as already discussed with the solution-processed In-ox samples, a reduction in hydroxide and the carbon peak was seen in XPS measurements after an ion treatment. The C 1s and O 1s spectra for both CITO and SITO were similar to the In-

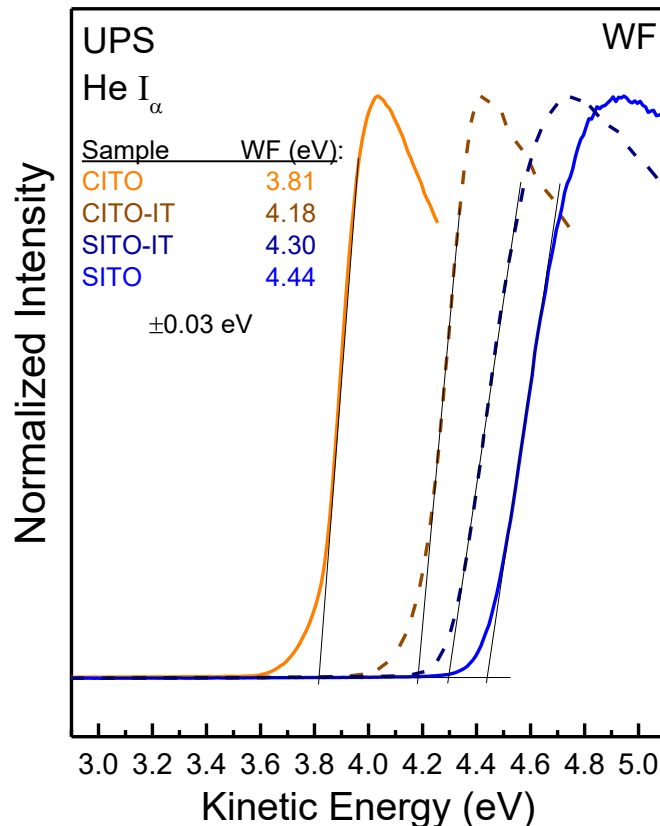


Figure 3-13. Work function (WF) determination of CITO and ITO, before and after ion treatment. Data is shown after subtraction of the applied bias voltage.

ox C 1s and O 1s spectra. Given that indium forms the majority of the metal oxide in both ITO thin films, the similarity to the In-ox samples is not surprising.

UPS measurements of the work function show distinct differences between CITO and SITO, both before and after ion treatment (Figure 3-10). The lower work function of the untreated CITO is consistent with a contaminated surface along with the increase in work function after ion treatment.<sup>[42,45,46]</sup> Higher work function values for ITO have been associated with a higher oxygen content following surface treatments.<sup>[42-45]</sup> One hypothesis for the higher work function of the untreated SITO surface is that the pyrolysis of the precursor solution serves a function similar to an oxygen surface treatment. Additional research with a wider range of measurement techniques needs to be done to understand the processes at the surface during the pyrolysis of the wet precursor thin film. In contrast to the CITO sample, the work function of the SITO sample is slightly lower after the ion treatment. One hypothesis for this is that protons are removed from metal hydroxides with ion treatment, leaving metal oxide sites with extra electrons at the oxygen atoms and at any defect sites created by the removal of oxygen atoms. Less energy would be required to remove these additional electrons.

As with In-ox, extrapolations of the VBM and CBM were done from UPS and IPES data, respectively. The results are plotted in Figure 3-14. The most noticeable effect of ion treatment is an increase in the tails adjacent to the VBM. It is hypothesized that the creation of additional defects from oxygen removal give rise to new defect states available to valence band electrons and thus lead to an increase in the VBM tails with ion treatment.

ITO is an n-type semiconductor, and as expected, both ITO samples show n-type character with the CBM closer to the Fermi level than the VBM, and again their tails are very close to the Fermi level. The VBM of CITO is shifted with ion treatment by about 1.7 eV toward the Fermi level, possibly due to the removal of surface adsorbates; however, a charging problem during the UPS measurements cannot entirely be ruled out. The onset of the VBM tail of CITO is shifted by 2.2 eV. In contrast, the VBM of SITO did not change as much with ion treatment, while the defect states near the VBM increased.

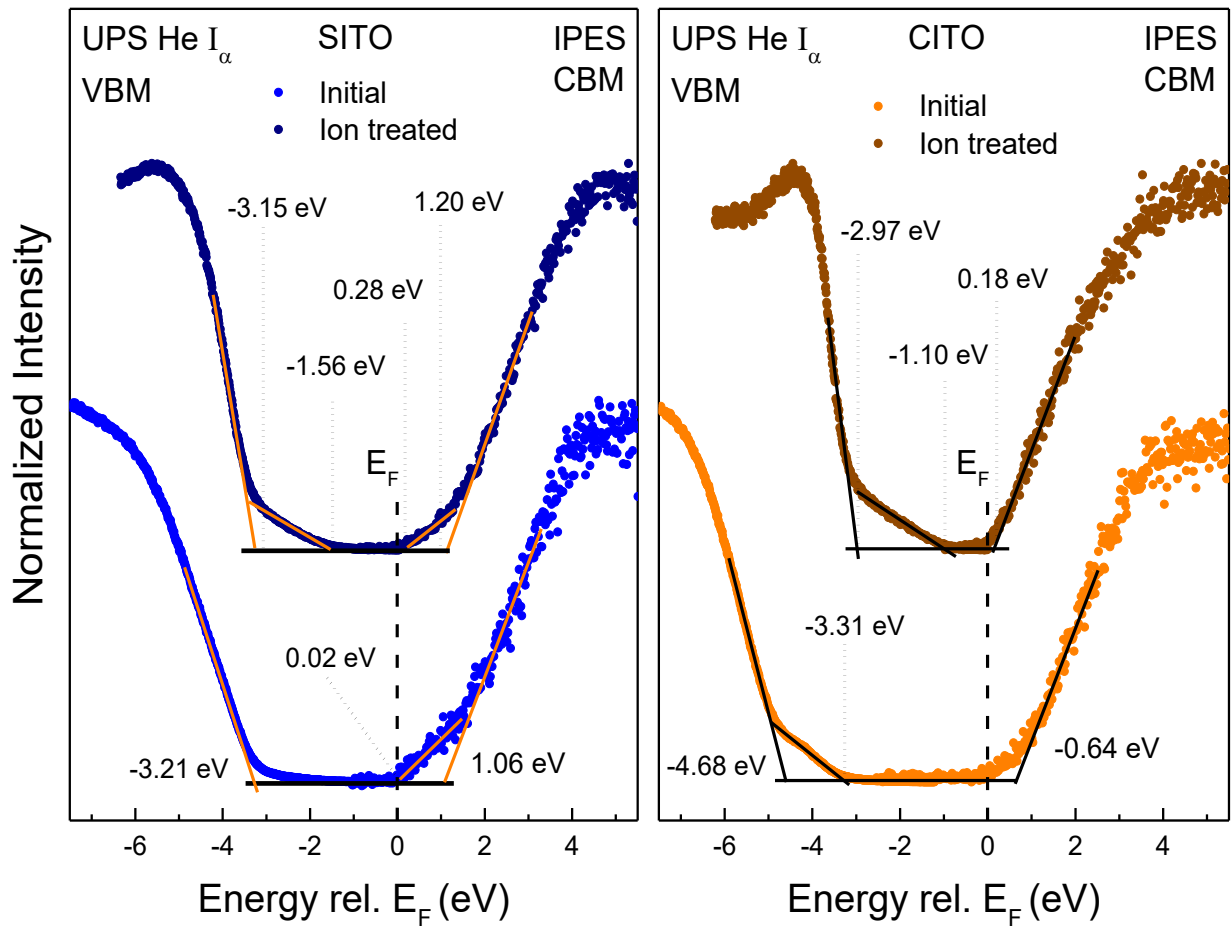


Figure 3-14. Extrapolated VBM and CBM from UPES and IPES data for SITO and CITO samples.

## Section 3.9 – Conclusions

No significant chemical differences were observed between solution-processed samples made in air and those made in nitrogen. This demonstrates that oxygen in the ambient air is not needed during the annealing part of the process, since oxygen is readily available in the acac and the solvent of the precursor solution. Indeed, the metal ion is already bound to the oxygen atoms in the acac, and only the carbon backbone of the acac needs to be removed. Also, carbon residues and surface hydroxides were detected for samples made under both air and N<sub>2</sub>, indicating that these are a by-product of the solution process. However, it was demonstrated that both can be removed via ion treatment, indicating that they are characteristic of the surface and not the lower layers of the TCO.

With regard to annealing, 250 °C is too low a temperature to produce a conductive thin film from the metal-acac precursor solution in this process. Considering the larger C 1s peak observed in XPS measurements of IZO, along with previous findings of Gallagher et al.<sup>[19]</sup>, it is hypothesized that carbon remains within the indium oxide in a manner that blocks electron movement. IZO, In-ox, and Zn-ox thin films annealed at 450 °C were heat-treated in UHV to 200 °C, and the hydroxide contribution to the O 1s peak was shown to decrease. This could be considered an alternative to an ion treatment for modifying the surface chemistry, but each method would require further study to determine if there are changes to surface roughness, conductivity, and other material properties.

ITO was successfully made using this solution process, and its chemical composition and electronic structure were very similar to commercially-produced ITO. A SITO sample and a

CITO sample exposed to air even have similar surface chemistry in terms of carbon and hydroxide species, both of which can be removed with ion treatment. The band gaps are similar, though not exactly alike. A better comparison between the two would require that the same glass be used as a substrate and that the thickness of the thin film be made the same for both. However, both are made predominantly of indium oxide, and the indium oxide establishes the base of the material properties. Processing modifications and post-processing treatments could make the films close to identical in terms of the measurements done here.

Interestingly, the solution-processed ITO had a higher work function than the commercial ITO, and its work function was lowered after ion treatment. Like the CITO sample, it was expected that the work function of the SITO would increase with the removal of surface carbon and hydroxides, yet the opposite occurred. With and without ion treatment, the SITO had a larger work function than the CITO. The higher work function of the untreated SITO would be desirable in a device like a solar cell where the ITO functions as an anode. Recombination of positively charged holes and negatively charged electrons created by the absorbing layer is a significant problem in photovoltaics, especially OPVs. The anode collects the positively charged holes and must have a large work function to prevent charge recombination from occurring before the charges can be transferred out of the device. This could be a worthwhile area of further study to better understand the solution process and how it modifies the surface properties of the TCO.

Another potential advantage of the SITO is the creation hydroxides at the surface. Hydroxides can improve surface wetting characteristics. In the case of applying an aqueous solution of PEDOT:PSS on ITO, surface wetting becomes very important for thin film formation, as will be discussed further in the next chapter.

There is no doubt that the metal-acac solution process used is capable of making TCO thin films. It produces a metal oxide, and that metal oxide determines the dominant chemical and electronic properties that were examined in this research. Processing effects cannot be entirely ignored or dismissed as irrelevant, however, and additional research into process effects on conductivity and the effects of surface treatments on solution-processed metal oxides is needed.

In conclusion, the desired metal oxides were easily produced using a precursor solution of metal-acac ligand in organic precursor solution in the process described. A mixture of metal hydroxides and organic species were formed along with the metal oxide and could be removed by ion treatment. ITO was successfully made using the solution-process, and it had properties very similar to those of commercially-produced ITO. Further research into comparing the conductivity, crystallinity, and other properties of solution-processed ITO and commercial ITO would be valuable in evaluating the potential use of solution-processed ITO in optoelectronic devices.

## Chapter 4 – PEDOT:PSS THIN FILMS

### Section 4.1 – Introduction

Poly(3,4-ethylenedioxythiophene) (PEDOT) is a  $\pi$ -conjugated polymer with high conductivity, stability, and good optical transparency in its oxidized state.<sup>[48,49]</sup> By itself, however, PEDOT has poor solubility, and the oxidized form is paired with a soluble anion to make solution processing possible. The most common anion used for this purpose is polystyrene sulfonate (PSS), either from its acid form (PSSH) or its sodium salt (PSS-Na),<sup>[49]</sup> to form an aqueous dispersion with PEDOT. Commercially available dispersions can be made with different ratios of PEDOT to PSS and different overall concentrations of polymers. These solutions are usually acidic, although neutral pH solutions are also available.<sup>[36]</sup>

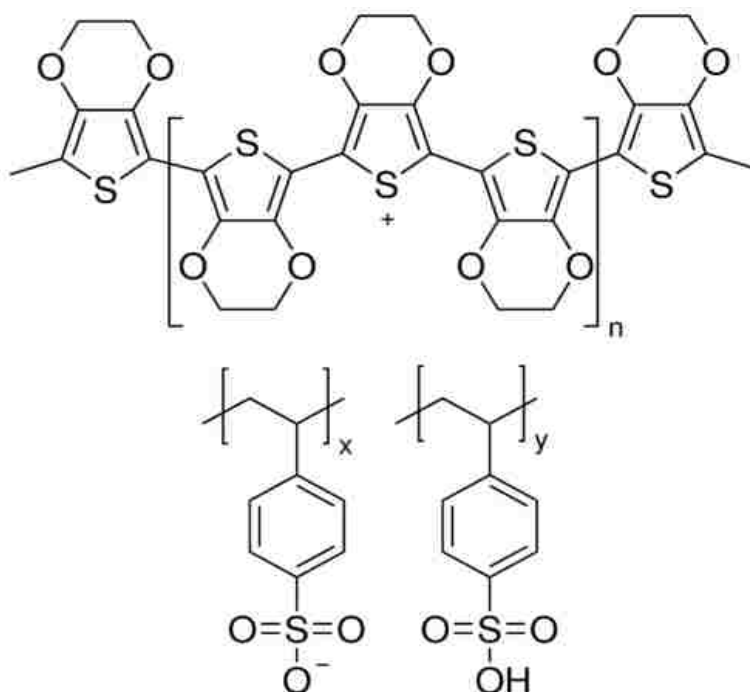


Figure 4-1. Molecular structures of PEDOT (top) and PSS (bottom). From [36].

The acidic dispersions can etch many surfaces, including the surface of ITO. Diffusion of indium ions into PEDOT:PSS films has been reported, and it is likely due to acid etching that occurs when the PEDOT:PSS dispersion is first applied.<sup>[50,51]</sup> Still, the acidic, aqueous dispersion of PEDOT:PSS is widely used, hence it was selected for this research.

A substantial amount of research on PEDOT:PSS has taken place since the 1990s, and research continues to the present day, resulting in a vast body of literature. Undoubtedly, part of this is due to its use in OLEDs, an organic electronics success story. The effects of processing conditions were recognized early on, with research being done on a multitude of factors, including annealing time,<sup>[52,53]</sup> annealing temperature,<sup>[53–55]</sup> solvent effects,<sup>[56–60]</sup> additives,<sup>[61–67]</sup> PEDOT:PSS ratios and inhomogeneities,<sup>[63,68]</sup> coating methodology,<sup>[52]</sup> post-process treatments,<sup>[48,66,67,69]</sup> and studying the resulting effects on morphology,<sup>[52,57,58,63,65,66,70–73]</sup> layer thickness,<sup>[52,54,55]</sup> crystallinity,<sup>[60,66,74,75]</sup> charge transport,<sup>[71,76]</sup> conductivity,<sup>[52,53,57,58,61–65,70,74,75,77–81]</sup> and device performance.<sup>[54,55,60,63,64,82]</sup> Research on PEDOT:PSS continues to the present day, including using PEDOT:PSS for new device applications, such as an electrode replacement for ITO in optoelectronic devices<sup>[63,83]</sup> and low-cost biosensors.<sup>[84]</sup>

The original motivation for working with PEDOT:PSS was simply to achieve a good conductive thin film upon which to place other organic materials to build multilayer organic electronic devices, such as a small-molecule solar cell. Making thin films from the PEDOT:PSS dispersion proved to be very challenging, and choosing from the vast amount of literature to develop a suitable recipe for the solution was no easy task. Of the spectroscopic data collected from the thin films, further study of the inhomogeneities in PEDOT to PSS ratio became a new focal point, since varying ratios are known to have effects on conductivity and device performance.<sup>[63,68]</sup>



## Section 4.2 – Experimental: Solution Development

High-conductivity PEDOT:PSS was purchased from Sigma-Aldrich<sup>[85]</sup> (product information in Appendix C). Initial experiments in spin coating (3200 rpm) the PEDOT:PSS dispersion on cleaned glass, ITO, and Au-coated substrates demonstrated a lack of wettability between the aqueous dispersion and the hydrophobic surface. Consequently, these first experiments showed that the PEDOT:PSS covered parts of the substrate surfaces, but did not create films. Experiments with 99.5% reagent grade isopropanol (IPA) coated on the substrate surface and added to the PEDOT:PSS dispersion showed improved wettability and a better tendency to form a complete film across the substrate surface.

Another set of experiments using ethylene glycol (EG) and sodium dodecyl sulfate (SDS) as additives to the PEDOT:PSS dispersion were conducted, along with warming the PEDOT:PSS solution before application.<sup>[82]</sup> The purpose of these experiments was to enhance the wettability by reducing surface tension and viscosity, based on additives and techniques found in the literature. Wei et al. reported improved conductivity by adding 3% EG to PEDOT:PSS.<sup>[66]</sup> Fan et al. enhanced conductivity with anionic surfactants, and achieved conductivities 500 times higher than PEDOT:PSS with no additives by adding sodium dodecyl sulfonate.<sup>[61]</sup> The structurally similar anionic surfactant SDS was used in a ratio of 2.5:1 SDS to PEDOT for the 1% Sigma-Aldrich dispersion (product number 768642) used in this study. Four solutions were compared, with EG and SDS added in the amounts mentioned above: PEDOT:PSS + EG, PEDOT:PSS + SDS, PEDOT:PSS + EG + SDS, and PEDOT:PSS with no additives. Wettability and thin film continuity was observed qualitatively during the spin coating and annealing process.

These experiments in enhancing wettability were unsuccessful, with SDS and PEDOT:PSS solutions being unfilterable through a 0.45  $\mu\text{m}$  PTFE filter, and no noticeable improvement in wettability for the others. This could be due to several possible factors: aging of the PEDOT:PSS dispersion, a negative impact of prolonged warming of the solutions, and non-optimal ratios of additives to PEDOT:PSS. One hypothesis is that the use of SDS, combined with solution heating, causes too much segregation of PEDOT from PSS, resulting in unfilterable material. Fan et al. proposed that the mechanism for improving conductivity with anionic surfactants was a change in conformation of the PEDOT chain as surfactant anions replace PSS anions along the PEDOT chain (see Figure 4-2), and it was noted that the solutions with surfactants became less stable.<sup>[61]</sup>

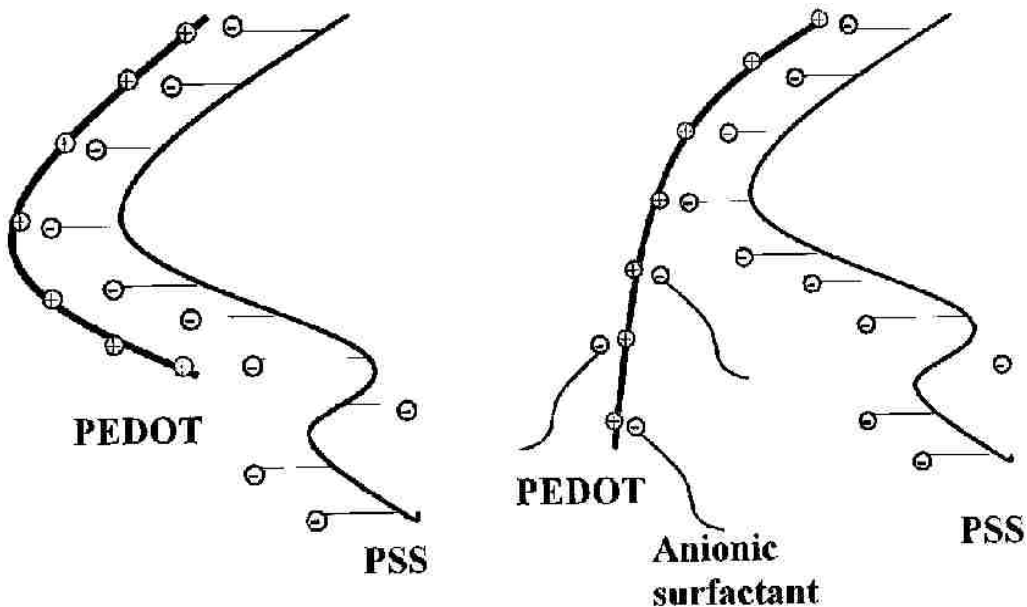


Figure 4-2. Change in PEDOT chain conformation due to surfactant ion replacement of PSS, as proposed by Fan et al. Modified from [60].

Developing an optimal PEDOT:PSS solution based on the wealth of research available in the literature could easily be a dissertation unto itself. Here, the main priority was obtaining a PEDOT:PSS thin film adequate for an analysis of its chemical and electronic properties. The final

recipe chosen for this dissertation was a solution made from 3% EG, 20% IPA, 77% PEDOT:PSS dispersion by volume to enhance conductivity (with EG) and improve wettability (with IPA). This formula provided decent filterability, wettability, and thin film formation when spin coating.

For this solution, the optimal processing conditions were found to be a spin speed less than 4000 rpm. Based on the literature, the thickness of PEDOT:PSS thin films is controlled largely through speed of the spin coater. For thicker films using this solution recipe, lower spin speeds would be needed.

### Section 4.3 – Thin Film Process

Substrates were cleaned in the same manner as substrates for the metal oxide thin films using acetone and IPA. After mixing the PEDOT:PSS solution, the solution was sonicated in a water bath at approximately 35-40 °C. Filters were placed in a plastic bag to warm in the water bath with the solution, as well as a pre-wetting solution for the filters composed of 3% EG, 20% IPA, and 77% NanoPure water. The pre-wetting solution was forced through the filters first, then air, then followed by the PEDOT:PSS solution.

The filtered solution was spin coated onto the substrates at 3200 rpm for one minute, using the single-speed spin coater in air. The resulting thin films were annealed on a 130 °C hotplate for eight minutes. 3800 rpm was used with the variable speed spin coater; 4800 rpm was also tried, but this resulted in films that only partially covered the substrates.

## Section 4.4 – Multiple Layers

To prepare a film consisting of multiple layers, a sample series was made on 15 x 15 mm<sup>2</sup> glass substrates. Note that no reference to coating multiple layers of PEDOT:PSS on a single substrate could be found in the literature, and hence the samples were either annealed after each layer (“each”) or annealed at the end of the entire multilayer application (“end”). It was quickly observed that beyond two layers, slippage and removal of the previous layer occurred if it had not been annealed. Resistance was checked for each sample, measuring from opposite corners, to ensure suitability for PES measurements. A trend was observed in that multiple layers, with annealing between layers, showed reduced resistivity. The results are shown below in Table 4-1.

<b>PEDOT:PSS Sample</b>	<b>Corner-to-Corner Resistance (k<math>\Omega</math>)</b>	<b>Notes</b> (Resistance values fluctuate for all samples)
1 layer	2-3	
2 layers, end	1.7	
3 layers, end	~2-4	Slippage; uneven film
2 layers, each	1-2	
3 layers, each	0.7-1.0	
4 layers, each	0.6-0.9	

Table 4-1. Resistance in multilayer PEDOT:PSS samples.

The measurements above were not done specifically with a study of conductivity in mind, but simply to check that the samples were sufficiently conductive for PES, given that they are deposited on insulating glass substrates. A more rigorous investigation of the relationship between the number of layers, layer thickness, conductivity, and charge mobility parallel and perpendicular to the film surface could be an interesting study.

## Section 4.6 – Results: PEDOT:PSS Inhomogeneities and Beam Damage

Figure 4-3 shows the survey spectrum of a PEDOT:PSS thin film on glass. Both PEDOT and PSS contain carbon, oxygen, hydrogen, and sulfur, but each polymer has different properties and a different function in the dispersion and the final film/device. Sodium in the survey spectrum most likely originates from the PEDOT:PSS dispersion, since the sodium salt of PSS is frequently used to make these dispersions. Because alkali-free glass was used as a substrate, the sodium cannot originate from the glass, Nitrogen is not present in the glass substrate nor the PEDOT:PSS dispersion, but this sample was made under nitrogen atmosphere in a glove box. It is possible that microscopic pockets of nitrogen were trapped in the polymer film during the spin

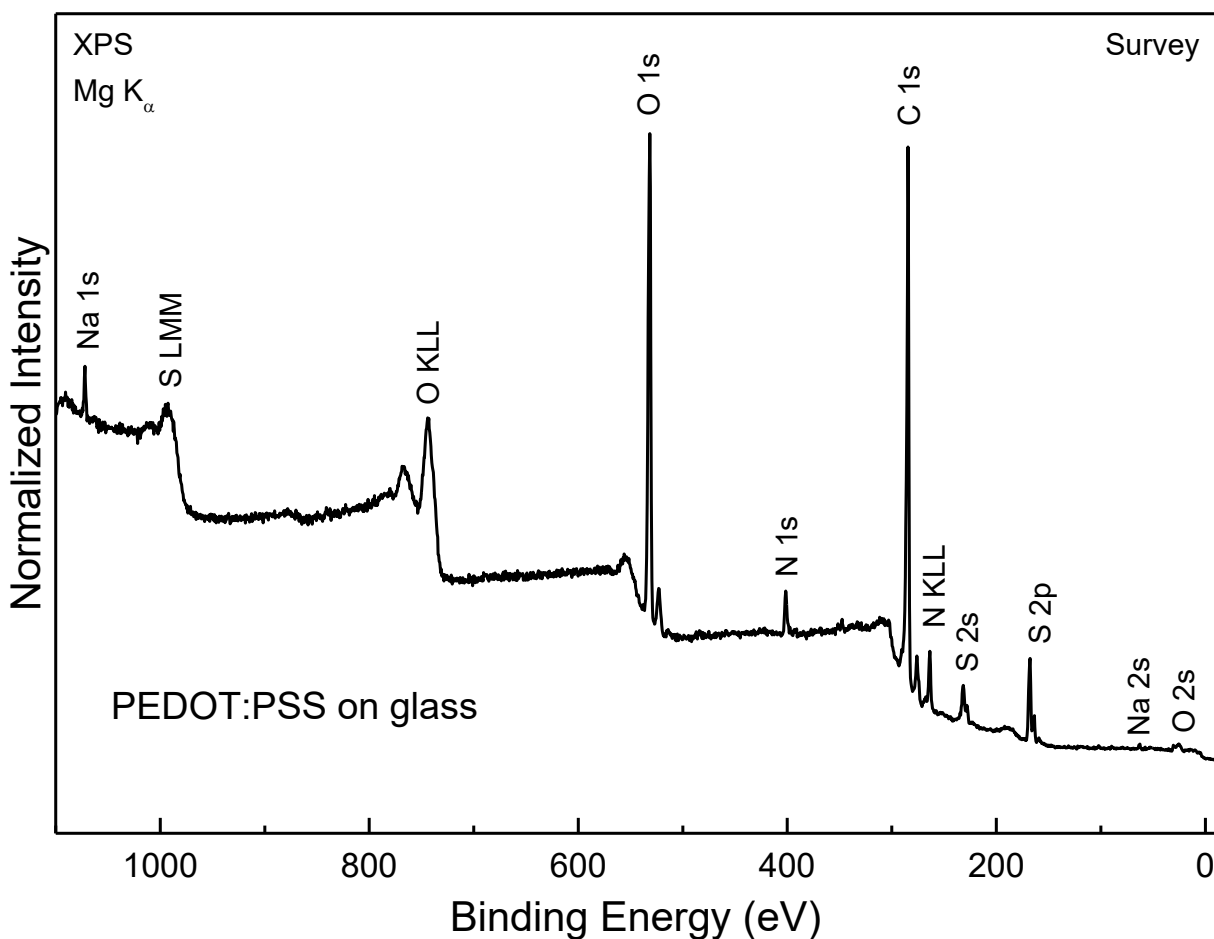


Figure 4-3. XPS survey spectrum of a PEDOT:PSS thin film on glass.

coating and drying process.

XPS measurements show a chemical environment for PEDOT's thiophene sulfur atoms quite different from that for sulfur in the sulfonate groups of PSS, so XPS spectra of the sulfur 2p region are the best way to verify the presence of PEDOT and PSS and differentiate between the two. Figure 4-4 shows an XPS spectrum of the S 2p region for PEDOT:PSS (on SITO) with separate spin-orbit doublets for each polymer. Reference values for different sulfur species<sup>[30]</sup> and for PEDOT:PSS<sup>[49]</sup> are also shown.

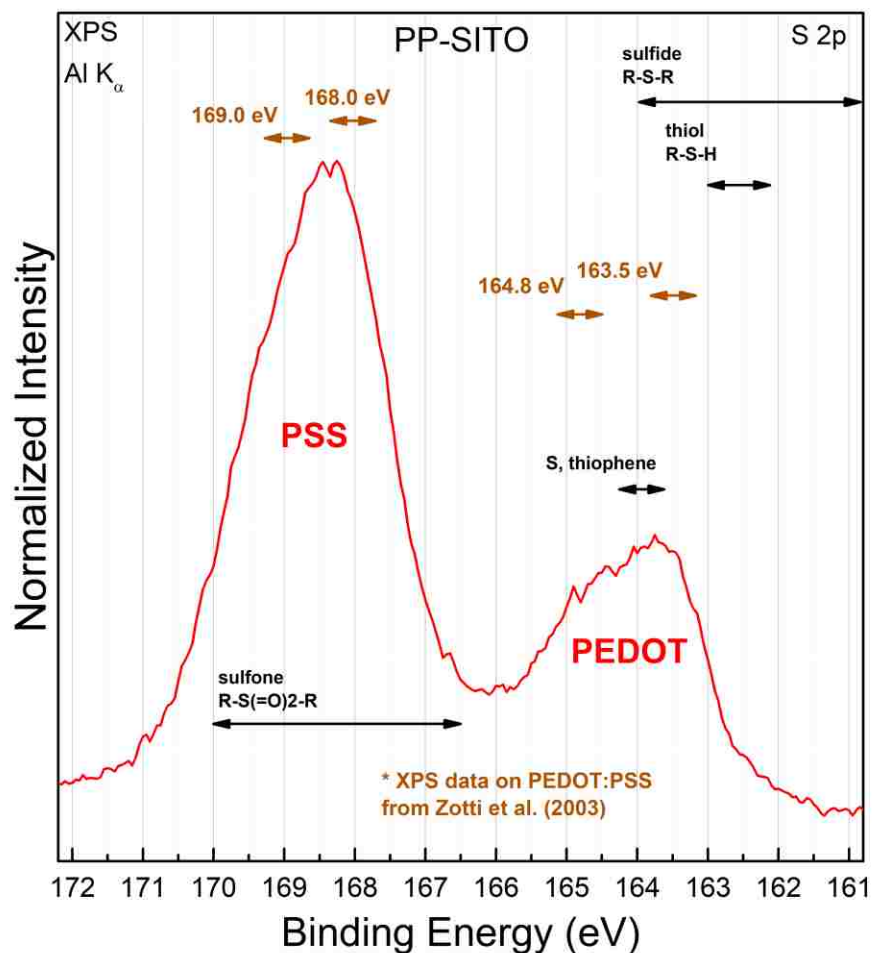


Figure 4-4. Example of the S 2p region in XPS, indicating how different chemical species can be differentiated. Reference XPS data on PEDOT:PSS from [49] were used for initial verification of species. Reference values (in black) are taken from [30].

#### Section 4.6.1 – Sample inhomogeneities and beam damage

The first XPS measurements on PEDOT:PSS (PP) involved measurements at different spots on both SITO and CITO 25 x 25 mm<sup>2</sup> substrates to check the film homogeneity. Pictured in Figure 4-5 is the PP-SITO sample on the measurement arm inside the UHV chamber. The dark blue area is PEDOT:PSS. In the transparent area on the left side of the clip, a portion of the PEDOT:PSS film wiped away before annealing, should a measurement of the ITO substrate be needed. A 25 x 25 mm<sup>2</sup> sample is too large for the sample plate that is used, so an edge from each samples was cut off for sample mounting. In relation to the original spin-coated film, Spot 3 is closest to the center of the substrate, Spot 1 is closest to the corner, and Spot 2 is between the edge and the center; this applies to both samples. For convenience, PP-SITO and PP-CITO will be used to denote the two different samples by substrate.

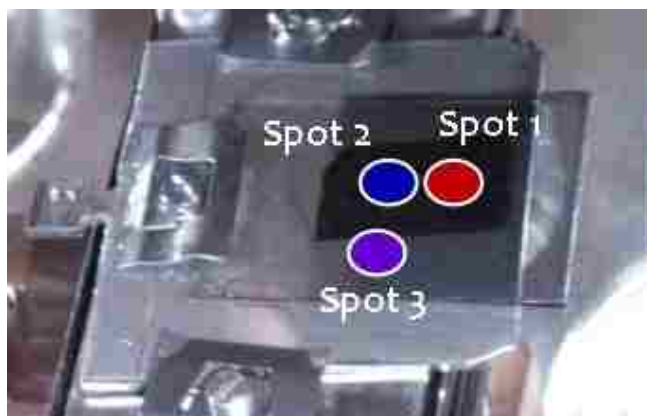


Figure 4-5. Photograph of the PP-SITO sample. The approximate locations of three measurement spots are marked. The sample was cut along the edge closest to Spot 3.

From the S 2p data, it was immediately apparent that both samples were not homogeneous. Multiple measurements were done at each spot to evaluate x-ray beam damage, and these results are combined in the following graphs. Figure 4-6 shows the different peak

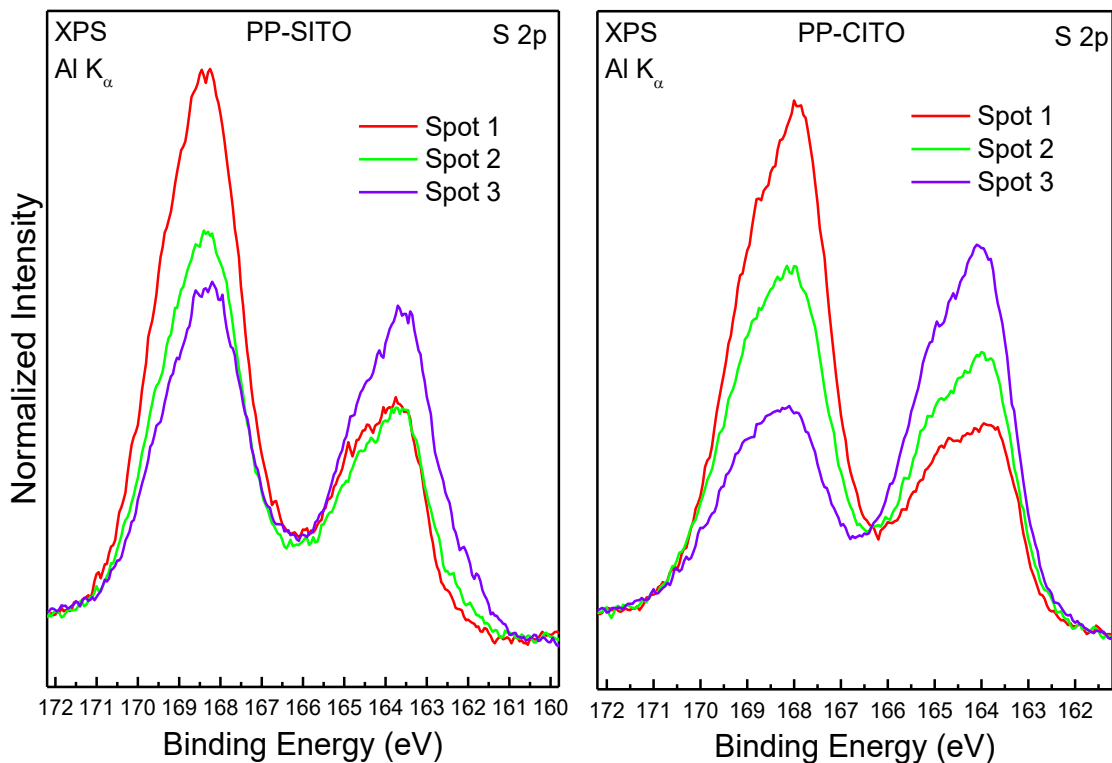


Figure 4-6. XPS measurements of the S 2p region for PP-SITO and PP-CITO, showing the differing intensities of PEDOT (ca. 164 eV) and PSS (ca. 168 eV) with respect to measurement location on the samples.

intensities of PEDOT (at ca. 164 eV) and PSS (at ca. 168 eV) according to measurement location. For both samples, a larger relative PEDOT signal is observed at Spot 3, which is close to the original center of the samples, while a larger relative signal of PSS is characteristic of Spot 1, closer to the corner. Figure 4-7 additionally shows the multiple measurements made at each spot location, with three measurements at Spot 1 (red, orange, yellow), three measurements at Spot 2 (green, light blue, dark blue), and two measurements at Spot 3 (purple and pink). This illustrates the effects of beam damage at each spot, and shows that, although beam damage decreases the PSS signal while increasing the PEDOT signal, the amount of change due to beam damage is smaller than the difference in signals due to sample inhomogeneity.



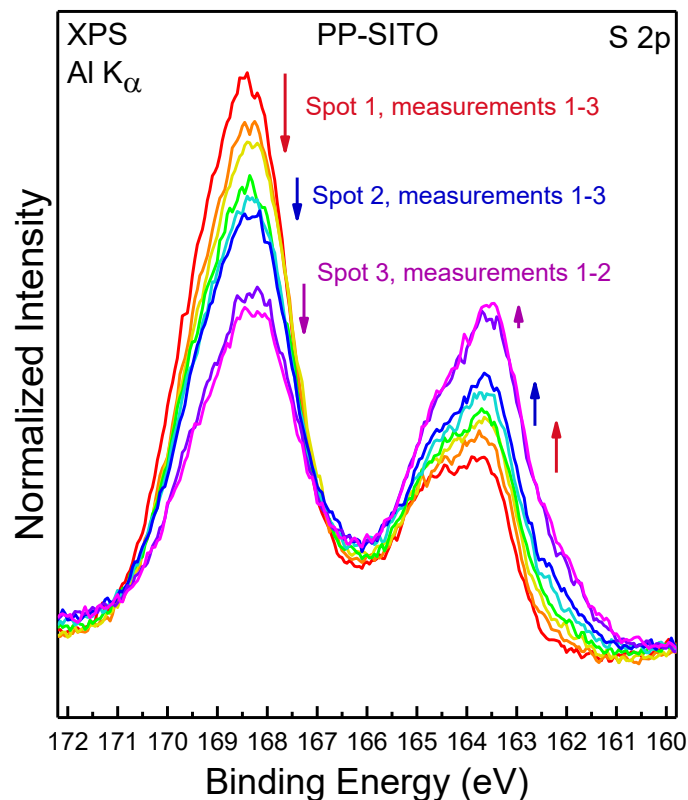


Figure 4-7. Multiple XPS measurements of the S 2p region on PP-SITO. With each measurement, the PSS peak intensity decreases and the PEDOT peak intensity increases at each measurement spot.

It is not unusual to see a decrease in peak intensity of some species due to beam damage, since the ionizing radiation of x-rays and ultraviolet light can easily break chemical bonds and decompose molecules, especially organic molecules. However, we point out that the increase in PEDOT *signal* cannot, conceivably, be due to an actual increase in the number of PEDOT molecules during measurement. Rather, we argue that the PSS molecules are decomposed as part of the observed beam-induced changes, possibly including a desorption of (the S-containing and other) functional groups into the vacuum. In turn, the attenuation of PEDOT photoemission signals is reduced, hence leading to an apparent relative increase in S 2p intensity. This model correlates with the non-conductive PSS being more readily destroyed by ionizing radiation than conductive PEDOT [REF!!]. We speculate that, because PEDOT is conductive, it can more

readily draw electrons from the electronic ground of the sample to replace electrons emitted in the XPS measurement. Less able to do the same, PSS is more likely to be damaged due to electron losses. It would be very interesting to perform *in situ* FTIR or mass spectrometry measurements during XPS and UPS measurements of these organic materials to better understand beam damage effects.

#### Section 4.6.2 – Determining PEDOT:PSS ratios with peak fitting

The peaks characteristic of PEDOT and PSS are actually composed of peak contributions of multiple sulfur species. To obtain accurate measurements of the areas under the peaks corresponding to each polymer, peak fitting must be done. The program fityk, version 0.9.4, was

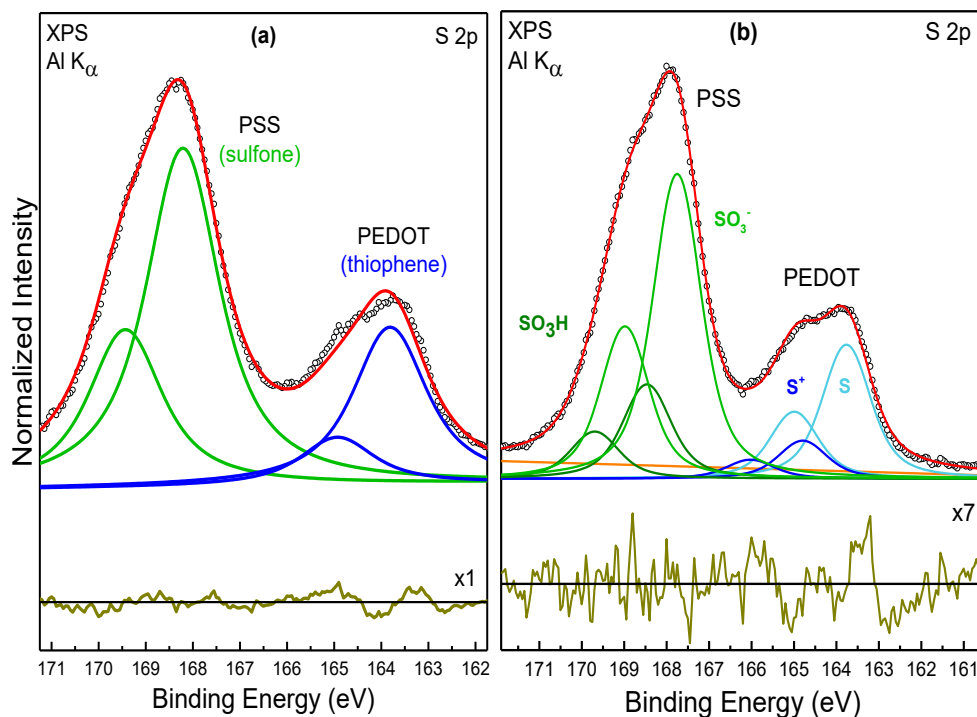


Figure 4-8. Peak fitting of XPS S 2p spectra for PEDOT:PSS. (a) Fitting a S 2p doublet for each polymer gives a poor fit. (b) A better fit is possible when the ionic species are also considered [46,47,85], requiring a total of four S 2p doublets in the fit.

used for this purpose.<sup>[38,39]</sup>

For peak fitting S 2p spectra, a spin-orbit doublet, representing the  $2p_{1/2}$  and  $2p_{3/2}$  peaks, must be used for each species. For sulfur, they must be constrained by a peak separation of  $\sim 1.20$  eV and a peak area ratio of 2:1 for  $2p_{3/2}$  to  $2p_{1/2}$ .<sup>[30,86]</sup> For PEDOT:PSS, it would seem that a doublet for the thiophene in PEDOT and a doublet for the sulfonate in PSS would be sufficient. However, this does not give a good fit, particularly for PEDOT, because it does not account for the possible simultaneous presence of ionic and neutral forms of both PSS and PEDOT in the thin film (Figure 4-8).<sup>[48,49,87]</sup>

To achieve a good fit, four doublets were fitted to the S 2p spectrum, as shown in Figure 4-8b. Details of the peak fitting parameters and functions were written into code to be used by fityk to load the desired data files and set up the parameters, functions, and constraints for fitting; an example of the parameters used in the code is shown in Appendix D. The calculated areas of the fitted Voigt functions were summed for the peaks representing the PEDOT and PSS

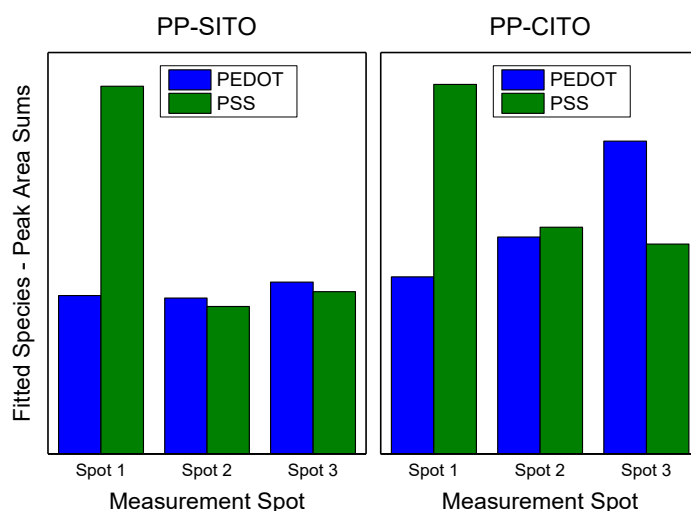


Figure 4-9. Ratios of peak area sums for PEDOT and PSS at different sample spots for PEDOT:PSS on SITO and CITO substrates.

contributions, respectively. These area sums are depicted in the bar graphs of Figure 4-9 for PP-SITO and PP-CITO, separated by measurement spot.

Although Spot 3 for PP-CITO shows a higher PEDOT contribution than the same spot for PP-SITO, this is probably due to overall sample inhomogeneity, and not necessarily a substrate effect. But it is clearly visible that a higher relative PSS contribution is found at Spot 1 of each sample, i.e., closer to the corners. It makes sense to interpret this as an effect of the spin-coating process, because of the greater solubility of PSS in aqueous dispersion than that of PEDOT. After deposition of the solution on the substrate, the centrifugal force during spinning pushes the aqueous solution away from the center of the substrate. This solution carries PSS with it, and at the areas farthest from the center, the corners, PSS not carried off the substrate with the excess solution will tend to accumulate.

#### Section 4.6.3 – UPS Results

UPS measurements were made on a second sample set of PEDOT:PSS on 15 x 15 mm<sup>2</sup> SITO and CITO substrates. These had either one or two layers, and are referred to as PP1-SITO, PP2-CITO, and so forth, with the number representing the number of PP layers. UPS measurements of the secondary electron cutoff to derive the work function gave unexpected results when measuring on different spots. For metals and many semiconducting materials, the SEC of UPS measurements is a steep, smooth slope. A stepped SEC was observed (Figure 4-10) at different locations of PP1-CITO. The most likely hypothesis of the source of this step is that fringe-field effects, induced by distortions of the electrostatic bias field between sample and electron analyzer near the corners of the sample may be the source of the stepped SEC.

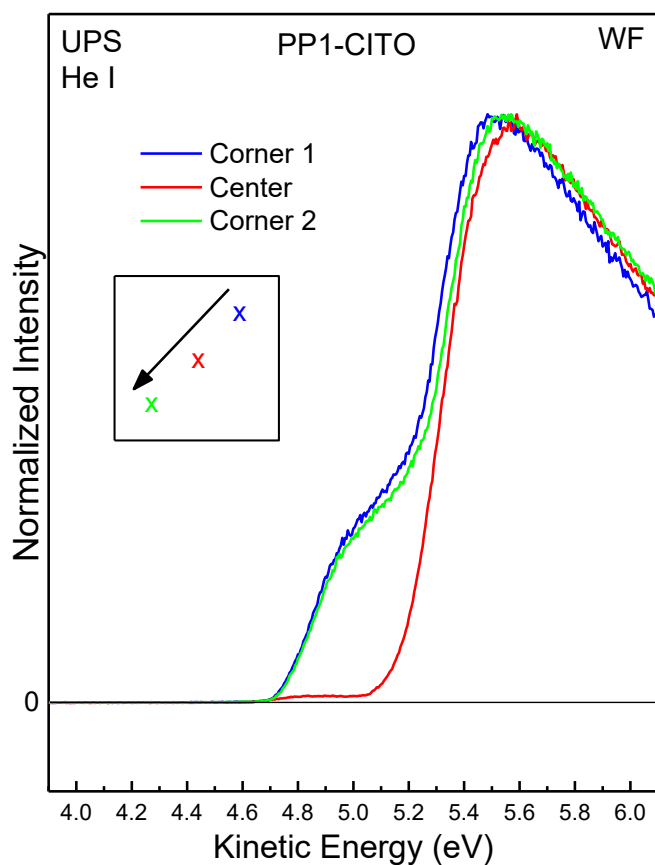


Figure 4-10. Secondary electron cutoff (SEC) measurements of PP-CITO-2 at different sample spots (after correction for the bias voltage).

Nevertheless, an alternative hypothesis based on lateral inhomogeneities is also worth considering. In this hypothesis, the stepped SEC is caused by differing ratios of PEDOT to PSS. The inhomogeneity of the PEDOT:PSS thin films has already been demonstrated, showing an excess of PSS closer to the sample corners. These UPS measurements were also performed on different spots, and a diagram in Figure 4-10 shows the order of measurement and the relative positions of the measurement spots on the square substrate. Thus, the stepped SEC spectra correspond to the areas with more PSS relative to PEDOT. There is a very small step at the same lower work function for the center spot, which would reflect a lower amount of PSS contributing

to the overall SEC. Note that there is also a slight shift toward higher work function as measurements progress. There is likely some slight overlap of measurement spots, and the hypothesis is that beam damage is continuing to remove PSS and raise the work function of the surface. Work function measurements of other PP samples on glass and on ITO also showed variations of SEC profiles shown in Figure 4-10. Some were stepped, and some were not. The inhomogeneity of the PP thin films appears to be process-dependent, not substrate-dependent.

Reported values of PEDOT:PSS work function are around 5.0 eV with variations of approximately  $\pm 0.3$  eV, which are believed to be caused by varying amounts of PSS in the top layer.<sup>[62]</sup> The extrapolated work function values in Figure 4-10 are centered around 5.1 and 4.7 eV, respectively, consistent with these reported values.

Knowing the effects of x-ray beam damage, XPS measurements were taken after UPS to assess UV damage. The center spot of the sample was measured. The spectra show a marked decrease in PSS signal with an increase in PEDOT signal, indicating significant damage to the PSS (Figure 4-11). Many organic molecules and materials are damaged by UV radiation, and PSS is no exception. Spectra collected using the Helium I $\alpha$  excitation are presented here, but data were also collected using Helium II $\alpha$ , using the monochromatized UV source on the VG Scienta system.

It may be possible that one of these excitations is less damaging than the other, or that one of the Helium  $\beta$  excitations could cause less damage to the PSS. Extending this hypothesis to other organic molecules, it may be advantageous to experiment with an organic material using the different settings of a monochromatized UV source to find the least damaging excitation energy for the material at hand.

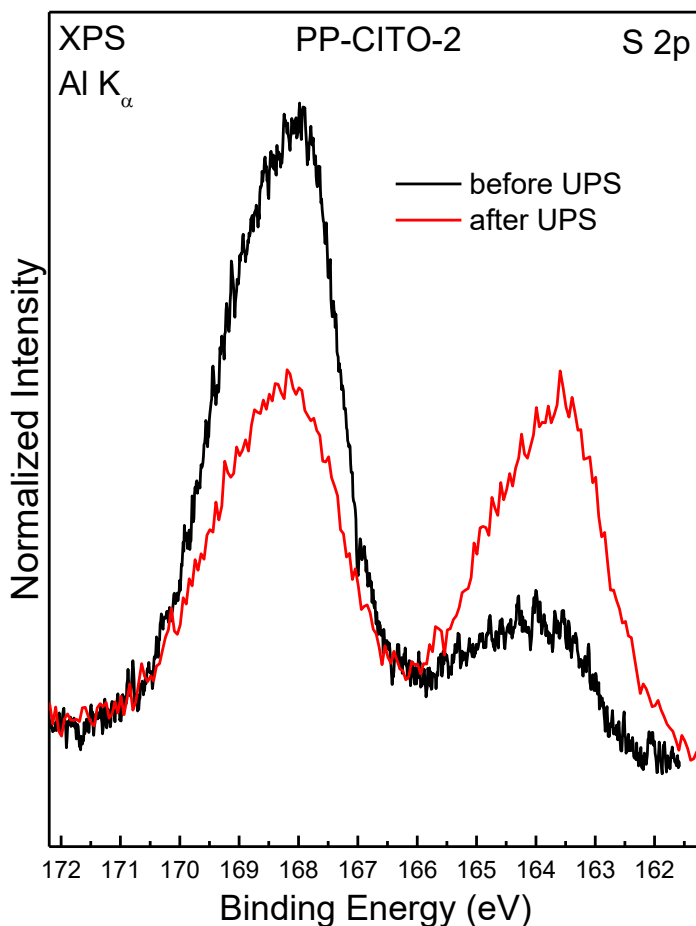


Figure 4-11. UV beam damage of PP film changes the intensity of PSS and PEDOT peaks in “before and after” XPS measurements

## Section 4.7 – Results: PEDOT:PSS on ITO

PEDOT:PSS samples made on both SITO and CITO showed the presence of indium in XPS measurements, even when two layers of PEDOT:PSS were applied and annealed between each layer. Figure 4-12, however, shows that this was not always the case, with no detectable In 3d peaks in the survey spectrum of the PP2-CITO sample.

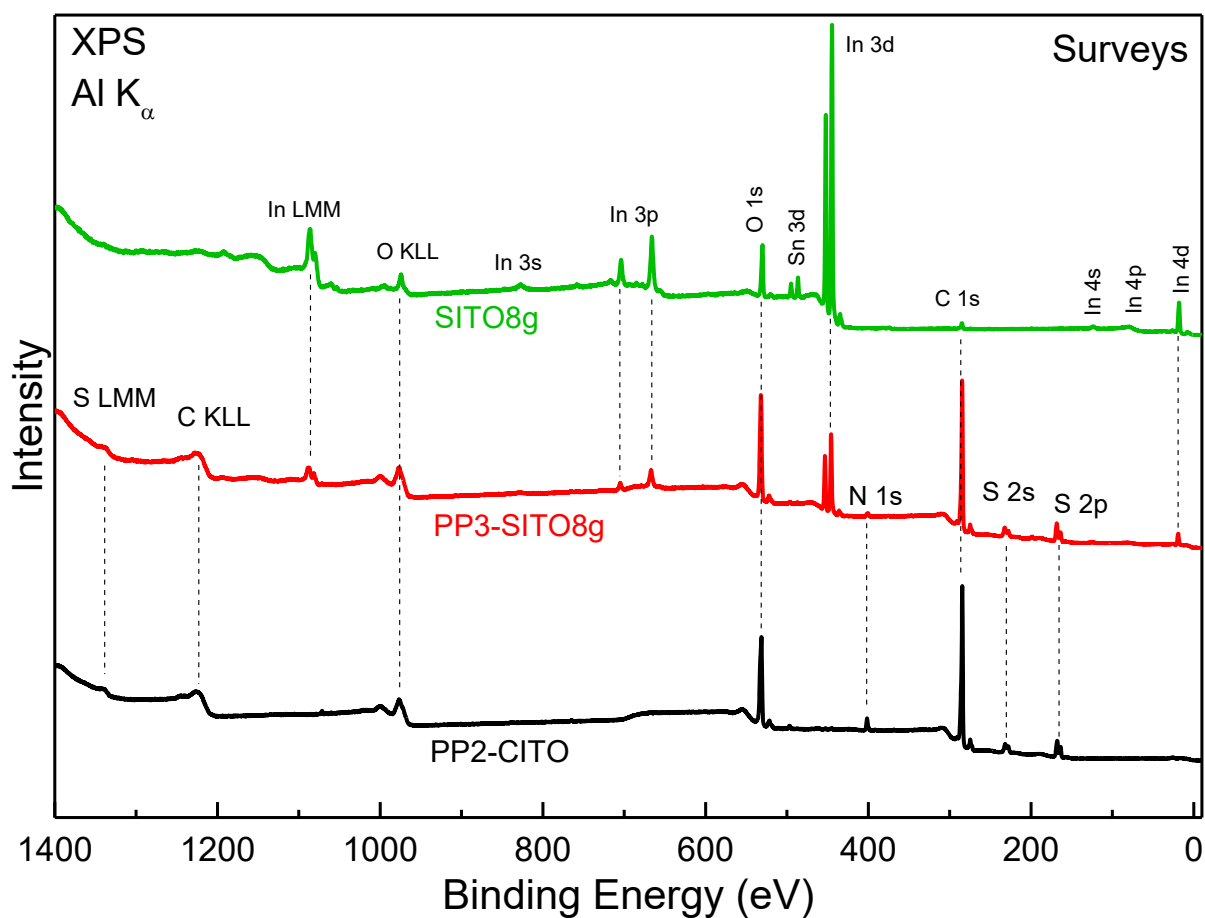


Figure 4-12. Survey spectra of PEDOT:PSS samples on SITO and CITO samples, with a SITO survey for reference purposes.



Taking additional scans of the In 3d region, it appears that the In 3d peaks are present but barely above the level of background noise (Figure 4-13). When different spots on the surface of the same sample are measured, the presence of the In 3d peaks becomes clear. Detecting indium at the sample surface could be due to several causes: diffusion of indium from the ITO into the PEDOT:PSS layer, as reported in the literature,<sup>[51,69]</sup> beam damage of overlying PSS, or inhomogeneities in the PEDOT:PSS film that leave areas of the substrate exposed and detectable by XPS. It could also be caused by a combination of these factors. The overall In 3d signal is much lower for the PP2-CITO sample than the PP3-SITO8g sample (Figures 4-12 and 4-13). A note on sample naming: the number after “PP” represents the number of layers of PEDOT:PSS placed on the substrate; likewise, the number after “SITO” defines the number of solution layers

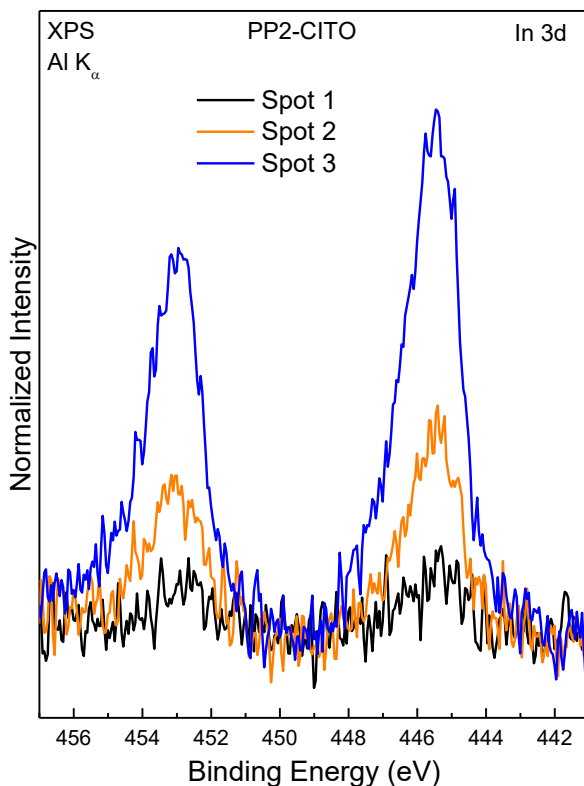


Figure 4-13. XPS measurement of In 3d peaks, detected at the surface of PEDOT:PSS on CITO.

that were applied, plus a “g” for the alkali-free glass substrate. Thus, PP3-SITO8g refers to three layers on PEDOT:PSS on eight layers of solution-processed ITO on a glass substrate, and PP2-CITO is two layers of PEDOT:PSS on commercial ITO.

Comparing the C and O 1s spectra between PEDOT:PSS samples on the two ITO substrates, additional differences are noted. The extent to which these differences can be attributed to the different substrates or to inhomogeneities in the PEDOT:PSS films cannot be determined. The major contributions to the C and O 1s spectra stem from the PEDOT and PSS polymers. Each polymer has a different chemical structure that contributes to the elemental signal, and differing ratios of PEDOT to PSS would change the profiles of the C 1s and O 1s spectra. An observation of the O 1s spectrum for PEDOT:PSS on the SITO sample in Figure 4-14: despite very detectable indium oxide peaks in the survey spectra, there is no expected metal

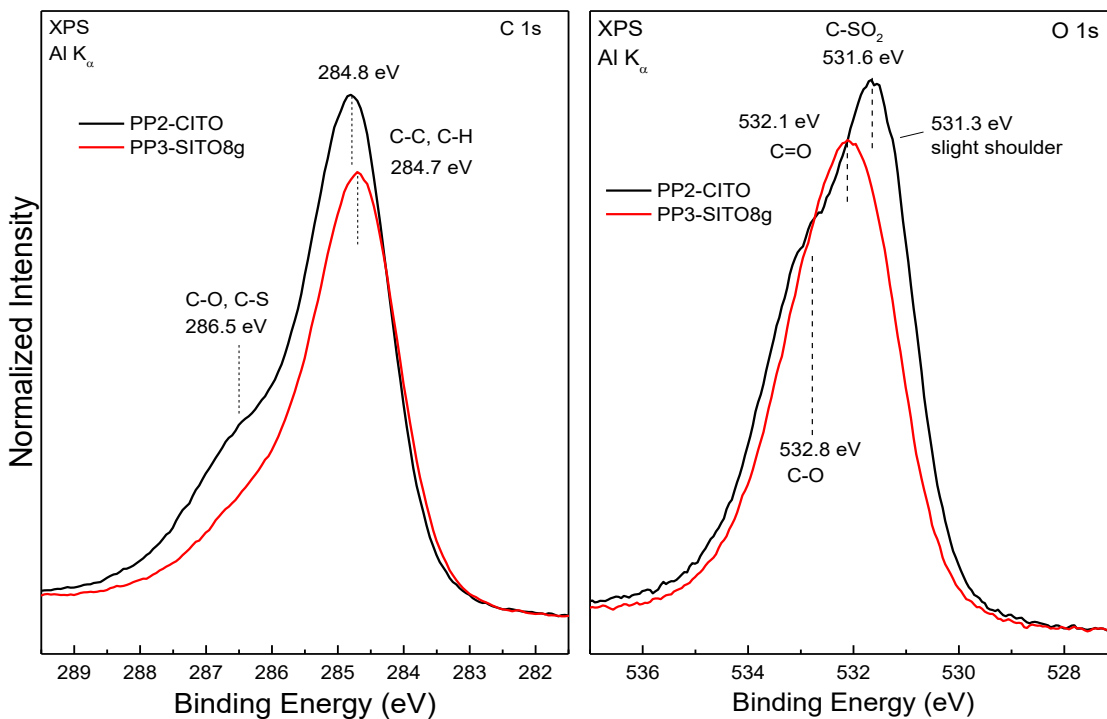


Figure 4-14. C 1s and O 1s spectra of the PP2-CITO and PP3-SITO8g samples shown in the survey spectra of Figure 4-12.

oxide contribution near 530 eV, but a metal oxide contribution close to 531 eV is possible.

To better understand if the indium just moves into the PEDOT:PSS layers, or if it forms a new species different from the indium oxide and hydroxide in the ITO, the peak positions of the In  $3d_{5/2}$  core level peak and the In  $M_4N_{4,5}N_{4,5}$  Auger peak were measured and the modified Auger parameter was calculated for these samples. The numerical results are presented in Table 4-2.

Sample	In $3d_{5/2}$ (eV)	In $M_4N_{4,5}N_{4,5}$ (eV)	$\alpha'$ (eV)
PP1-SITO	446.00 +/- 0.05	405.1 +/- 0.2*	851.1
PP2-SITO	445.51 +/- 0.05	404.90 +/- 0.05	850.41
PP1-CITO	445.00 +/- 0.05	406.3 +/- 0.5*	851.3
PP2-CITO	444.97 +/- 0.05	406.44 +/- 0.05	851.41

Table 4-2. In  $3d_{5/2}$  and In  $M_4N_{4,5}N_{4,5}$  peak positions, and modified Auger parameter for indium, as detected in PP thin films.

These results are also shown in a Wagner plot in Figure 4-15. The data points (crosses) have been extended to show the determination error. The approximate region of indium-sulfur species is included in the plot, to demonstrate that none of the data in Table 4-2 indicate the formation of indium-sulfur species. The difference between SITO and CITO as substrates is now readily observed. Indium in the PP-CITO samples lies in the region of indium oxides, and indium in the PP-SITO samples best corresponds to indium hydroxides.

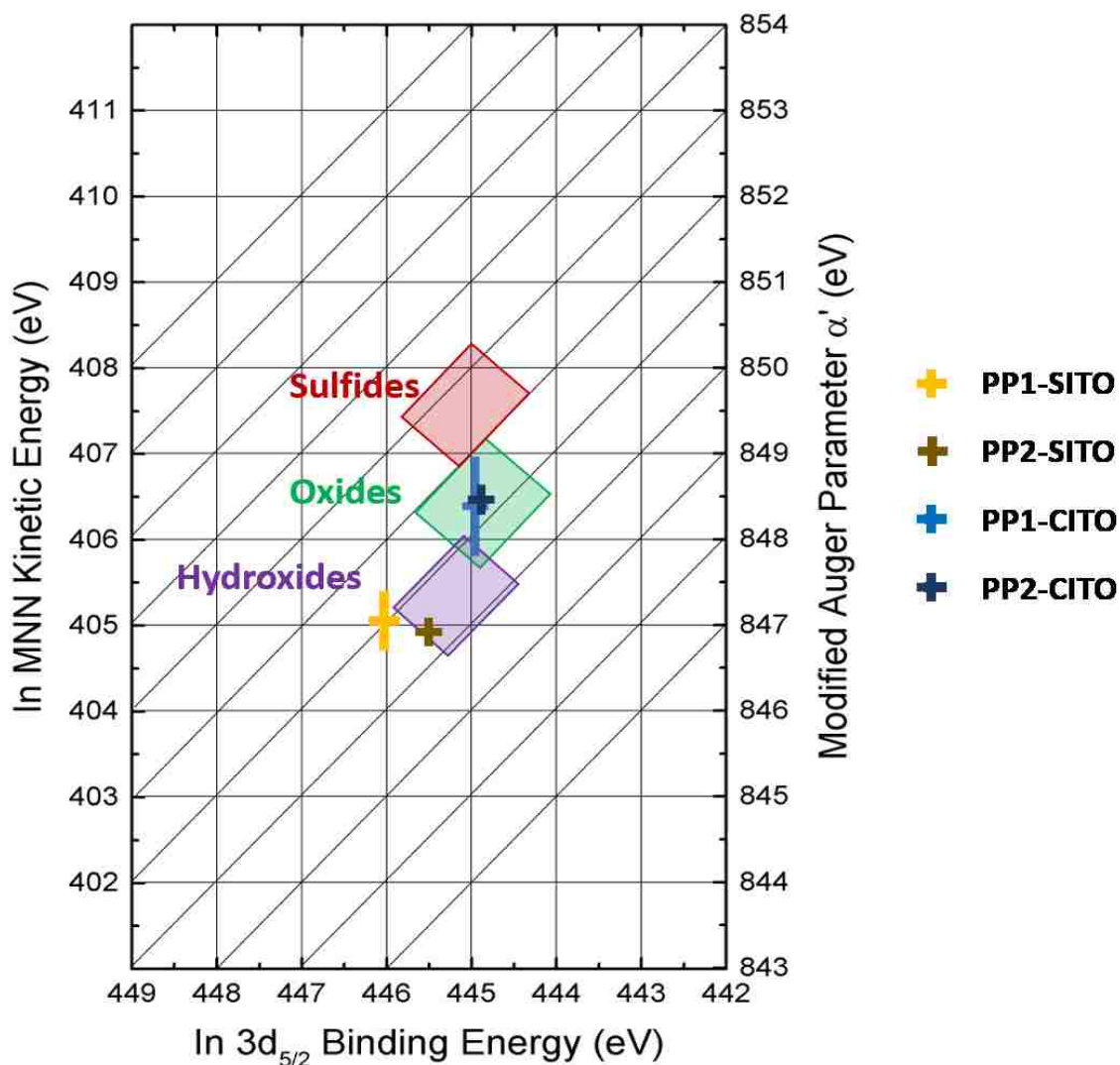


Figure 4-15. Wagner plot for indium from Fig. 2-4, with data added for PP-SITO and PP-CITO samples.

The PP-SITO samples were made by depositing PEDOT:PSS on SITO made immediately prior, i.e., without additional surface treatments. The hydroxide character of the detected indium likely reflects the post-processing hydroxides that remain on the surface; this also indicates that the O 1s hydroxides are attached to the indium and are not due to the presence of another species. The CITO substrates were cleaned using the acetone/IPES/heating treatment

as done with glass for the metal oxides. This may have removed adsorbed hydroxide and organic species, which otherwise contribute to the O 1s signal of an uncleaned sample.

Given the challenges of making continuous thin films with good substrate coverage, the possibility of (microscopic) holes in the PEDOT:PSS films cannot be eliminated. It is possible that the detected indium is not due to indium diffusion, but is instead an XPS signal from uncovered (or thinly covered) portions of the substrate. Since indium oxide and hydroxide have been detected on the different ITO substrates, an explanation for the presence of indium cannot be simply based on the diffusion of indium ions into PEDOT:PSS.

## Section 4.7 – Conclusions

The main finding of the experiments with PEDOT:PSS thin films is that process is much more important than substrate in determining important properties of PEDOT:PSS thin films. Modifying the aqueous dispersion and how it is handled may seem straightforward, but it is not a trivial undertaking.

The application process is very important, and spin coating pushes more PSS to the substrate edges, resulting in differing ratios of PEDOT to PSS as observed with XPS. The different work functions in different areas of the sample surface confirm this. Ultimately, spin coating produces a PEDOT:PSS thin film where PEDOT:PSS ratio and work function are dependent on the region of the substrate being measured. The susceptibility of PSS to beam damage is not unexpected, but it is something that must be considered in the context of the effects of varying PEDOT:PSS ratios and electronic properties.

Indium diffusion into the PEDOT:PSS has been reported in the literature,<sup>[51,88]</sup> and without looking further at the XPS data, this could be assumed to be occurring with these samples. Deeper examination of the core levels, Auger peaks, and the modified Auger parameter  $\alpha'$  tells a different story. If indium ion diffusion were occurring, there should be no difference in  $\alpha'$  between samples on SITO or SITO, nor such substantial differences on a Wagner plot. The PEDOT:PSS may not be completely covering the substrate at the microscopic level, but the detection of indium persists with the application of a second layer of PEDOT:PSS. Examination of the film morphology may help unravel this mystery.

The PEDOT:PSS thin films produced were not suitable for incorporation into a device platform for organic electronics research. However, changes to the process, perhaps the addition of a post-processing surface treatment of PEDOT:PSS, may produce films with a higher homogeneity in both PEDOT:PSS ratio and work function.

## Chapter 5 – SUMMARY AND FUTURE WORK

In this research, both organic and inorganic solution-processed materials were studied, specifically transparent conductive oxides (TCOs) made from an organic precursor solution, as well as the polymer mixture PEDOT:PSS. The importance of the various parameters of the solution process cannot be underestimated. There are many different ways to modify a solution process, and as shown here and in the wider body of literature, tailoring the solution process to the specific material is necessary to achieve the desired material properties. The fabrication process and any post-processing treatments can become very complex, and designing a specific solution process for a specific material, for a specific application, can easily turn into a dissertation project all by itself.

TCO thin films of indium-based metal oxides were produced using metal-acac precursor solutions with good results when using a temperature of 450 °C to pyrolyze the organic material in the precursor solution. Even at that temperature, some organic residues will remain at the surface, which can be removed with ion treatment and reduced with UHV heating. These residues were present whether the TCO thin film was made in air or in a nitrogen-filled glove box. The properties of the thin film made with this solution process are largely dependent on the metal oxide that is formed.

As demonstrated with ITO, the surface chemistry and electrical properties were very similar, due to the dominance of indium oxide as the major constituent for both solution-processed and commercially-made samples. Surface treatments commonly used to modify the ITO surface and change its work function could be used on solution-processed ITO or other metal oxides. One unexpected result was found for the ITO work function before and after ion treatment, where ion treatment slightly lowered the work function of the solution-processed ITO

sample, while either of the work functions (before and after ion treatment) was higher than that of the commercial sample. Thus, the results of surface treatments used to change a commercially-produced ITO surface may not yield the expected results. Some adjustments may be required in the handling of solution-processed metal oxides after fabrication, but this is not necessarily detrimental to their use. Depending on the application, solution-processed metal oxides may have more advantages than PVD-produced ones.

For incorporation into specific devices, resistivity measurements should be done on solution-processed TCO thin films of interest. If available, a probe head with metallized rubber contacts would be advantageous for good Ohmic contact with the TCO surface. In conjunction with resistivity measurements, characterization using scanning electron microscopy (SEM) with energy dispersive x-ray spectroscopy (EDX) would be useful to visualize the elemental distribution of the surface. SEM could also be used to examine surface smoothness and thin film thickness, if those parameters are significant for the device architecture.

It would also be interesting to characterize these TCOs with x-ray diffraction (XRD) for crystallinity. Crystallization of amorphous indium oxide thin films has been found to be near 520 °C, and the glass transition temperature at about 460 °C.<sup>[19]</sup> Given the very thin layer of low-concentration precursor solution being annealed at 450 °C, with a new film of solution being added and annealed repeatedly, it would be good to know if any crystallinity were present or if these films remain truly amorphous. A study involving resistivity and crystallinity, and how those characteristics relate to annealing temperature and time would add to the overall picture of the nature of these solution-processed TCOs.

For multinary TCOs, the chemical stoichiometry can be readily changed to create novel compounds. The solution process used here is well-suited to a research environment to quickly



and easily make novel metal oxides. Because the properties examined here depend more on the metal oxide than the solution-process, such samples are useful for initial phases of study.

Promising candidates could then be reproduced using other, more traditional methods, if solution-process effects such as hydroxides are a concern.

It may be possible to combine this solution process with some of the techniques currently being used in 3-D printing and additive manufacturing. Metal objects have been printed by using heat from lasers to sinter metal powder particles together to make 3-D metal objects. Lower-powered lasers could provide a heat source to precisely anneal the metal-acac precursor solution used in this project at specific locations on a substrate. This could enable even less waste of precursor material and be used to make both conductive and non-conductive metal oxides in printed patterns at a very small scale and in multiple layers, without having to make an enormous investment in nanotechnology fabrication methods. Advances in additive manufacturing techniques, particularly different types of 3-D printing, will increasingly drive materials development, including solution processing methods.

PEDOT:PSS is already the subject of ongoing research for use as a replacement for ITO<sup>[83]</sup> and as a component of biosensors.<sup>[84]</sup> It should be emphasized is that it is not trivial to get PEDOT:PSS in the form one wants it in with the properties one desires. The ratio of PEDOT to PSS is very important for its electrical properties, and due to the nature of the aqueous dispersion so commonly used, differences in these ratios within a thin film readily occur. There is much in the literature that seeks to address this, and the challenge becomes one of selecting the best methods to achieve the desired results, with care taken when combining different methods.

Enhancing conductivity and improving homogeneity can be done by removing PSS, and there are numerous methods employed to do so. In this research, UV exposure during UPS

measurements did this very well. It may be possible to adapt this into a method for PSS removal as a processing step or post-processing treatment. There is a report of successfully using UV-ozone to remove PSS.<sup>[89]</sup> A study decoupling the UV from the ozone as a treatment may prove illuminating; likewise, combining a UV treatment with other methods to remove or minimize PSS in PEDOT:PSS thin films could be useful.

In the race to discover and develop new materials for new technologies, it is sometimes forgotten that a single material is quite unlikely to be the magic bullet that solves several different or application problems, and perhaps not even solve a single, specific problem. A material can certainly be optimized for its intended purpose, but the materials it comes into contact with, how those materials are placed together, and the processes used to build a structure or device all contribute functionality and efficiency of the final product.

This research has shown that the process effects on material composition and properties cannot be taken for granted. A single material such as PEDOT:PSS has complexities that require more than a superficial understanding to fully realize its uses. In terms of building new electronic devices, organic or inorganic, teams composed of experts on individual materials are needed. Ultimately, progress will only be achieved through collaborative work where researchers can bring their individual expertise to cooperatively advance the next generations of materials and devices.

## APPENDIX A – LIST OF ABBREVIATIONS AND SYMBOLS

$\alpha'$	Modified Auger Parameter
acac	Acetylacetonate
CB	Conduction band
CBM	Conduction band minimum
CITO	Commercial ITO
EDX	Energy Dispersive X-ray Spectroscopy
$E_B$	Binding energy
$E_F$	Fermi level
$E_g$	Band gap
$E_K$	Kinetic energy
EM	Electromagnetic radiation
$E_{vac}$	Vacuum level
FWHM	Full width at half maximum
$h\nu$	Photon energy
HOMO	Highest occupied molecular orbital
IMFP	Inelastic Mean Free Path
In-ox	Indium oxide (non-stoichiometric)
IPA	Isopropanol
IPES	Inverse Photoemission Spectroscopy
IT	Ion treatment
ITO	Indium tin oxide
IZO	Indium zinc oxide

LUMO	Lowest unoccupied molecular orbital
MFP	Mean Free Path
OLED	Organic light-emitting diode
OPV	Organic photovoltaic
PES	Photoelectron Spectroscopy
PP	PEDOT:PSS
PV	Photovoltaic
PVD	Physical Vapor Deposition
SEC	Secondary Electron Cutoff
SEM	Scanning Electron Microscopy
SITO	Solution-processed ITO
Sn-ox	Tin oxide (non-stoichiometric)
TCO	Transparent conductive oxide
UHV	Ultra-high vacuum
UPS	Ultraviolet Photoelectron Spectroscopy
UV	Ultraviolet
UV-Vis	Ultraviolet-Visible
VB	Valence band
VBM	Valence band maximum
$\Phi$	Work Function
WF	Work Function
XPS	X-ray Photoelectron Spectroscopy
Zn-ox	Zinc Oxide (non-stoichiometric)

## APPENDIX B – SPECTROSCOPY EQUIPMENT

XPS, UPS, and IPES were performed on two separate UHV systems connected to a sample distribution chamber and N<sub>2</sub>-filled glove boxes for sample preparation:

- $\mu$ -metal UHV chamber with PHOIBOS150MCD electron analyzer, SPECSLab 2.78 software, SPECS XR-50 Mg/Al dual anode x-ray source, pressure-controlled helium UV source, and custom-built Ar-I<sub>2</sub> IPES detector with Staib electron gun
- Customized, computer-integrated VG Scienta (Scienta Omicron) UHV system with R4000 electron analyzer, SES 3.x software, monochromated Al x-ray source, SPECS XR-50 Mg/Al dual anode x-ray source, VUV5000 UV source with monochromator and extendable capillary, and custom PMT-based IPES detector with Staib electron gun

## APPENDIX C – CHEMICAL INFORMATION

Chemical, Sigma-Aldrich Product Number, CAS Number:

Indium(III) acetylacetonate, 13300 Aldrich, CAS Number 14405-45-9

Tin(IV) bis(acetylacetonate) dichloride, 404659 Aldrich, CAS Number 16919-46-3

Zn(acac)<sub>2</sub>, Bis(2,4-pentanedionato)zinc, 480991 Aldrich, CAS Number 108503-47-5

Vanadyl acetylacetonate, 574562 Aldrich, CAS Number 3153-26-2

PEDOT:PSS, 768642 Aldrich, CAS Number 155090-83-8

ITO coated glass slides (70-100 Ω/sq.), 576352 Aldrich, CAS Number 50926-11-9

## APPENDIX D – INPUT CODE FOR PEAK FITTING

The following is an example of the coding used with the fityk 0.9.4 software program. It was written into a text file, saved, and the file extension changed to “.fit” to be opened in the fityk program. The code loads the specified data files into the program and establishes the parameters and constraints for fitting a curve to the spectroscopic data. Data can be manually loaded into the program and constraints established afterward; however, using a code such as this has the advantages of consistent handling of batch data, ease of checking for errors in establishing fit parameters, and the ability to quickly repeat a fit procedure with the same parameters. The examples that follow were taken from a file used to fit XPS data of the sulfur 2p region collected from samples of PEDOT:PSS on solution-processed ITO.

The first lines specify the file path and which columns of data should be designated as x and y. In the examples below, column 3 data will be used for the x axis and column 4 for the y axis. The “@+” is used to load additional files.

```
@0<'C:[file path]\PPSITO-1m1.dat:3:4:.'  
@+<'C:[file path]...\PPSITO-2m1.dat:3:4:.'
```

Next, the parameters for the individual functions are set. The “~” means that value is allowed to vary during fitting. Initial parameters for a linear function are given:

```
$1_intercept = ~-15000  
$1_slope = ~120
```

Voigt functions are used for peak fitting. A Voigt function is a convolution of a Gaussian peak and a Lorentzian peak. The Gaussian line width represents experimental

broadening and Lorentzian line width the lifetime broadening in the spectra peak fit. Neither should vary among the multiple functions needed for the fit, so they are set equal to each other:

$$\text{\$2\_ghwhm} = \sim 0.75$$

$$\text{\$3\_ghwhm} = \text{\$2\_ghwhm}$$

$$\text{\$4\_ghwhm} = \text{\$2\_ghwhm}$$

... et cetera

$$\text{\$2\_lwidth} = \sim 0.1$$

$$\text{\$3\_lwidth} = \text{\$2\_lwidth}$$

$$\text{\$4\_lwidth} = \text{\$2\_lwidth}$$

... et cetera

For sulfur 2p peak fitting, the  $2p_{3/2}$  and  $2p_{1/2}$  energy position and peak splitting must be constrained. In the example given, the position of the  $2p_{3/2}$  is allowed to vary during fitting, but the  $2p_{1/2}$  peak must always be 1.19 eV higher in energy position:

$$\text{\$2\_E} = \sim 163.7$$

$$\text{\$3\_E} = 1.19 + \text{\$2\_E}$$

The area ratios are constrained in a similar way. The  $2p_{3/2}$  peak may vary in area, but  $2p_{1/2}$  peak must equal half of the area of the  $2p_{3/2}$  peak.

$$\text{\$2\_area} = \sim 2500$$

$$\text{\$3\_area} = (\text{\$2\_area})/2$$



The functions are defined in terms of the parameters:

```
%_1 = Linear($1_intercept, $1_slope)
%_2 = VoigtA($2_area, $2_E, $2_ghwhm, $2_lwidth/(2*$2_ghwhm))
%_3 = VoigtA($3_area, $3_E, $3_ghwhm, $3_lwidth/(2*$3_ghwhm))
... et cetera
```

The functions are applied to the spectra:

```
@0.F = %_1 + %_2 + %_3 + %_4 + %_5 + %_6 + %_7 + %_8 + %_9
@1.F = ... et cetera
```

The plotted area is defined:

```
plot [154:175][-1000:16000]
```

The active data points are defined for each spectrum:

```
A = 162.5<x and x<170.75 in @0
A = 162.5<x and x<170.75 in @1
```

## APPENDIX E – SPIN COATERS

### Section E.1 – Single-Speed Spin Coater

A single speed spin coater was made in-house by Dr. Marc Häming for making metal oxide thin films. This spin coater was made from a 3-wire computer fan attached to a large piece of metal to provide a stable base. A mini compact disc was attached to the top of the fan motor, and a copper wire holder sized for 25 x 25 mm<sup>2</sup> substrates was attached to this. A similar copper wire holder on a 25 x 25 mm<sup>2</sup> glass substrate was made for use with 15 x 15 mm<sup>2</sup> substrates. The spin speed of this coater, as tested with an oscilloscope, is approximately 3200 rpm.



Figure E-1. Single-speed spin coater. Copper wire substrate holders visible on top.

### Section E.2 – Variable-Speed Spin Coater

A variable-speed spin coater was designed and built for higher spinning speeds that would be needed for creating thin films from more viscous (organic) solutions. Based on the

Häming spin coater described above, this variable spin coater was specifically designed with a smaller footprint than the Häming spin coater, in order to conserve the extremely limited working space in the glovebox where it would be used. The dimensions of commercial spin coaters would not fit in the space available.

Electronic parts:

- Computer case fan, 60 x 25 mm<sup>2</sup>, model FAN6X25TX3H, from StarTech.com. 3-pin, TX3 connection, rated 5000 rpm. 12 V DC input.
- Plug-in power supply with DC output: 12 V, 300 mA
- 2-position (on/off) rocker switch
- 8-position rotary switch with solder lugs
- Resistors ( $\pm 5\%$  tolerance) and circuit board

Base parts:

- Scrap anti-static PVC
- Scrap aluminum profile sections
- Self-adhesive clear rubber pads

Build:

Most of the fan blades were removed with a Dremel tool to minimize air flow. This increased the maximum speed to over 7000 rpm. Two sections of copper mesh were trimmed and formed to hold 25x25 mm<sup>2</sup> and 15x15 mm<sup>2</sup> substrates, respectively. The mesh for the larger substrates was secured to the center of the fan motor with epoxy. The smaller mesh was attached to a 25x25 mm<sup>2</sup> glass substrate; the surface of the glass was scratched and sanded to enable

bonding with the mesh and epoxy.

The circuitry was prototyped on a breadboard using various resistors and measuring the resulting frequencies with a Keysight oscilloscope. By increasing resistance in the power circuit of the fan, the spin speed is reduced. For the 8-position switch, the target values were 3500 to 7000 rpm in increments of 500. An 8-position switch was chosen instead of using a variable resistor to ensure that the spin speeds would be reproducible. When the circuitry was soldered together, the overall resistance changed, and as a result, the final measured speeds are higher than the target speeds (Table F-1). Speeds were measured from start-up for 30 seconds, hence the second column average contains lower rpm values.

Switch Number	Resistance (Ohm)	Average rpm from start-up	Std. Dev.	Average rpm 10 s after start-up	Std. Dev.
1	18	7100	130	7200	80
2	30	6500	140	6600	80
3	40	6050	150	6200	150
4	52	5600	120	5750	170
5	67	5150	80	5400	90
6	85	4600	130	4800	100
7	112	4100	60	4300	80
8	137	3600	80	3800	40

Table E-1. Measurements of rpm for each position of 8-position selector switch after final assembly of spin coater.

Two scrap aluminum profile sections were used to provide weight to the base, and scrap sections of clear, anti-static PVC were used to form a removable enclosure to protect against spills. The fan was mounted to the PVC cover, and the cover was mounted to the aluminum profile sections. Nuts and bolts were used for these mountings to allow for easy disassembly if the fan must be replaced. Self-adhesive clear rubber feet were applied to the bottom of the PVC

cover, and small pieces of same material were applied to the bottom of the profile sections; the purpose of this was to minimize movement and vibrations between the spin coater sections and the spin coater as a whole.

The resistor circuit board was placed at the back of the spin coater. The board is connected by three-pin connectors between the fan and the power supply. This enables the board to be removed and replaced with a different board or other circuitry to change the resistance –

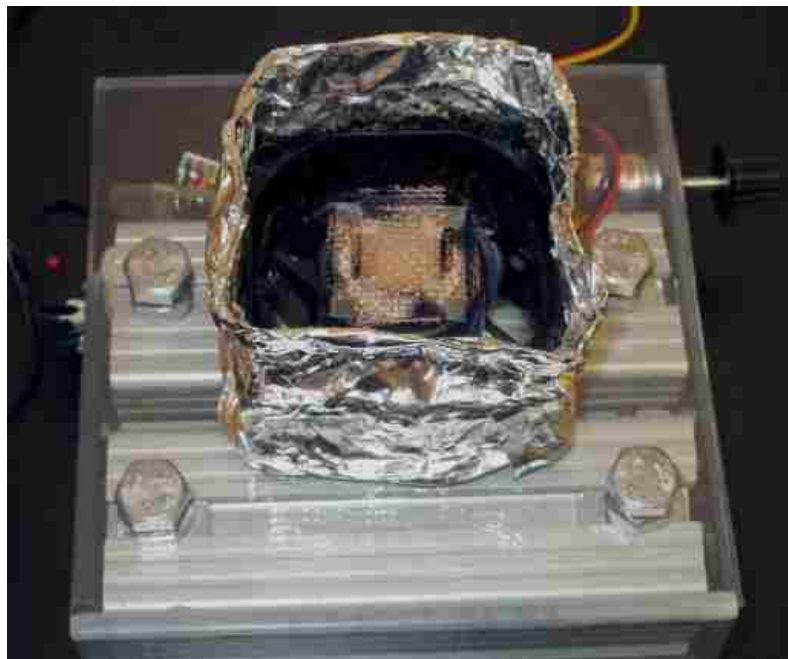


Figure E-2. Variable speed spin coater. Copper mesh holders for  $15 \times 15 \text{mm}^2$  and  $25 \times 25 \text{mm}^2$  substrates visible on top. Profile sections and electronics are visible through the PVC enclosure. On/off switch is on the left, and rotary 8-position rpm selector switch is on the right.

and thereby the speed – settings. The 8-position switch, however, is soldered to the board and must be removed with the board. Electrical tape provides a barrier between the board and the profile, and the back of the spin coater remains open to dissipate any heat from the resistors. The on/off switch was secured to one of the profiles with epoxy on the side opposite the 8-position switch.

The substrate holders were tested for stability at all spin speeds. Even up to 7200 RPM, substrates were held securely in the holders. A connection to the 3<sup>rd</sup> wire of the fan remains available to measure rpm at any time. A “collar” of aluminum foil wrapped around the fan contains spatter very well and is easily replaced as needed.

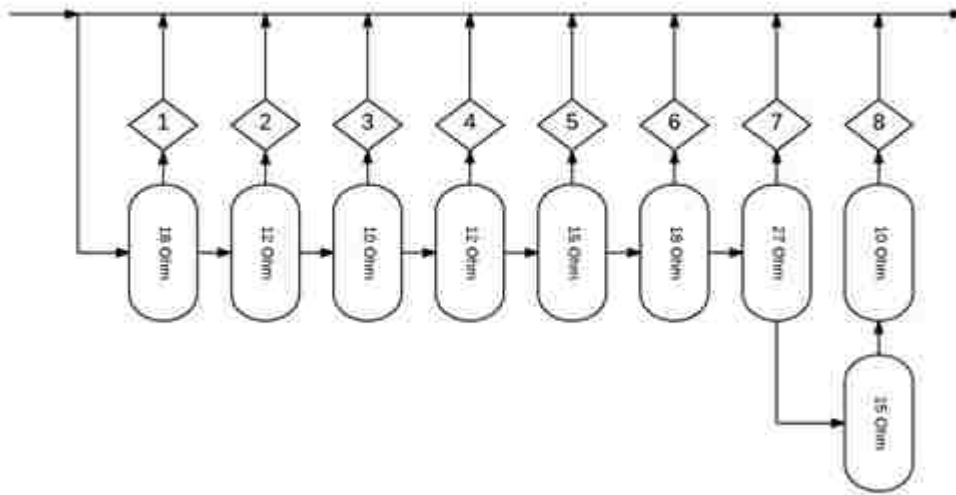


Figure E-3. Photograph of circuit board at the back of the spin coater and diagram of the resistors connected to the switch positions.

## BIBLIOGRAPHY

- [1] International Energy Agency, *Renewables 2017: Analysis and Forecasts to 2022, Executive Summary*, International Energy Agency, **2017**.
- [2] R. Cavanagh, A. Levin, *NRDC's Fifth Annual Energy Report: America's Clean Energy Revolution*, Natural Resources Defense Council, **2017**.
- [3] R. Meyer, "How Solar and Wind Got So Cheap, So Fast," can be found under <http://www.newsweek.com/how-solar-and-wind-got-so-cheap-so-fast-401450>, **2015**.
- [4] A. Leach, *The Guardian* **2015**.
- [5] I. Johnston, "The developing world is investing more in renewable energy than rich countries," can be found under <http://www.independent.co.uk/environment/climate-change/renewable-energy-investment-developed-world-developing-world-ren21-report-a7058436.html>, **2016**.
- [6] B. Gardiner, "Three Reasons to Believe in China's Renewable Energy Boom," can be found under <https://news.nationalgeographic.com/2017/05/china-renewables-energy-climate-change-pollution-environment/>, **2017**.
- [7] T. C. Nguyen, *Washington Post* **2015**.
- [8] D. Talbot, "LEDs vs. the Lightbulb," can be found under <https://www.technologyreview.com/s/401913/leds-vs-the-lightbulb/>, **2003**.
- [9] W. Zhao, S. Li, H. Yao, S. Zhang, Y. Zhang, B. Yang, J. Hou, *J. Am. Chem. Soc.* **2017**, *139*, 7148–7151.
- [10] Y. Chuo, B. Omrane, C. Landrock, J. Aristizabal, D. Hohertz, S. V. Grayli, B. Kaminska, *IEEE Design Test of Computers* **2011**, *28*, 32–40.

- [11] infinityPV, “infinityPV - OPV,” can be found under <https://infinitypv.com/products/opv>,  
**n.d.**
- [12] J. Perelaer, P. J. Smith, D. Mager, D. Soltman, S. K. Volkman, V. Subramanian, J. G. Korvink, U. S. Schubert, *J. Mater. Chem.* **2010**, *20*, 8446–8453.
- [13] V. Subramanian, J. B. Chang, A. de la F. Vornbrock, D. C. Huang, L. Jagannathan, F. Liao, B. Mattis, S. Molesa, D. R. Redinger, D. Soltman, et al., in *Solid-State Device Research Conference, 2008. ESSDERC 2008. 38th European*, **2008**, pp. 17–24.
- [14] S. Mason, “UCLA researchers use liquid inks to create better solar cells,” can be found under <http://newsroom.ucla.edu/releases/ucla-researchers-use-liquid-inks-to-create-better-solar-cells>, **2014**.
- [15] L. Vayssieres, *Adv. Mater.* **2003**, *15*, 464–466.
- [16] A. Stadler, *Materials* **2012**, *5*, 661–683.
- [17] “USGS Minerals Information: Indium,” can be found under <https://minerals.usgs.gov/minerals/pubs/commodity/indium/>, **n.d.**
- [18] T. Maruyama, A. Kojima, *Jpn. J. Appl. Phys.* **1988**, *27*, L1829–L1831.
- [19] D. Gallagher, F. Scanlan, R. Houriet, H. J. Mathieu, T. A. Ring, *Journal of Materials Research* **1993**, *8*, 3135–3144.
- [20] F. C. Krebs, *Solar Energy Materials and Solar Cells* **2009**, *93*, 394–412.
- [21] Instituto di Fotonica e Nanotecnologie, “RF-Sputtering principles - IFN Trento,” can be found under <http://www.tn.ifn.cnr.it/facilities/rf-sputtering-facility/rf-sputtering-principles>,  
**n.d.**
- [22] M. Häming, A. Issanin, D. Walker, H. von Seggern, W. Jägermann, K. Bonrad, *J. Phys. Chem. C* **2014**, *118*, 12826–12836.



- [23] M. Bär, S. Pookpanratana, L. Weinhardt, R. G. Wilks, B. A. Schubert, B. Marsen, T. Unold, M. Blum, S. Krause, Y. Zhang, et al., *Journal of Electron Spectroscopy and Related Phenomena* **2013**, *190, Part A*, 47–53.
- [24] Heske, Clemens, **2015**.
- [25] “Mean free path definition and meaning | Collins English Dictionary,” can be found under <https://www.collinsdictionary.com/us/dictionary/english/mean-free-path>, **n.d.**
- [26] M. P. Seah, W. A. Dench, *Surf. Interface Anal.* **1979**, *1*, 2–11.
- [27] “Mean free path,” can be found under [https://en.wikipedia.org/w/index.php?title=Mean\\_free\\_path&oldid=787219803](https://en.wikipedia.org/w/index.php?title=Mean_free_path&oldid=787219803), **2017**.
- [28] D. Briggs, M. P. Seah, *Practical Surface Analysis*, John Wiley & Sons, **1983**.
- [29] “Ultraviolet photoelectron spectroscopy,” can be found under [https://en.wikipedia.org/w/index.php?title=Ultraviolet\\_photoelectron\\_spectroscopy&oldid=788858775](https://en.wikipedia.org/w/index.php?title=Ultraviolet_photoelectron_spectroscopy&oldid=788858775), **2017**.
- [30] “NIST X-ray Photoelectron Spectroscopy (XPS) Database, Version 4.1,” can be found under <https://srdata.nist.gov/xps/>, **2012**.
- [31] A. Kamal, in *Particle Physics*, Springer, Berlin, Heidelberg, **2014**, pp. 1–78.
- [32] T. Gleim, C. Heske, E. Umbach, C. Schumacher, S. Gundel, W. Faschinger, A. Fleszar, C. Ammon, M. Probst, H.-P. Steinrück, *Surface Science* **2003**, *531*, 77–85.
- [33] H. Kim, C. M. Gilmore, A. Piqué, J. S. Horwitz, H. Mattoussi, H. Murata, Z. H. Kafafi, D. B. Chrisey, *Journal of Applied Physics* **1999**, *86*, 6451–6461.
- [34] D. W. Barnum, *Journal of Inorganic and Nuclear Chemistry* **1961**, *21*, 221–237.
- [35] W. Caminati, J.-U. Grabow, *J. Am. Chem. Soc.* **2006**, *128*, 854–857.
- [36] *Sigma-Aldrich Product Catalog* **2017**.

- [37] E. Shuter, S. J. Rettig, C. Orvig, *Acta Cryst C, Acta Cryst Sect C, Acta Crystallogr C, Acta Crystallogr Sect C, Acta Crystallogr C Cryst Struct Commun, Acta Crystallogr Sect C Cryst Struct Commun* **1995**, *51*, 12–14.
- [38] M. Wojdyr, *J Appl Cryst, J Appl Crystallogr* **2010**, *43*, 1126–1128.
- [39] M. Wojdyr, *Fityk*, **2010**.
- [40] E. Y. Wang, L. Hsu, *J. Electrochem. Soc.* **1978**, *125*, 1328–1331.
- [41] C. A. Pan, T. P. Ma, *Applied Physics Letters* **1980**, *37*, 714–716.
- [42] L. Chkoda, C. Heske, M. Sokolowski, E. Umbach, F. Steuber, J. Staudigel, M. Stößel, J. Simmerer, *Synthetic Metals* **2000**, *111–112*, 315–319.
- [43] R. F. Minibaev, A. A. Bagatur'yants, D. I. Bazhanov, A. A. Knizhnik, M. V. Alfimov, *Nanotechnol Russia* **2010**, *5*, 185–190.
- [44] K. H. Lee, H. W. Jang, K.-B. Kim, Y.-H. Tak, J.-L. Lee, *Journal of Applied Physics* **2004**, *95*, 586–590.
- [45] R. Schlaf, H. Murata, Z. H. Kafafi, *Journal of Electron Spectroscopy and Related Phenomena* **2001**, *120*, 149–154.
- [46] K. Sugiyama, H. Ishii, Y. Ouchi, K. Seki, *Journal of Applied Physics* **2000**, *87*, 295–298.
- [47] D. A. Duncan, R. Mendelsberg, M. Mezher, K. Horsley, S. G. Rosenberg, M. Blum, G. Xiong, L. Weinhardt, M. Gloeckler, C. Heske, *Adv. Mater. Interfaces* **2016**, *3*, n/a-n/a.
- [48] G. Greczynski, T. Kugler, W. R. Salaneck, *Thin Solid Films* **1999**, *354*, 129–135.
- [49] G. Zotti, S. Zecchin, G. Schiavon, F. Louwet, L. Groenendaal, X. Crispin, W. Osikowicz, W. Salaneck, M. Fahlman, *Macromolecules* **2003**, *36*, 3337–3344.
- [50] K. W. Wong, H. L. Yip, Y. Luo, K. Y. Wong, W. M. Lau, K. H. Low, H. F. Chow, Z. Q. Gao, W. L. Yeung, C. C. Chang, *Applied Physics Letters* **2002**, *80*, 2788–2790.

- [51] S. J. Jo, C. S. Kim, J. B. Kim, S. Y. Ryu, J. H. Noh, H. K. Baik, Y. S. Kim, S.-J. Lee, *Journal of Applied Physics* **2008**, *103*, 114502.
- [52] F. Zabihi, Y. Xie, S. Gao, M. Eslamian, *Applied Surface Science* **2015**, *338*, 163–177.
- [53] J. Huang, P. F. Miller, J. C. de Mello, A. J. de Mello, D. D. C. Bradley, *Synthetic Metals* **2003**, *139*, 569–572.
- [54] B. Friedel, P. E. Keivanidis, T. J. K. Brenner, A. Abrusci, C. R. McNeill, R. H. Friend, N. C. Greenham, *Macromolecules* **2009**, *42*, 6741–6747.
- [55] Y. Kim, A. M. Ballantyne, J. Nelson, D. D. C. Bradley, *Organic Electronics* **2009**, *10*, 205–209.
- [56] J. Y. Kim, J. H. Jung, D. E. Lee, J. Joo, *Synthetic Metals* **2002**, *126*, 311–316.
- [57] S. K. M. Jönsson, J. Birgersson, X. Crispin, G. Greczynski, W. Osikowicz, A. W. Denier van der Gon, W. R. Salaneck, M. Fahlman, *Synthetic Metals* **2003**, *139*, 1–10.
- [58] A. M. Nardes, R. A. J. Janssen, M. Kemerink, *Adv. Funct. Mater.* **2008**, *18*, 865–871.
- [59] H. Yan, H. Okuzaki, *Synthetic Metals* **2009**, *159*, 2225–2228.
- [60] J. Palathinkal Thomas, L. Zhao, D. McGillivray, K. Tong Leung, *Journal of Materials Chemistry A* **2014**, *2*, 2383–2389.
- [61] B. Fan, X. Mei, J. Ouyang, *Macromolecules* **2008**, *41*, 5971–5973.
- [62] A. M. Nardes, M. Kemerink, M. M. de Kok, E. Vinken, K. Maturova, R. A. J. Janssen, *Organic Electronics* **2008**, *9*, 727–734.
- [63] S.-I. Na, G. Wang, S.-S. Kim, T.-W. Kim, S.-H. Oh, B.-K. Yu, T. Lee, D.-Y. Kim, *Journal of Materials Chemistry* **2009**, *19*, 9045–9053.
- [64] K.-H. Hwang, H. J. Seo, S.-H. Nam, J.-H. Boo, *Journal of Nanoscience and Nanotechnology* **2015**, *15*, 7652–7656.

- [65] T. Wang, Y. Qi, J. Xu, X. Hu, P. Chen, *Applied Surface Science* **2005**, *250*, 188–194.
- [66] Q. Wei, M. Mukaida, Y. Naitoh, T. Ishida, *Adv. Mater.* **2013**, *25*, 2831–2836.
- [67] J. Huang, P. F. Miller, J. S. Wilson, A. J. de Mello, J. C. de Mello, D. D. C. Bradley, *Adv. Funct. Mater.* **2005**, *15*, 290–296.
- [68] M. Kemerink, S. Timpanaro, M. M. de Kok, E. A. Meulenkaamp, F. J. Touwslager, *J. Phys. Chem. B* **2004**, *108*, 18820–18825.
- [69] T. P. Nguyen, P. Le Rendu, P. D. Long, S. A. De Vos, *Surface and Coatings Technology* **2004**, *180–181*, 646–649.
- [70] S. Timpanaro, M. Kemerink, F. J. Touwslager, M. M. De Kok, S. Schrader, *Chemical Physics Letters* **2004**, *394*, 339–343.
- [71] C. S. S. Sangeeth, M. Jaiswal, R. Menon, *J. Phys.: Condens. Matter* **2009**, *21*, 072101.
- [72] L. Ouyang, C. Musumeci, M. J. Jafari, T. Ederth, O. Inganäs, *ACS Appl. Mater. Interfaces* **2015**, *7*, 19764–19773.
- [73] U. Lang, E. Müller, N. Naujoks, J. Dual, *Adv. Funct. Mater.* **2009**, *19*, 1215–1220.
- [74] T. Takano, H. Masunaga, A. Fujiwara, H. Okuzaki, T. Sasaki, *Macromolecules* **2012**, *45*, 3859–3865.
- [75] N. Kim, S. Kee, S. H. Lee, B. H. Lee, Y. H. Kahng, Y.-R. Jo, B.-J. Kim, K. Lee, *Adv. Mater.* **2014**, *26*, 2268–2272.
- [76] L. S. C. Pingree, B. A. MacLeod, D. S. Ginger, *J. Phys. Chem. C* **2008**, *112*, 7922–7927.
- [77] X. Crispin, F. L. E. Jakobsson, A. Crispin, P. C. M. Grim, P. Andersson, A. Volodin, C. van Haesendonck, M. Van der Auweraer, W. R. Salaneck, M. Berggren, *Chem. Mater.* **2006**, *18*, 4354–4360.

- [78] M. Döbbelin, R. Marcilla, M. Salsamendi, C. Pozo-Gonzalo, P. M. Carrasco, J. A. Pomposo, D. Mecerreyes, *Chem. Mater.* **2007**, *19*, 2147–2149.
- [79] A. M. Nardes, M. Kemerink, R. a. J. Janssen, J. a. M. Bastiaansen, N. M. M. Kiggen, B. M. W. Langeveld, A. J. J. M. van Breemen, M. M. de Kok, *Adv. Mater.* **2007**, *19*, 1196–1200.
- [80] Y. Xia, J. Ouyang, *Journal of Materials Chemistry* **2011**, *21*, 4927–4936.
- [81] E. Vitoratos, S. Sakkopoulos, N. Paliatsas, K. Emmanouil, S. A. Choulis, *Open Journal of Organic Polymer Materials* **2012**, *02*, 7.
- [82] B. Friedel, T. J. K. Brenner, C. R. McNeill, U. Steiner, N. C. Greenham, *Organic Electronics* **2011**, *12*, 1736–1745.
- [83] Y. H. Kim, C. Sachse, M. L. Machala, C. May, L. Müller-Meskamp, K. Leo, *Adv. Funct. Mater.* **2011**, *21*, 1076–1081.
- [84] E. Moczko, G. Istamboulie, C. Calas-Blanchard, R. Rouillon, T. Noguer, *J. Polym. Sci. A Polym. Chem.* **2012**, *50*, 2286–2292.
- [85] *Sigma-Aldrich Product Catalog* **n.d.**
- [86] M. C. Biesinger, **2015**.
- [87] G. Greczynski, T. Kugler, M. Keil, W. Osikowicz, M. Fahlman, W. R. Salaneck, *Journal of Electron Spectroscopy and Related Phenomena* **2001**, *121*, 1–17.
- [88] T. P. Nguyen, S. A. de Vos, *Applied Surface Science* **2004**, *221*, 330–339.
- [89] W. J. Dong, G. H. Jung, S. Y. Kim, J.-L. Lee, *Solar Energy Materials and Solar Cells* **2013**, *109*, 240–245.

## CURRICULUM VITAE

**Lynette M. Kogler**

Department of Chemistry & Biochemistry

University of Nevada, Las Vegas

[koglerl@unlv.nevada.edu](mailto:koglerl@unlv.nevada.edu)

[lmkogler@outlook.com](mailto:lmkogler@outlook.com)

### DEGREE

May 1995 Bachelor of Science, Physics & Astronomy, Texas Christian University.  
Cum laude. Honors Program – Dept. Honors in Physics.

### RESEARCH EXPERIENCE

2013-Present Graduate Assistant, Department of Chemistry & Biochemistry,  
University of Nevada, Las Vegas  
Research group of Dr. Clemens Heske, Surface & Interface Science.

Spring 2016 Graduate Research Certificate, University of Nevada, Las Vegas

Summer 1993 Undergraduate Lab Assistant, Texas Christian University, Fort Worth, TX  
Research group of Dr. T.W. Zerda, Physics Department.

## PRESENTATIONS

- April 2017     Poster, UNLV Graduate and Professional Student Research Forum: “Interface Characterization of PEDOT:PSS on ITO Using Photoelectron Spectroscopy”
- April 2017     Oral presentation, American Chemical Society 253<sup>rd</sup> National Meeting: “Interface Characterization of PEDOT:PSS on ITO Using Photoelectron Spectroscopy”
- April 2017     Poster, American Chemical Society 253<sup>rd</sup> National Meeting: “Interface Characterization of PEDOT:PSS on ITO Using Photoelectron Spectroscopy”
- March 2017     Poster, American Physical Society March Meeting: “Interface Characterization of PEDOT:PSS on ITO Using Photoelectron Spectroscopy”
- June 2016     Oral presentation, Electronic Materials Conference: “Characterizing Electronic and Chemical Properties of Solution-Processed Transparent Conductive Oxides Using Photoelectron and Inverse Photoemission Spectroscopy”
- March 2016     Oral presentation, UNLV Graduate and Professional Student Research Forum: “Characterizing Electronic and Chemical Properties of Solution-Processed Transparent Conductive Oxides Using Photoelectron and Inverse Photoemission Spectroscopy”

## NON-ACADEMIC PROFESSIONAL EXPERIENCE

2003-2010 Criminalist I/II, Scottsdale Police Department, Scottsdale, AZ  
Analyzed drug evidence, blood samples for alcohol, and firearm and toolmark evidence.

2000-2003 Criminalist I, Firearms Section, Phoenix Police Department, Phoenix, AZ  
Examined firearms and ammunition components.

1998-2000 Evidence Technician, Latent Print Section, Phoenix Police Dept., Phoenix, AZ  
Processed crime scenes with photography, latent print development, and other techniques.

## NON-ACADEMIC PRESENTATIONS

May 2010 Poster, Association of Firearm and Toolmark Examiners 2010 Training Seminar:  
“Infrared Photography: An Overview for the Firearm Examiner”

Sept. 2004 Presentation: “Poisonous Plants of the Southwest”, California Association of  
Toxicologists. Based on independent review of literature in botany and chemistry.



## PROFESSIONAL MEMBERSHIPS

American Chemical Society

American Physical Society

American Vacuum Society

Association for Women in Science

Materials Research Society

Phi Kappa Phi

## AWARDS

April 2017    Honorable Mention, poster, UNLV Graduate and Professional Student Research  
Forum

March 2016    2<sup>nd</sup> Place, oral presentation, UNLV Graduate and Professional Student Research  
Forum

## DISSERTATION TITLE

Surface and Interface Characterization of Solution-Processed Metal Oxides and PEDOT:PSS  
Using Photoelectron Spectroscopy

DISSERTATION EXAMINATION COMMITTEE

Dr. Clemens Heske, Advisory Committee Chair

Dr. Dong-Chan Lee, Advisory Committee Member

Dr. Kathleen Robins, Advisory Committee Member

Dr. Daniel Gerrity, Graduate College Representative